Summer 1998

The Solution of Hypersingular Integral Equations With Applications in Acoustics and Fracture Mechanics

Richard S. St. John
Old Dominion University

THE SOLUTION OF HYPERSINGULAR INTEGRAL EQUATIONS

WITH APPLICATIONS IN

ACOUSTICS AND FRACTURE MECHANICS

by

Richard S. St.John
B.S. May 1993, Old Dominion University
M.S. May 1995, Old Dominion University

A Dissertation submitted to the Faculty of
Old Dominion University in Partial Fulfillment of the
Requirement for the Degree of

DOCTOR OF PHILOSOPHY

COMPUTATIONAL AND APPLIED MATHEMATICS

OLD DOMINION UNIVERSITY
August 1998

Approved by:

John Tweed (Director)

Mark H. Dunn (Member)

Gordon Melrose (Member)

F. Farassat (Member)

John H. Heinbockel (Member)

ABSTRACT

THE SOLUTION OF HYPERSINGULAR INTEGRAL EQUATIONS WITH APPLICATIONS IN FRACTURE MECHANICS AND ACOUSTICS.

Richard S. St.John
Old Dominion University, 1998
Director: Dr. John Tweed

The numerical solution of two classes of hypersingular integral equations is addressed. Both classes are integral equations of the first kind, and are hypersingular due to a kernel containing a Hadamard singularity. The convergence of a Galerkin method and a collocation method is discussed and computationally efficient algorithms are developed for each class of hypersingular integral equation.

Interest in these classes of hypersingular integral equations is due to their occurrence in many physical applications. In particular, investigations into the scattering of acoustic waves by moving objects and the study of dynamic Griffith crack problems has necessitated a computationally efficient technique for solving such equations.

Fracture mechanic studies are performed using the aforementioned techniques. We focus our studies on problems addressing the Stress Intensity Factors (SIF) of a finite Griffith crack scattering an out of plane shear wave. In addition, we consider the problem of determining the SIF of two parallel Griffith cracks and two perpendicular Griffith cracks. It is shown that the method is very accurate and computationally efficient.

In acoustics, we first consider the moving wing problem. For this problem we wish to find the sound produced by the interaction of a moving wing with a known

incident sound source. Although this problem is relatively simple, it is a good precursor to the two-dimensional, finite, moving duct problem.

The bulk of the research is focused on solving the two-dimensional, finite, moving duct problem. Here we look at sound propagation and radiation from a finite, two-dimensional, moving duct with a variety of inlet configurations. In particular, we conduct studies on the redirection of sound by a so-called scarf inlet design. In said designs, we are able to demonstrate the ability to redirect sound away from sensitive areas.

ACKNOWLEDGEMENTS

There are many people who I wish to thank for support and guidance throughout the completion of this dissertation. I wish to thank the members of my dissertation committee: Dr. John Tweed, Dr. Mark Dunn, Dr. Gordon Melrose, Dr. Feri Farassat and Dr. John Heinbockel for their time and effort in helping to edit this manuscript. In addition, I wish to thank my very good friend Dr. Carryn Bellomo for her emotional support and friendship.

TABLE OF CONTENTS

Page

LIST OF TABLES

LIST OF FIGURES

SECTION 1

INTRODUCTION

Motivated by the desire to solve problems in fracture mechanics and aeroacoustics, numerically efficient algorithms for two classes of hypersingular integral equations are derived. Both classes of integral equations are integral equations of the first kind and contain a Hadamard and a logarithmic singularity along with a weight function $\Delta^{\alpha}(t)=\left(1-t^{2}\right)^{\alpha/2}$ for $\alpha=\pm 1$.

The case $\alpha=1$ is considered in section 2. The form of the integral equation is given by

$$\frac{1}{\pi}\int_{-1}^{1}\Delta^{1}(t)f(t)\left\{\frac{1}{(s-t)^{2}}+B\ln|s-t|+D(s,t)\right\}dt=g(s)\quad\text{for }|s|\le 1 \tag{1.1}$$

where B is a constant, $D(s,t)$ is a bounded function and $g(s)$ is sufficiently smooth. A theoretical argument showing that (1.1) is uniquely solvable is followed by the development of a collocation method and a Galerkin method. Both aforementioned solution techniques are theoretically shown to converge to the unique solution and numerical experiments are conducted to better understand these rates of convergence.

In section 3 equation (1.1) is modified by assuming $\alpha=$ -1. In addition, it differs from the previous class of integral equations because, in order to guarantee uniqueness, it will be shown that two subsidiary conditions are needed. This class of integral equation

---

The *Journal of Computational and Applied Mathematics* was used as the model journal for this dissertation.

arises from physical situations with inherent boundary conditions. The class of integral equations along with the subsidiary conditions is given below

$$\frac{1}{\pi}\int_{-1}^{1}\Delta^{-1}(t)f(t)\left\{\frac{1}{(s-t)^2}+B\ln|s-t|+D(s,t)\right\}dt=g(s)\ \text{ for }\ |s|\le 1 \tag{1.2}$$

with subsidiary conditions

$$W_k f = g_k \ \text{ for }\ k=0,1. \tag{1.3}$$

Two types of subsidiary conditions are considered. The first is the integral type subsidiary condition,

$$W_k f \equiv \int_{-1}^{1} w_k(t)f(t)dt = g_k \ \text{ for }\ k=0,1 \tag{1.4}$$

where $w_k(t)$ is a given weight function. The end-point type subsidiary condition is also considered and is denoted by

$$W_0 f \equiv f(-1)=g_0 \ \text{ or }\ W_1 f \equiv f(1)=g_1. \tag{1.5}$$

A technique similar to the one developed in section 2 is used to give theoretical assurance that equation (1.2) along with subsidiary conditions (1.3) is uniquely solvable. A Galerkin method is shown to converge to the unique solution and therefore, a Galerkin algorithm is developed to solve (1.2) with subsidiary conditions (1.3). In addition, a collocation method is derived and a computationally efficient algorithm is developed. Although the convergence of the collocation method is not, as yet, theoretically proven, numerical experiments demonstrate that the method rapidly converges to the unique solution.

In both classes of integral equations the first integrals are, in general, divergent and must be interpreted in a finite-part sense. In addition, the logarithmic terms have been extracted because although a logarithmic singularity is analytically integrable, it is

numerically difficult to evaluate. In order to solve both classes of integral equations, analytic and numerical techniques are used.

The reason for the interest in these classes of integral equations is that they arise from many physical situations. The remainder of the dissertation is devoted to solving problems in fracture mechanic and aeroacoustics. Three chapters dealing with three distinct, but related, problems in fracture mechanics are presented followed by two problems in aeroacoustics; the study of sound propagation by moving objects.

The first problem in fracture mechanics is the dynamic Griffith crack problem. Here we are concerned with finding the stresses at the end of a finite line discontinuity located in an elastic, homogenous, isotropic medium, which is diffracting an out-of-plane shear wave. This problem has been studied by many others and is well documented. Therefore, we will be able to compare our solution with solutions obtained by others. In addition, this relatively simple problem will serve as a precursor to problems where two Griffith cracks are diffracting an out-of-plane shear wave.

The diffraction of an out-of-plane shear wave by two parallel Griffith cracks is the next problem studied. A related problem, the problem of two symmetric, parallel Griffith cracks, has been extensively studied and it is our goal to expand on this research. With the methods outlined here we are able to determine the stresses for any two disjoint, parallel Griffith cracks and we will compare our results to the results for the special case of symmetric cracks.

The final problem in fracture mechanics is concerned with finding the stresses of two perpendicular Griffith cracks which diffract an out-of-plane shear wave. Very little research exists for this problem and therefore, we expect to gain some new insight into

this problem. Future research will combine the later two problems into one by looking at the diffraction of an out-of-plane shear wave by any two disjoint line cracks.

For the study of aeroacoustics, two problems are considered. The first is the scattering of an acoustic wave by a thin moving wing. Following that is the effects of the scattering of an acoustic wave by a thin moving duct. In both problems we are assuming the motion is uniform in an undisturbed medium. Also, the wing and the duct are both infinitesimally thin. Therefore, linearized acoustics will be used.

The moving wing problem is concerned with finding the total acoustic pressure due to scattering of a known acoustic wave by the interaction of a thin moving wing. Although this problem has few applications, it is a good precursor to the moving duct problem because the moving duct is comprised of two of thin moving strips constructed in such a way that they form a duct.

The scattering of an acoustic wave by a thin moving duct is a problem with many applications. In particular, we will spend a great deal of time focusing on studies involving the effects of a scarf inlet on the radiated sound. A scarf inlet is defined to be an inlet configuration such that the line connecting the upper portion of the inlet with the lower portion of the inlet makes an angle α with vertical. See Figure 1.1

Figure 1.1 Scarf Inlet Geometry

In our case the duct is of finite length, but research exists for the semi-infinite duct. That is, the trailing edges of the duct are extended to negative infinity and the leading edges are constructed as in Figure 1.1. The prominent method for solving the semi-infinite scarf inlet is the Wiener-Hopf technique and some useful results have been obtained. It is our goal to extend these results to the finite duct.

In conclusion, we will see that the methods outlined in the first two sections are ideal for solving problems in fracture mechanics and acoustics. The algorithms are extremely fast and accurate and little modification is required to expand on the topics presented here.

SECTION 2

THE SOLUTION OF HYPERSINGULAR INTEGRAL EQUATIONS

PART I

2.1 Introduction

Consider the following integral equation,

$$\frac{1}{\pi}\int_{-1}^{1}\Delta(t)f(t)\left\{\frac{1}{(s-t)^2}+B\ln|s-t|+D(s,t)\right\}dt=g(s)\ \text{for}\ |s|\le 1 \tag{2.1}$$

where B is a constant, $D(s,t)$ is a bounded, continuous functions, $g(s)$ is sufficiently smooth and

$$\Delta(t)=\sqrt{1-t^2}\ .$$

Due to the $(s-t)^{-2}$ term in the kernel, equation (2.1) is known as a hypersingular integral equation with a Hadamard singularity. The Hadamard singularity in (2.1) is, in general, a divergent integral and must be interpreted in a finite-part sense, which is defined by

$$\int_{-1}^{1}\frac{F(t)}{(s-t)^2}dt=\frac{d}{ds}\int_{-1}^{1}\frac{F(t)}{t-s}dt \tag{2.2}$$

where the integral on the right hand side of (2.2) is a Cauchy principle value integral. Cauchy principle value integrals have been investigated by a number of authors [10, 13, 14, 21, 22]. In particular, Golberg [13, 14] shows that equation (2.1) is uniquely solvable and proves numerical convergence results for a Galerkin method and several collocation methods when $B\equiv 0$. Frenkel [10], on the other hand, developed a Galerkin method for

solving (2.1) but no proof of convergence was given. In this section, the theoretical development to the extension of Golberg will be given which includes the logarithmic singularity. In addition, the numerical technique developed by Frenkel will be improved upon by outlining a more efficient collocation method algorithm.

We begin by noting some well-known definitions and relationships. The Tchebyshev polynomials of the first and second kind, respectively, are defined as,

$$T_n(s) = \cos(n\theta) \tag{2.3}$$

$$U_n(s) = \frac{\sin((n+1)\theta)}{\sin(\theta)} \tag{2.4}$$

where $s = \cos(\theta)$. It is well known [25] that the Tchebyshev polynomials of the first and second kind are related via the Cauchy type integral

$$\frac{1}{\pi}\int_{-1}^{1} \frac{\sqrt{1-t^2}\,U_n(t)}{(t-s)}\,dt = -T_{n+1}(s) \quad \text{for } n \geq 0. \tag{2.5}$$

Furthermore,

$$\frac{d}{ds}T_n(s) = nU_{n-1}(s). \tag{2.6}$$

By using the definition of the finite-part integral the Hadamard term takes the form

$$\frac{1}{\pi}\int_{-1}^{1} \frac{\sqrt{1-t^2}\,U_n(t)}{(s-t)^2}\,dt = -(n+1)U_n(s) \quad \text{for } n \geq 0. \tag{2.7}$$

Equation (2.7) suggests that (2.1) may be solved by approximating the unknown solution, $f(t)$, in a series of Tchebyshev polynomials of the second kind, i.e.

$$f(t) = \sum_{n=0}^{M} f_n U_n(t).$$

Numerical experiments have shown this to be true and it is our goal now to theoretically substantiate this claim.

2.2 Fredholm Theory

The first task will be to show that equation (2.1) is equivalent to an integral equation of the second kind on a suitable Hilbert space and thus, governed by Fredholm theory. To that end, we introduce the following operators $\mathcal{H}$, $\mathcal{L}$, and $\mathcal{D}$.

Definition 2.1. The Hilbert space H is defined to be the space of real-valued, measurable functions

$$H=\left\{f:[-1,1]\to\mathcal{R}\mid\int_{-1}^{1}\left(1-t^{2}\right)^{1/2}f^{2}(t)dt<\infty\right\} \tag{2.8}$$

with inner product

$$\langle f,g\rangle=\int_{-1}^{1}\left(1-t^{2}\right)^{1/2}f(t)g(t)dt \tag{2.9}$$

and norm

$$\|f\|=\sqrt{\langle f,f\rangle}. \tag{2.10}$$

It is well known that the Tchebyshev polynomials of the second kind, $\sqrt{\frac{2}{\pi}}U_n(t)$, form an orthonormal basis for H. Define the following operators:

Definition 2.2. Define the linear operators $\mathcal{H}$, $\mathcal{L}$, $\mathcal{D}$, and $\mathcal{W}$ by

$$\mathcal{H}f=\frac{1}{\pi}\int_{-1}^{1}\frac{\sqrt{1-t^{2}}f(t)}{(s-t)^{2}}dt \tag{2.11}$$

$$\mathcal{L}f=\frac{1}{\pi}\int_{-1}^{1}\sqrt{1-t^{2}}\,f(t)\ln|s-t|dt \tag{2.12}$$

$$\mathcal{D}f=\frac{1}{\pi}\int_{-1}^{1}\sqrt{1-t^{2}}f(t)D(s,t)dt \tag{2.13}$$

$$\mathcal{W} = B\mathcal{L} + \mathcal{D} \tag{2.14}$$

respectively, where B is a constant.

By virtue of equation (2.7) it is clear that

$$\mathcal{H} U_n = -(n+1)U_n \text{ for } n \geq 0 \tag{2.15}$$

is an unbounded operator. However, Golberg [13] shows that the operator (2.11) has a bounded, right inverse $\mathcal{H}^I$. Furthermore, he showed that the nullspace of $\mathcal{H}^I$, $N(\mathcal{H}^I) = 0$. Therefore, for every $g \in H$, the special case of (2.1) for which $B = D = 0$ has a unique solution $f \in H$.

Now the solution of equation (2.1) will be studied. In operator notation, (2.1) takes the form

$$\mathcal{H}f + \mathcal{W}f = g \tag{2.16}$$

It should be noted that the operator $\mathcal{D}$ is assumed to contain a continuous kernel and is therefore compact [23]. Furthermore, since $\mathcal{L}$ contains a weakly singular kernel, it too is compact [23] and by the linearity of the operators $\mathcal{L}$ and $\mathcal{D}$, $\mathcal{W}$ is compact. Finally, since $\mathcal{H}^I$ is bounded, $\mathcal{H}^I\mathcal{W}$ is compact and equation (2.16) is equivalent to the Fredholm equation

$$f + \mathcal{H}^I\mathcal{W}f = \mathcal{H}^I g. \tag{2.17}$$

The solvability of (2.16) may therefore be determined from the classical Fredholm theory. In particular, (2.17) has a unique solution if and only if $N(I + \mathcal{H}^I\mathcal{W}) = 0$. This condition is assumed to hold and hence, (2.16) or equivalently, (2.1) has a unique solution $f \in H$ for every $g \in H$. Now that a unique solution exists, the convergence of the Galerkin method is discussed.

2.3 Galerkin Method

The convergence of the Galerkin method relies heavily on the fact that the operator $\mathcal{W}$ is compact. Using this fact, the convergence argument developed by Golberg follows immediately. In order to be thorough, the method he uses is outlined below.

Approximate the solution of (2.1) by a finite expansion of Tchebyshev polynomials of the second kind, $U_n(t)$, $n = 0,1,2,\ldots, M$. That is,

$$f^{(M)}(t) = \sum_{n=0}^{M} f_n U_n(t) \tag{2.18}$$

Define the residue r_M by

$$r_M = (\mathcal{H} + \mathcal{W}) f^{(M)} - g \tag{2.19}$$

and determine the coefficients f_n, by requiring that

$$\langle r_M, U_m \rangle = 0 \text{ for } m = 0,1,\ldots, M \tag{2.20}$$

This yields the $M+1$ linear equations

$$\sum_{n=0}^{M} f_n \left[-(n+1)\langle U_n, U_m \rangle + \langle \mathcal{W} U_n, U_m \rangle \right] = \langle g, U_m \rangle \text{ for } m = 0,1,\ldots, M \tag{2.21}$$

It is now shown that for sufficiently large M, (2.21) has a unique solution and that the corresponding sum converges in mean to the unique solution f. That is,

$$\lim_{M\to\infty} \left\| f - f^{(M)} \right\| = 0. \tag{2.22}$$

This is done by reformulating (2.21) in a fashion analogous to that used by Golberg [13].

Let P_M be the orthogonal projection operator

$$P_M f = \frac{2}{\pi} \sum_{n=0}^{M} \langle f, U_n \rangle U_n \tag{2.23}$$

Then the orthogonality conditions

$$\langle r_M, U_m \rangle = 0 \text{ for } m = 0,1,\ldots, M \tag{2.24}$$

are equivalent to $P_M r_M = 0$ or

$$P_M\left(\mathcal{H}f^{(M)} + \mathcal{W}f^{(M)} - g\right) = P_M\mathcal{H}f^{(M)} + P_M\mathcal{W}f^{(M)} - P_M g = 0 \tag{2.25}$$

Note that $\mathcal{H}f^{(M)} \in span\{U_n\}_{n=0}^{M}$, therefore $P_M\mathcal{H}f^{(M)} = \mathcal{H}f^{(M)}$. Hence, $f^{(M)}$ satisfies

$$\mathcal{H}f^{(M)} + P_M\mathcal{W}f^{(M)} = P_M g \tag{2.26}$$

Clearly, (2.26) has a solution if and only if $f^{(M)}$ satisfies

$$f^{(M)} + \mathcal{H}^I P_M \mathcal{W}f^{(M)} = \mathcal{H}^I P_M g \tag{2.27}$$

According to Baker [3], in order to see that $f^{(M)}$ has the property (2.22), it is sufficient to show that

$$\lim_{M\to\infty}\left\|\mathcal{H}^I\mathcal{W} - \mathcal{H}^I P_M \mathcal{W}\right\| = 0 \text{ and } \lim_{M\to\infty}\left\|\mathcal{H}^I g - \mathcal{H}^I P_M g\right\| = 0 \tag{2.28}$$

Since $\mathcal{H}^I$ is bounded, it is sufficient to show that

$$\lim_{M\to\infty}\left\|\mathcal{W} - P_M\mathcal{W}\right\| = 0 \text{ and } \lim_{M\to\infty}\left\|g - P_M g\right\| = 0 \tag{2.29}$$

The limits in (2.29) are valid from the fact that $\{U_n\}_{n=0}^{\infty}$ are complete in H and $\mathcal{W}$ is compact. Hence, the Galerkin method determined by (2.18) and (2.20) provides a convergent numerical scheme for solving the integral equation (2.1)

2.4 Collocation Method

In the collocation method $f(t)$ is approximated as in (2.18),

$$f^{(M)}(t) = \sum_{n=0}^{M} f_n U_n(t)$$

and coefficients f_n are determined by the $M+1$ equations

$$r_M(t_m)=0,\ \ t_m \in[-1,1] \text{ and } m=0,1,\ldots,M \tag{2.30}$$

where the t_m are suitably chosen collocation points. Golberg [13] proves that the collocation method converges to the unique solution when the collocation points are chosen to be the zeros of $T_{M+1}(x)$ or the zeros of $U_{M+1}(x)$.

2.5 Galerkin Method Algorithm

In this section, the Galerkin algorithm is outlined. As denoted in the theory, the unknown solution of (2.1) is approximated by a finite expansion of the Tchebyshev polynomials of the second kind,

$$f(t)=\sum_{n=0}^{M} f_n U_n(t). \tag{2.31}$$

Substituting (2.31) into a modified (2.1) yields,

$$\sum_{n=0}^{M} f_n \int_{-1}^{1} \Delta(t)U_n(t)\left\{\frac{A}{(s-t)^2}+B\ln|s-t|+D(s,t)\right\}dt=g(s) \tag{2.32}$$

where $\Delta(t)=\sqrt{1-t^2}$ and $A\neq 0$. Hence, for $m=0,1,\ldots M$

$$\begin{aligned}&\sum_{n=0}^{M} f_n \int_{-1}^{1}\int_{-1}^{1} \Delta(t)\Delta(s)U_n(t)U_m(s)\left\{\frac{A}{(s-t)^2}+B\ln|s-t|+D(s,t)\right\}dtds \\ &=\int_{-1}^{1}\Delta(s)U_m(s)g(s)ds\end{aligned} \tag{2.33}$$

In order to set up the corresponding matrix equation, each term in (2.33) will be considered separately.

The finite-part integral is approximated by

$$\begin{aligned}
&\sum_{n=0}^{M} f_n \int_{-1}^{1}\int_{-1}^{1} \Delta(t)\Delta(s)U_n(t)U_m(s)\frac{A}{(s-t)^2}\,dsdt \\
&= A\sum_{n=0}^{M} f_n \int_{-1}^{1} \Delta(s)U_m(s)\int_{-1}^{1} \Delta(t)U_n(t)\frac{1}{(s-t)^2}\,dtds \\
&= A\sum_{n=0}^{M} f_n \int_{-1}^{1} \Delta(s)U_m(s)\left[-\pi(n+1)U_n(s)\right]ds \\
&= -A\pi\left(\frac{\pi}{2}\right)\sum_{n=0}^{M} f_n(n+1)\delta_{mn}\,.
\end{aligned} \tag{2.34}$$

In evaluating the logarithmic integral use is made of the formulas

$$\ln|s-t| \approx -\sum_{l=0}^{\infty} \nu_l T_l(t)T_l(s), \text{ where } \nu_l = \begin{cases} \ln 2 & l=0 \\ 2/l & l\geq 1 \end{cases} \tag{2.35}$$

and

$$\int_{-1}^{1} \Delta(s)U_m(s)T_l(s)ds = \frac{\pi}{2}\left\{\delta_{ml} - \delta_{m+2\,l}\right\}. \tag{2.36}$$

Hence,

$$\begin{aligned}
&B\sum_{n=0}^{M} f_n \int_{-1}^{1}\int_{-1}^{1} \Delta(t)\Delta(s)U_n(t)U_m(s)\ln|s-t|dtds \\
&= -B\sum_{n=0}^{M} f_n \sum_{l=0}^{\infty} \nu_l \int_{-1}^{1}\int_{-1}^{1} \Delta(t)\Delta(s)U_n(t)U_m(s)T_l(t)T_l(s)dtds \\
&= -B\sum_{n=0}^{M} f_n \sum_{l=0}^{\infty} \nu_l \int_{-1}^{1} \Delta(t)U_n(t)T_l(t)dt \int_{-1}^{1} \Delta(s)U_m(s)T_l(s)ds \\
&= -B\left(\frac{\pi}{2}\right)^2 \sum_{n=0}^{M} f_n \sum_{l=0}^{\infty} \nu_l \left\{\delta_{nl} - \delta_{n+2\,l}\right\}\left\{\delta_{ml} - \delta_{m+2\,l}\right\} \\
&= -B\left(\frac{\pi}{2}\right)^2 \sum_{n=0}^{M} f_n \left\{(\ln 2)\delta_{m0}\delta_{n0} + \frac{2\delta_{mn}}{m}\left(1-\delta_{m0}\right) + \frac{2\delta_{mn}}{m+2} - \frac{2}{m}\delta_{m\,n+2} - \frac{2}{n}\delta_{m+2\,n}\right\}.
\end{aligned} \tag{2.37}$$

By expanding the regular part of the kernel in the Tchebyshev expansion,

$$D(s,t) = \sum_{k,l=0}^{M} d_{kl} U_k(s)U_l(t) \tag{2.38}$$

where

$$d_{kl} = \frac{4}{\pi}\int_{-1}^{1}\int_{-1}^{1}\Delta(s)\Delta(t)D(s,t)U_k(s)U_l(t)dsdt\,. \tag{2.39}$$

we can write the bounded integral as

$$\begin{aligned}
&\sum_{n=0}^{M} f_n \int_{-1}^{1}\int_{-1}^{1}\Delta(t)\Delta(s)U_n(t)U_m(s)\sum_{k,l=0}^{M} d_{kl}U_k(s)U_l(t)dtds \\
&= \sum_{n=0}^{M} f_n \sum_{k,l=0}^{M} d_{kl}\int_{-1}^{1}\Delta(t)U_n(t)U_l(t)dt\int_{-1}^{1}\Delta(s)U_m(s)U_k(s)ds \\
&= \left(\frac{\pi}{2}\right)^2 \sum_{n=0}^{M} f_n d_{mn}
\end{aligned} \tag{2.40}$$

Finally, the right-hand side becomes

$$\begin{aligned}
&\int_{-1}^{1}\Delta(s)U_m(s)g(s)ds \\
&= \int_{-1}^{1}\Delta(s)U_m(s)\sum_{k=0}^{M} g_k U_k(s)ds \\
&= \frac{\pi}{2}g_m
\end{aligned} \tag{2.41}$$

Therefore, the matrix equation to be solved is given by

$$\sum_{n=0}^{M}\left[-A\pi(n+1)\delta_{mn} - B\frac{\pi}{2}\gamma_{mn} + \frac{\pi}{2}d_{mn}\right]f_n = g_m \quad \text{for } m = 0,1,\ldots,M \tag{2.42}$$

where

$$\begin{aligned}
\gamma_{mn} &= (\ln 2)\delta_{m0}\delta_{n0} + \frac{2\delta_{mn}}{m}\left(1-\delta_{m0}\right) + \frac{2\delta_{mn}}{m+2} - \frac{2}{m}\delta_{mn+2} - \frac{2}{n}\delta_{m+2n} \\
d_{mn} &= \int_{-1}^{1}\int_{-1}^{1}\Delta(s)\Delta(t)U_m(s)U_n(t)D(s,t)dsdt \\
g_m &= \int_{-1}^{1}\Delta(s)U_m(s)g(s)ds.
\end{aligned} \tag{2.43}$$

Now we need to approximate the regular part and the right-hand side matrix components. This is accomplished by using a modified Tchebyshev quadrature. Hence,

$$d_{mn} = \int_{-1}^{1}\int_{-1}^{1} \Delta(s)\Delta(t)D(s,t)U_m(s)U_n(t)dsdt$$
$$\approx \left(\frac{1}{NQ+1}\right)^2 \sum_{i,j=0}^{NQ} \left[T_n(x_i) - T_{n+2}(x_i)\right]\left[T_m(x_j) - T_{m+2}(x_j)\right]D(x_i,x_j) \tag{2.44}$$

and

$$g_m = \int_{-1}^{1} \Delta(s)U_m(s)g(s)ds$$
$$\approx \frac{1}{NQ+1}\sum_{j=0}^{NQ}\left[T_m(x_j) - T_{m+2}(x_j)\right]g(x_j) \tag{2.45}$$

where

$$x_i = \cos\left[\frac{2i+1}{2NQ+2}\pi\right] \text{ for } i = 0,1,\ldots,NQ. \tag{2.46}$$

2.6 Collocation Method Algorithm

The Galerkin method requires the evaluation of double integrals for the bounded part of the kernel and a single integration for the right-hand side forcing function. The collocation method, on the other hand, requires only one numerical integration of the bounded part of the kernel. Therefore, the collocation method is computationally more efficient than the Galerkin method. A collocation algorithm for solving equation a modified (2.1) is now developed.

The method described here will make use of the following analytic results.

$$\int_{-1}^{1} \Delta(t)\frac{U_n(t)}{(s-t)^2}dt = -\pi(n+1)U_n(s) \text{ for } n \geq 0 \text{ and } |s| \leq 1 \tag{2.47}$$

$$\int_{-1}^{1} \Delta(t)U_n(t)\ln|s-t|dt = \frac{\pi}{2}\begin{cases} \dfrac{T_2(s)}{2} - \ln 2 & \text{for } n = 0 \\ \dfrac{T_{n+2}(s)}{n+2} - \dfrac{T_n(s)}{n} & \text{for } n \geq 1 \end{cases} \text{ for } |s| \leq 1 \tag{2.48}$$

Let the unknown function, $f(t)$, be approximated by a finite expansion of Tchebyshev polynomials of the second kind.

$$f(t)=\sum_{n=0}^{M} f_n U_n(t) \tag{2.49}$$

Substituting (2.49) into the modified integral equation (2.1) yields

$$\sum_{n=0}^{M} f_n \int_{-1}^{1} \Delta(t) U_n(t) \left\{ \frac{A}{(s-t)^2} + B\ln|s-t| + D(s,t) \right\} dt = g(s) \tag{2.50}$$

Now, we will evaluate equation (2.50) at the collocation points suggested by Golberg [13],

$$x_i = \cos\left(\frac{i+1}{M+2}\pi \right) \text{ for } i = 0,1,\ldots,M. \tag{2.51}$$

With the use of (2.47) and (2.48), the integral equation is approximated by the linear algebraic system below,

$$\sum_{n=0}^{M} f_n \left(\alpha_{ni} + B\gamma_{ni} + \beta_{ni} \right) = g_i; \text{ for } i = 0,1,2,\ldots,M \tag{2.52}$$

where

$$\alpha_{ni} = -\pi(n+1)U_n(x_i) \tag{2.53}$$

$$\gamma_{ni} = \begin{cases} \dfrac{\pi}{4}\left(T_2(x_i) - \ln 4\right) & \text{for } n = 0 \\ \dfrac{\pi}{2}\left(\dfrac{T_{n+2}(x_i)}{n+2} - \dfrac{T_n(x_i)}{n} \right) & \text{for } n \geq 1 \end{cases} \tag{2.54}$$

$$\beta_{ni} = \int_{-1}^{1} \Delta(t) U_n(t) D(x_i,t)\, dt \tag{2.55}$$

$$g_i = g(x_i). \tag{2.56}$$

In order to complete the collocation algorithm, a numerical integration scheme must be used to evaluate the integral. The scheme is given by a modified Tchebyshev quadrature formula,

$$\begin{aligned}\beta_{n,i} &= \int_{-1}^{1} \Delta(t) U_n(t) D(x_i, t) dt \\ &\approx \frac{\pi}{2NQ+2} \sum_{j=0}^{NQ} D(x_i, t_j) \left[T_n(t_j) - T_{n+2}(t_j) \right]\end{aligned} \tag{2.57}$$

where the quadrature nodes are located at

$$t_j = \cos\left(\frac{2j+1}{2NQ+2} \pi \right) \text{ for } j = 0,1,2,\ldots, NQ. \tag{2.58}$$

2.7 Numerical Results

In this section a specific example is used to illustrate and compare the above algorithms for accuracy and computational efficiency. Due to fewer numerical integrations, the collocation method is more computationally efficient. However, the degree of efficiency has not been determined. An illustrative example with some later relevance is given. We wish to solve the following integral equation

$$\int_{-1}^{1} \sqrt{1-t^2} f(t) \frac{k H_1^{(2)}(k|s-t|)}{|s-t|} dt = k \cos\alpha \, e^{iks\cos\alpha} \text{ for } |s| \le 1 \tag{2.59}$$

where

$$H_\lambda^{(2)}(x) = J_\lambda(x) - i Y_\lambda(x)$$

is the Hankel function of the second kind of order λ. J_λ and Y_λ are the Bessel functions of the first and second kind, respectively.

Clearly we have to put this in the form of (2.1). To do this we will isolate the singular behavior of the kernel in (2.59) by expanding the kernel for $|s-t| << 1$. This yields,

$$\frac{kH_1^{(2)}(k|s-t|)}{|s-t|} = \frac{2i}{\pi}\frac{1}{(s-t)^2} - \frac{ik^2}{\pi}\ln|s-t| - \frac{ik^2}{\pi}\left(\ln\frac{k}{2} + \gamma - \frac{1}{2} + \frac{i\pi}{2}\right) + O\left(|s-t|^2\right)$$

where $\gamma \approx .57721566490153$ is Euler's constant. By using this expansion, equation (2.59) takes the form

$$\frac{1}{\pi}\int_{-1}^{1}\sqrt{1-t^2}\,f(t)\left\{\frac{2i}{(s-t)^2} - ik^2\ln|s-t| + D(s,t)\right\}dt = k\cos\alpha\, e^{iks\cos\alpha} \qquad (2.60)$$

where

$$D(s,t) = \pi\frac{kH_1^{(2)}(k|s-t|)}{|s-t|} - \frac{2i}{(s-t)^2} + ik^2\ln|s-t| = O(1) + O\left(|s-t|^2\right). \qquad (2.61)$$

In order to compare the two methods the following values will be used: $k = 3\pi$ and $\alpha = 0$. The first set of results is located in Table 2.1. This table shows the magnitude of each vector component in the expansions of the Galerkin method and collocation method followed by their difference for the case $M = 20$. The computational time necessary to complete this case is negligible and therefore a more detailed study of the time requirements is necessary. In Table 2.2 the computational time, in seconds, required to complete each case is given along with the number of terms taken in the expansion.

Table 2.1
Term by term comparison of the solution vectors obtain by the Galerkin method and the collocation method

n	Galerkin method: Magnitude of the n^{th} component $\|f_n\|$	Collocation method: Magnitude of the n^{th} component $\|g_n\|$	Difference $\| \|f_n\| - \|g_n\| \|$
0	1.40E-01	1.39E-01	8.43E-04
1	3.99E-01	3.96E-01	2.26E-03
2	3.83E-01	3.80E-01	2.79E-03
3	7.40E-01	7.36E-01	3.86E-03
4	5.16E-01	5.12E-01	4.39E-03
5	4.88E-01	4.85E-01	2.90E-03
6	5.46E-01	5.44E-01	2.28E-03
7	8.69E-01	8.63E-01	5.29E-03
8	5.83E-01	5.78E-01	4.39E-03
9	4.30E-01	4.26E-01	4.38E-03
10	2.28E-01	2.25E-01	2.99E-03
11	1.14E-01	1.12E-01	2.01E-03
12	5.00E-02	4.89E-02	1.14E-03
13	1.95E-02	1.89E-02	5.94E-04
14	7.29E-03	7.00E-03	2.87E-04
15	2.35E-03	2.23E-03	1.24E-04
16	7.68E-04	7.16E-04	5.23E-05
17	2.14E-04	1.95E-04	1.93E-05
18	6.22E-05	5.50E-05	7.18E-06
19	1.54E-05	1.30E-05	2.38E-06
20	3.90E-06	3.43E-06	4.67E-07

From Table 2.2 it is clear that for large expansions, the Galerkin method is far more computationally expensive than the collocation method. In some of the case studies later in this dissertation, we will show that number of terms needed in the expansion exceeds 100. In that case, the Galerkin method requires over 2 minutes to execute and it implements a do loop with 10E8 multiplication, whereas the collocation method requires only 10E6 multiplication and about 2 seconds to execute.

Table 2.2
Time, measured in seconds, required to execute each method with varying number of terms in the solution expansion

No. of terms	Galerkin method Execution time	Collocation method Execution time
10	0.06	0.05
20	0.33	0.06
30	1.54	0.16
40	3.63	0.33
50	9.06	0.54
60	17.90	0.83
70	32.24	1.15
80	54.11	1.37
90	85.12	1.64
100	130.95	1.98
110	189.05	2.41
120	266.82	2.96
140	493.45	4.23
160	840.85	5.83

To further test the accuracy of the two methods, consider Table 2.3. For fixed $k = 40$, $\alpha = 0$, the i^{th} vector component with the maximum relative percentage between the two methods is computed along with the vector location of the maximum error for varying number of terms used in the expansion.

Assuming that the solution has converged when the maximum error between the two methods is less than 2%, the next step is to try to relate the number of terms required in the expansion to the parameter k. The next table does just that. Varying the parameter k and holding $\alpha = \pi / 2$ fixed, the number of terms in the expansion required to produce a maximum relative error of less than 2% between the two methods is determined. Table 2.4 suggests that $M \approx 2k$ will produce the desired convergence.

Table 2.3
Maximum relative percentage error between the Galerkin method and collocation method for varying number of terms in the solution expansion

No. of Terms	Max. error location: i	Galerkin $\lvert f_i \rvert$	Collocation $\lvert g_i \rvert$	Max relative % Error
20	18	8.81E-10	3.09E-09	250.86
25	22	1.74E-09	7.57E-10	56.45
30	28	1.63E-09	5.74E-10	64.80
35	34	1.65E-09	8.27E-10	49.77
40	36	2.01E-09	1.23E-09	38.77
45	38	1.61E-09	1.05E-09	34.52
50	38	1.46E-09	1.15E-09	21.45
55	38	1.40E-09	1.20E-09	14.29
60	38	1.36E-09	1.22E-09	10.05
65	38	1.34E-09	1.24E-09	7.37
70	38	1.33E-09	1.25E-09	5.58
75	38	1.32E-09	1.26E-09	4.33
80	38	1.31E-09	1.26E-09	3.43
85	38	1.30E-09	1.27E-09	2.78
90	38	1.30E-09	1.27E-09	2.28
95	38	1.30E-09	1.27E-09	1.90
100	38	1.30E-09	1.27E-09	1.60
105	38	1.29E-09	1.28E-09	1.36
110	38	1.29E-09	1.28E-09	1.16
115	38	1.29E-09	1.28E-09	1.01
120	38	1.29E-09	1.28E-09	0.88
125	38	1.29E-09	1.28E-09	0.77

Finally, to see if $M = 2k$ is indeed a good stopping criterion, Table 2.5 shows the relative change in the i^{th} component by letting $M = 2k$. This is done by evaluating the i^{th} component using $M = 2k$ and $M = 2k + 20$ terms in the approximation and determining the relative percentage change between the two. Furthermore, from Table 2.3, the maximum error between the two methods seems to occur on about the k^{th} term.

Therefore, the change in the k^{th} term is considered. Table 2.5 gives the relative percentage error of taking an additional 20 terms on the i^{th} term of the solution.

Table 2.4
For varying k, the number of terms required to obtain a maximum relative error of less than 2% between the solutions obtained by the Galerkin and collocation methods

k	No. of terms required	Max. relative % Error
10	20	1.05
12	24	1.56
14	28	1.29
16	32	1.50
18	36	1.50
20	40	1.88
22	49	1.04
24	53	1.29
26	57	1.69
28	61	1.49
30	65	1.53
32	74	1.59
34	78	1.51
36	82	1.67
38	86	1.84
40	90	1.82
42	95	1.99
44	98	1.79
46	103	1.98
48	112	1.98

It is clear from Table 2.5 that $M = 2k$ terms in the expansion will produce the desired accuracy in the solution. Of particular interest is that the collocation method converges faster than the Galerkin method. Therefore, due to the computational efficiency and the rapid convergence, we clearly see that the collocation method is a much better choice.

Table 2.5
The relative percentage error of the i^{th} component of the solution by taking an addition 20 terms in the approximating solution

k	i	**Galerkin** $\frac{\left\|f_i^{(2k+20)}-f_i^{(2k)}\right\|}{\left\|f_i^{(2k)}\right\|}\cdot 100\%$	**Collocation** $\frac{\left\|g_i^{(2k+20)}-g_i^{(2k)}\right\|}{\left\|g_i^{(2k)}\right\|}\cdot 100\%$
10	10	0.81	0.66
12	12	0.69	0.56
14	14	0.88	0.72
16	16	0.95	0.78
18	18	0.81	0.67
20	20	1.03	0.85
22	22	0.98	0.80
24	24	0.90	0.74
26	26	1.10	0.90
28	28	0.96	0.79
30	30	0.97	0.80
32	32	1.11	0.91
34	34	0.94	0.77
36	36	1.03	0.85
38	38	1.07	0.88
40	40	0.92	0.77
42	42	1.07	0.88
44	44	1.02	0.84
46	46	0.93	0.77
48	48	1.08	0.89

SECTION 3

THE SOLUTION OF HYPERSINGULAR INTEGRAL EQUATIONS

PART II

3.1 Introduction

Consider the following finite-part integral equation

$$\frac{1}{\pi}\int_{-1}^{1}\frac{f(t)}{\sqrt{1-t^2}}\left\{\frac{1}{(s-t)^2}+B\ln|s-t|+D(s,t)\right\}dt=g(s)\ \text{ for }\ |s|<1 \tag{3.1}$$

with subsidiary conditions (linear functionals)

$$W_k f=g_k\ \text{ for }\ k=0,1 \tag{3.2}$$

which are typically of the integral type

$$W_k f=\frac{1}{\pi}\int_{-1}^{1}w_k(t)f(t)dt=g_k\ \text{ for }\ k=0,1 \tag{3.3}$$

or of the end-point type

$$W_0 f=f(-1)=g_0\ \text{ or }\ W_1 f=f(1)=g_1. \tag{3.4}$$

The first integral in (3.1) is a finite-part integral, defined by

$$\int_{-1}^{1}\frac{F(t)}{(s-t)^2}dt=\frac{d}{ds}\int_{-1}^{1}\frac{F(t)}{t-s}dt \tag{3.5}$$

where the integral on the right of (3.5) is a Cauchy principal value integral. Equations involving such integrals have been investigated by a number of authors [1, 2, 10, 13, 14] and the approach used here is similar to that developed by Golberg [13].

It is well known that the Tchebyshev polynomials of the first and second kinds, $T_n(x)$ and $U_n(x)$ respectively, are related via the Cauchy type integral

$$\frac{1}{\pi}\int_{-1}^{1}\frac{T_n(t)}{\sqrt{1-t^2}}\frac{1}{t-s}dt=\begin{cases}0, & \text{for } n=0\\ U_{n-1}(s), & \text{for } n\geq 1\end{cases}. \tag{3.6}$$

Hence, applying equation (3.5) to (3.6),

$$\frac{1}{\pi}\int_{-1}^{1}\frac{T_n(t)}{\sqrt{1-t^2}}\frac{1}{(s-t)^2}dt=\begin{cases}0, & \text{for } n=0,1\\ 2C_{n-2}^{2}(s), & \text{for } n\geq 2\end{cases} \tag{3.7}$$

where $C_n^{\lambda}(x)$ are the Gegenbauer polynomials of degree n and parameter λ. The Tchebyshev and Gegenbauer polynomials $\{T_n(x)\}_{n=0}^{\infty}$ and $\{C_n^2(x)\}_{n=0}^{\infty}$ are orthogonal sets of polynomials satisfying the orthogonality conditions

$$\int_{-1}^{1}\frac{T_n(t)T_m(t)}{\sqrt{1-t^2}}dt=\frac{\pi}{\varepsilon_n}\delta_{mn} \quad \text{where } \varepsilon_n=\begin{cases}1 & \text{for } n=0\\ 2 & \text{for } n\geq 1\end{cases} \tag{3.8}$$

and

$$\int_{-1}^{1}(1-t^2)^{3/2}C_m^2(t)C_n^2(t)dt=\frac{\pi}{8}(n+3)(n+1)\delta_{mn}. \tag{3.9}$$

Equation (3.7) suggests that the integral equation with subsidiary conditions may be solved by expanding the unknown solution, $f(t)$, in a series of Tchebyshev polynomials of the first kind, $T_n(t)$, and the right-hand side, $g(s)$, in a series of Gegenbauer polynomials, $C_n^2(s)$. Numerical experiments confirm that this technique works and the convergence of the method is now discussed.

3.2 Fredholm Theory

The goal here is to show that equation (3.1) with conditions (3.2) are equivalent to an integral equation of the second kind on a suitable Hilbert space and are thus governed by Fredholm theory. To that end, define the Hilbert Spaces H_α $(\alpha = 0,1,2)$ and the linear operators $\mathcal{H}$, $\mathcal{L}$, and $\mathcal{D}$.

Definition 3.1. The Hilbert space H_α is defined to be the space of real-valued, measurable functions

$$H_\alpha = \left\{ f : [-1,1] \to \mathcal{R} \mid \int_{-1}^{1} (1-t^2)^{\alpha-1/2} f^2(t)dt < \infty \right\} \tag{3.10}$$

with inner product

$$\langle f, g \rangle_\alpha = \int_{-1}^{1} (1-t^2)^{\alpha-1/2} f(t)g(t)dt \tag{3.11}$$

and norm

$$\|f\|_\alpha = \sqrt{\langle f, f \rangle_\alpha}\,. \tag{3.12}$$

It should be noted that H_α has an orthonormal basis $\left\{ h_n^{(\alpha)} \right\}_{n=0}^{\infty}$ where $h_n^{(0)} = \sqrt{\frac{\varepsilon_n}{\pi}}\, T_n(x)$, $h_n^{(1)} = \sqrt{\frac{2}{\pi}}\, U_n(x)$, and $h_n^{(2)} = \sqrt{\frac{8}{\pi(n+3)(n+1)}}\, C_n^2(x)$, for $n \geq 0$. Now we will define some linear operators.

Definition 3.2. Define the linear operators $\mathcal{H}$, $\mathcal{L}$, and $\mathcal{D}$ by

$$\mathcal{H}f = \frac{1}{\pi} \int_{-1}^{1} \frac{f(t)}{\sqrt{1-t^2}} \frac{1}{(s-t)^2} dt \tag{3.13}$$

$$\mathcal{L}f = \frac{1}{\pi} \int_{-1}^{1} \frac{f(t)}{\sqrt{1-t^2}} \ln|s-t| dt \tag{3.14}$$

and

$$\mathcal{D}f = \frac{1}{\pi}\int_{-1}^{1} \frac{f(t)}{\sqrt{1-t^2}} D(s,t)dt \tag{3.15}$$

respectively.

By virtue of equation (3.7) it is readily seen that

$$\mathcal{H}h_r^{(0)} = \begin{cases} 0, & \text{for } r = 0,1 \\ \sqrt{r^2-1}\, h_{r-2}^{(2)} & \text{for } r \geq 2 \end{cases}. \tag{3.16}$$

Clearly, $\mathcal{H}$ is unbounded when regarded as an operator from H_0 to H_2. This motivates the introduction of a subspace $H \subset H_0$ on which all the operators (3.13) - (3.15) are bounded. The new subspace H is defined as follows:

Definition 3.3. Let $\lambda_0 = \lambda_1 = 1$ and $\lambda_r = \sqrt{r^2-1}$ for $r \geq 2$, then,

$$H = \left\{ f \in H_0 \mid \sum_{r=0}^{\infty} \lambda_r^2 \left\langle f, h_r^{(0)} \right\rangle_0^2 < \infty \right\} \tag{3.17}$$

with inner product

$$\langle f, g \rangle_H = \sum_{r=0}^{\infty} \lambda_r^2 \left\langle f, h_r^{(0)} \right\rangle_0 \left\langle g, h_r^{(0)} \right\rangle_0 \tag{3.18}$$

and norm

$$\|f\|_H = \sqrt{\langle f, f \rangle_H} \ . \tag{3.19}$$

Note that $\left\| h_r^{(0)} \right\|_H = \lambda_r$ and hence, H has an orthonormal basis $\{h_r\}_{r=0}^{\infty}$, where

$$h_r = \frac{1}{\lambda_r} h_r^{(0)} \text{ for } r \geq 0$$

Assume that $g \in H_2$ and $D(s,t)$ satisfies the condition

$$\int_{-1}^{1}\int_{-1}^{1}\frac{(1-s^2)^{3/2}}{(1-t^2)^{1/2}}D^2(s,t)dsdt<\infty. \tag{3.20}$$

Lemma 3.4. $\mathcal{H}$, $\mathcal{L}$, and $\mathcal{D}$ define bounded linear operators from H to H_2. In addition, $\mathcal{L}$ and $\mathcal{D}$ are compact.

Proof:

(i) It is clear that $\mathcal{H}:H\to H_2$ is bounded. To see this, if $f=\sum_{r=0}^{\infty}f_r h_r\in H$ then

$$\begin{aligned}\mathcal{H}f&=\sum_{r=0}^{\infty}f_r\mathcal{H}h_r\\&=\sum_{r=2}^{\infty}f_r h_{r-2}^{(2)}\end{aligned} \tag{3.21}$$

and

$$\begin{aligned}\|\mathcal{H}f\|_2^2&=\sum_{r=2}^{\infty}f_r^2\\&\le\|f\|_H\end{aligned} \tag{3.22}$$

which shows that $\mathcal{H}f\in H_2$ and $\|\mathcal{H}\|\le 1$. Hence $\mathcal{H}$ is bounded.

(ii) To show $\mathcal{L}$ is compact, and hence bounded, it will be sufficient [11] to show that $\sum_{r=0}^{\infty}\|\mathcal{L}h_r\|_2^2<\infty$. It is well known [25] that

$$\frac{1}{\pi}\int_{-1}^{1}\frac{T_r(t)}{\sqrt{1-t^2}}\ln|t-s|dt=-\mu_r T_r(s)\ \text{ where }\ \mu_r=\begin{cases}\ln 2, & \text{for } r=0\\ r^{-1}, & \text{for } r\ge 1\end{cases} \tag{3.23}$$

Hence, $\mathcal{L}h_r=-\mu_r h_r$ and therefore

$$\sum_{r=0}^{\infty}\|\mathcal{L}h_r\|_2^2 = \sum_{r=0}^{\infty}\frac{\mu_r^2\varepsilon_r}{\pi\lambda_r^2}\int_{-1}^{1}(1-s^2)^{3/2}T_r^2(s)ds$$
$$= \sum_{r=0}^{\infty}\frac{\mu_r^2\varepsilon_r}{8\lambda_r^2}\left[6(1+\delta_{0r})-4\delta_{1r}+\delta_{2r}\right] \qquad (3.24)$$
$$= \frac{3}{2}(\ln 2)^2+\frac{31}{48}<\infty$$

hence, $\mathcal{L}$ is compact.

(iii) Since $D(s,t)$ satisfies (3.20), it is a Hilbert Schmidt kernel and hence the corresponding operator $\mathcal{D}$ is compact. □

Observe that if $g=\sum_{r=2}^{\infty}g_r h_{r-2}^{(2)}$ is any element of H_2, then $f=\sum_{r=2}^{\infty}g_r h_r$ belongs to H and $\mathcal{H}f=g$. However, f is not unique since $\mathcal{H}$ has a non-trivial nullspace, $N(\mathcal{H})=span\{h_0,h_1\}$, and this is precisely why the subsidiary conditions (3.2) are needed. The linear functionals W_k, $k=0,1$, appearing in the subsidiary conditions are assumed to be bounded linear functionals from H to R, and are assumed to satisfy the condition

$$(W_0h_0)(W_1h_1)-(W_0h_1)(W_1h_0)\neq 0. \qquad (3.25)$$

By virtue of Riesz' Representation theorem, $W_kf=\langle f,w_k\rangle_H$ for unique $w_k\in H$ and therefore the conditions (3.2) may be written as

$$W_kf=\langle f,w_k\rangle_H$$
$$=\sum_{r=0}^{\infty}f_rw_{rk}=g_k \quad \text{for } k=0,1 \qquad (3.26)$$

where $w_{rk}=W_kh_r$ ($k=0,1$; $r=0,1,2,\ldots$). Additionally, assumption (3.25) takes the form

$$\det(w)=\begin{vmatrix} w_{00} & w_{01}\\ w_{10} & w_{11}\end{vmatrix}\neq 0. \qquad (3.27)$$

It should be observed that while linear functionals of end point type, such as (3.4), are unbounded on H_0 they are bounded on H and are thus, covered by the present theory.

The next stage is to construct an invertible operator which is equivalent to the integral equation (3.1) and its subsidiary conditions (3.2). In order to do this, the introduction of yet another Hilbert space $\hat{H}$ and two additional operators $\mathcal{W}$ and $\mathcal{K}$ are required.

Definition 3.5. $\hat{H}$ is defined to be the Hilbert space

$$\hat{H} = \mathcal{R}^2 \oplus H_2 = \left\{ x = \left(x_0, x_1, x_{(2)} \right) : (x_0, x_1) \in \mathcal{R}^2, x_{(2)} \in H_2 \right\} \tag{3.28}$$

with inner product

$$\langle x, y \rangle_{\hat{H}} = x_0 y_0 + x_1 y_1 + \left\langle x_{(2)}, y_{(2)} \right\rangle_{(2)} \tag{3.29}$$

and norm

$$\|x\|_{\hat{H}} = \sqrt{\langle x, x \rangle_{\hat{H}}} \,. \tag{3.30}$$

Clearly, $\hat{H}$ has an orthonormal basis $\left\{ \hat{h}_n \right\}_{n=0}^{\infty}$ where $\hat{h}_0 = \left(1,0,0_{(2)}\right)$, $\hat{h}_1 = \left(0,1,0_{(2)}\right)$ and $\hat{h}_n = \left(0,0,h_{n-2}^{(2)}\right)$ for $n \geq 2$.

Definition 3.6. Define the linear operators $\mathcal{W}, \mathcal{K} : H \to \hat{H}$ by

$$\mathcal{W} f = \left(W_0 f, W_1 f, \mathcal{H} f \right) \tag{3.31}$$

$$\mathcal{K} f = \left(0,0,[B\mathcal{L} + \mathcal{D}]f\right). \tag{3.32}$$

It will now be shown that $\mathcal{W}$ is a bounded, invertible operator and $\mathcal{K}$ is bounded.

Lemma 3.7. $\mathcal{W} : H \to \hat{H}$ is bounded and has a bounded inverse $\mathcal{W}^I : \hat{H} \to H$.

Proof:

(i) $\mathcal{W} h_r = (W_0 h_r, W_1 h_r, \mathcal{H} h_r) = w_{r0}\hat{h}_0 + w_{r1}\hat{h}_1 + (1-\delta_{r0}-\delta_{r1})\hat{h}_r$.

(ii) Let $f \in H$ then

$$\|\mathcal{W} f\|_{\hat{H}}^2 = |\langle f, w_0\rangle_H|^2 + |\langle f, w_1\rangle_H|^2 + \|\mathcal{H} f\|_2^2$$
$$\leq \left(\|w_0\|_H^2 + \|w_1\|_H^2 + 1\right)\|f\|_H^2.$$

Thus $\mathcal{W} f \in \hat{H}$ and $\mathcal{W}$ is bounded since

$$\|\mathcal{W}\|^2 \leq \|w_0\|_H^2 + \|w_1\|_H^2 + 1$$
$$< \infty.$$

(iii) The matrix of $\mathcal{W}$ is given by $W_{rs} = \langle \mathcal{W} h_r, \hat{h}_s \rangle_{\hat{H}}$. Therefore, in view of (i),

$$W = (W_{rs}) = \begin{pmatrix} w & 0 \\ b & I \end{pmatrix}$$

where $w = (w_{rs})\ (r,s = 0,1)$ and $b = (w_{rs})\ (r = 2,3,...;s = 0,1)$. Since $\det(w) \neq 0$, w has an inverse w^I and therefore W has an inverse given by

$$W^I = (W_{rs}^I) = \begin{pmatrix} w^I & 0 \\ -bw^I & I \end{pmatrix}.$$

(iv) The nullspace of $\mathcal{W} = N(\mathcal{W}) = \{0\}$, For $f \in H$ and $\mathcal{W} f = 0$ then

$$\mathcal{W} f = \mathcal{W}\left(\sum_{r=0}^{\infty} f_r h_r\right)$$
$$= \sum_{s=0}^{\infty}\sum_{r=0}^{\infty} f_r W_{rs}\hat{h}_s = 0$$

$$\Rightarrow \sum_{r=0}^{\infty} f_r W_{rs} = 0$$
$$\Rightarrow f_r = 0.$$

(v) For $g = \sum_{r=0}^{\infty} g_r \hat{h}_r \in \hat{H}$, define $\mathcal{W}^I g = f = \sum_{s=0}^{\infty} f_s h_s$ where $f_s = \sum_{r=0}^{\infty} g_r W_{rs}^I$. Then,

$f_s = g_s$ for $s \geq 2$. Hence, $\sum_{s=2}^{\infty} f_s^2 \leq \sum_{s=0}^{\infty} g_s^2 = \|g\|_{\hat{H}}^2$. Furthermore,

$$\begin{aligned}
\sum_{s=0}^{1} f_s^2 &= \sum_{s=0}^{1} \left(\sum_{r=0}^{\infty} g_r W_{rs}^I \right)^2 \\
&\leq \|g\|_{\hat{H}}^2 \sum_{s=0}^{1} \sum_{r=0}^{\infty} \left(W_{rs}^I \right)^2 \\
&= \|g\|_{\hat{H}}^2 \sum_{s=0}^{1} \left\{ \sum_{r=0}^{1} \left(w_{rs}^I \right)^2 + \sum_{r=2}^{\infty} \left(\sum_{k=0}^{1} -w_{rk} w_{ks}^I \right)^2 \right\} \\
&\leq \|g\|_{\hat{H}}^2 \left\{ \sum_{s=0}^{1} \sum_{r=0}^{1} \left(w_{rs}^I \right)^2 \right\} \left\{ 1 + \sum_{k=0}^{1} \|w_k\|_H^2 \right\}.
\end{aligned}$$

Thus, $\sum_{s=0}^{\infty} f_s^2 \leq A \|g\|_{\hat{H}}^2$ which shows that $f \in H$ and $\mathcal{W}^I$ is bounded.

(vi) The nullspace $N(\mathcal{W}^I) = \{0\}$. To see this,

$$\begin{aligned}
&\mathcal{W}^I g = 0 \\
&\Rightarrow \sum_{r=0}^{\infty} g_r W_{rs}^I = 0 \\
&\Rightarrow g_r = 0 \\
&\Rightarrow g = 0.
\end{aligned}$$

(vii) For $f \in H$, $\mathcal{W}^I(\mathcal{W} f) = f$. To see this,

$$\begin{aligned}
\mathcal{W}^I(\mathcal{W} f) &= \mathcal{W}^I \left(\sum_{p=0}^{\infty} g_p \hat{h}_p \right) \\
&= \mathcal{W}^I \left(\sum_{p=0}^{\infty} \sum_{q=0}^{\infty} f_q W_{qp} \hat{h}_p \right)
\end{aligned}$$

$$= \sum_{s=0}^{\infty}\sum_{q=0}^{\infty}\sum_{p=0}^{\infty} f_q W_{qp} W^I_{ps} h_s$$

$$= \sum_{s=0}^{\infty}\sum_{q=0}^{\infty} f_q \delta_{qs} h_s$$

$$= \sum_{s=0}^{\infty} f_s h_s = f.$$

(viii) Similarly, for $g \in \hat{H}$, $\mathcal{W}(\mathcal{W}^I g) = g$

$$\mathcal{W}(\mathcal{W}^I g) = \mathcal{W}\left(\sum_{p=0}^{\infty} f_p h_p\right)$$

$$= \mathcal{W}\left(\sum_{p=0}^{\infty}\sum_{q=0}^{\infty} g_q W^I_{qp} h_p\right)$$

$$= \sum_{s=0}^{\infty}\sum_{q=0}^{\infty}\sum_{p=0}^{\infty} g_q W^I_{qp} W_{ps} \hat{h}_s$$

$$= \sum_{s=0}^{\infty} g_s \hat{h}_s = g.$$

Thus the proof is complete.

Lemma 3.8. $\mathcal{K}: H \to \hat{H}$ is compact.

Proof: Let $S = B\mathcal{L} + \mathcal{D}$ then $S: H \to H_2$ is compact. Also, since $\mathcal{K}f = (0, 0, Sf)$, it is clear that $\|\mathcal{K}f\|_{\hat{H}} = \|Sf\|_2$. Let f_n converge weakly to f in H as $n \to \infty$. Then since S is compact, $\|Sf_n - Sf\|_2 \to 0$ as $n \to \infty$ and hence, $\|\mathcal{K}f_n - \mathcal{K}f\| \to 0$ as $n \to \infty$. Hence, $\mathcal{K}$ is compact.

With $\mathcal{W}$ and $\mathcal{K}$ defined as in (3.31) and (3.32), integral equation (3.1) with subsidiary conditions (3.2) can be written as an operator equation from H to $\hat{H}$ by

$$\mathcal{W}f + \mathcal{K}f = \hat{g} \text{ for } f \in H \text{ and } \hat{g} = (g_0\, g_1\, g) \in \hat{H} \qquad (3.33)$$

Clearly, (3.33) has a solution if and only if

$$f + \mathcal{W}^I \mathcal{K} f = \mathcal{W}^I \hat{g} \tag{3.34}$$

Since, $\mathcal{W}^I$ is bounded and $\mathcal{K}$ is compact, $\mathcal{W}^I \mathcal{K}$ is also compact and the solvability of (3.34) can be determined from the classical Fredholm theory. In particular, (3.34) has a unique solution if and only if $N(I + \mathcal{W}^I \mathcal{K}) = 0$. It is Assumed that this condition holds and thus (3.33) has a unique solution $f \in H$ for every $\hat{g} \in \hat{H}$. Now the convergence of a Galerkin method is discussed.

3.3 Galerkin Method

In the Galerkin method the unknown function $f(t)$ is approximated by a finite series

$$f^{(M)}(t) = \sum_{n=0}^{M} f_n h_n(t) \tag{3.35}$$

of weighted Tchebyshev polynomials of the first kind $h_n(t) = \frac{1}{\lambda_n}\sqrt{\frac{\varepsilon_n}{\pi}}\, T_n(t)$ for $n = 0, 1, \ldots, M$. Define the residual $\hat{r}_M$ by

$$\hat{r}_M = \mathcal{W} f^{(M)} + \mathcal{K} f^{(M)} - \hat{g} \tag{3.36}$$

and determine the coefficients f_n by requiring that

$$\left\langle \hat{r}_M, \hat{h}_m \right\rangle_{\hat{H}} = 0 \text{ for } m = 0, 1, 2, \ldots M. \tag{3.37}$$

This yields $M + 1$ linear algebraic equations

$$\sum_{n=0}^{M} f_n \left(W_{nm} + K_{nm} \right) = g_m. \tag{3.38}$$

It will now be shown that for large enough M, equation (3.38) has a unique solution and that the corresponding sum $\sum_{n=0}^{M} f_n h_n$ converges in mean to f. That is,

$$\lim_{M\to\infty}\left\|f - f^{(M)}\right\|_H = 0. \tag{3.39}$$

Convergence is shown by reformulating the system (3.38) in a fashion analogous to that used by Golberg in [13].

Let $P_M : \hat{H} \to span\left\{\hat{h}_n\right\}_{n=0}^{M}$ be an orthogonal projection operator, so that for $\hat{g} \in \hat{H}$

$$P_M \hat{g} = \sum_{n=0}^{M} \left\langle \hat{g}, \hat{h}_n \right\rangle_{\hat{H}} \hat{h}_n . \tag{3.40}$$

Thus, $\left\langle \hat{r}_M, \hat{h}_n \right\rangle_{\hat{H}} = 0$ for $n = 0,1,\ldots,M$ if and only if $P_M \hat{r}_M = 0$. Therefore, equation (3.38) is equivalent to the operator equation

$$P_M \mathcal{W} f^{(M)} + P_M \mathcal{K} f^{(M)} = P_M \hat{g} \tag{3.41}$$

and by lemma 3.7, $\mathcal{W} f^{(M)} \in span\left\{\hat{h}_n\right\}_{n=0}^{M}$, therefore $P_M \mathcal{W} f = \mathcal{W} f$. Making use of the previous observations and equation (3.41) leads to the following operator notation

$$\mathcal{W} f^{(M)} + P_M \mathcal{K} f^{(M)} = P_M \hat{g} \tag{3.42}$$

and clearly equation (3.42) has a unique solution if and only if $f^{(M)}$ satisfies

$$f^{(M)} + \mathcal{W}^I P_M \mathcal{K} f^{(M)} = \mathcal{W}^I P_M \hat{g}. \tag{3.43}$$

According to Baker [3] it is sufficient to show that $\lim_{M\to\infty}\left\|\mathcal{W}^I \mathcal{K} - \mathcal{W}^I P_M \mathcal{K}\right\| = 0$ and $\lim_{M\to\infty}\left\|\mathcal{W}^I \hat{g} - \mathcal{W}^I P_M \hat{g}\right\| = 0$. Since, $\mathcal{W}^I$ is bounded however, it is sufficient to show that $\lim_{M\to\infty}\left\|\mathcal{K} - P_M \mathcal{K}\right\| = 0$ and that $\lim_{M\to\infty}\left\|\hat{g} - P_M \hat{g}\right\| = 0$. Recalling that $\left\{\hat{h}_n\right\}_{n=0}^{\infty}$ is complete

in $\hat{H}$ and $\mathcal{K}$ is compact, these previous limits are true. Therefore, the Galerkin method determined by (3.35) and (3.37) provides a convergent numerical scheme for solving the integral equation (3.1) with subsidiary conditions (3.2).

3.4 Galerkin Method Algorithm

The integral equation to be solved is given by

$$\frac{1}{\pi}\int_{-1}^{1}\frac{f(t)}{\Delta(t)}\left\{\frac{A}{(s-t)^2}+B\ln|s-t|+D(s,t)\right\}dt=g(s)\quad\text{for }|s|\le 1 \tag{3.44}$$

with subsidiary conditions,

$$W_0 f = g_0 \text{ and } W_1 f = g_1 \tag{3.45}$$

where $A\neq 0$ and B are constants, $\Delta(t)=\sqrt{1-t^2}$, and W_0 and W_1 are linear functionals.

Expand the unknown function in a Tchebyshev polynomial expansion and the right hand side in a Gegenbauer expansion as follows

$$f(t)=\sum_{n=0}^{M} f_n T_n(t) \text{ and } g(s)=\sum_{m=2}^{M} g_m C_{m-2}^2(s) \tag{3.46}$$

The Gegenbauer polynomials satisfy the following orthogonality condition,

$$\int_{-1}^{1}\Delta^3(t)C_{n-2}^2(t)C_{m-2}^2(t)dt=\frac{\pi}{8}(n^2-1)\delta_{nm}\quad\text{for } n,m\ge 2 \tag{3.47}$$

Now, by equation (3.46) and (3.47) we can rewrite the integral equation (3.44) as follows: for $m = 2, 3,\ldots, M$

$$\frac{8}{\pi(m^2-1)}\sum_{n=0}^{M} f_n\int_{-1}^{1}\Delta^3(s)C_{m-2}^2(s)\int_{-1}^{1}\frac{T_n(t)}{\Delta(t)}\left\{\frac{A}{(s-t)^2}+B\ln|s-t|+D(s,t)\right\}dtds=g_m \tag{3.48}$$

Consider each part of the kernel separately.

The Hadamard part is given first. Define the following $(M-1)\times(M+1)$ matrix

$$\alpha_{mn} = \frac{8A}{\pi(m^2-1)} \int_{-1}^{1} \Delta^3(s) C_{m-2}^2(s) \int_{-1}^{1} \frac{1}{\Delta(t)} \frac{T_n(t)}{(s-t)^2} dtds \tag{3.49}$$

Then,

$$\alpha_{mn} = \begin{cases} 0, & n = 0,1 \\ \dfrac{16A}{m^2-1} \displaystyle\int_{-1}^{1} \Delta^3(s) C_{m-2}^2(s) C_{n-2}^2(s) ds, & n \geq 2 \end{cases} \tag{3.50}$$

Upon simplifying, we see that

$$\alpha_{mn} = \begin{cases} 0, & n = 0,1 \\ 2\pi A \delta_{mn}, & n \geq 2 \end{cases} \tag{3.51}$$

Now the logarithmic term is given below,

$$\beta_{mn} = B \frac{8}{\pi(m^2-1)} \int_{-1}^{1} \Delta^3(s) C_{m-2}^2(s) \int_{a}^{b} \frac{T_n(t)}{\Delta(t)} \ln|s-t| dtds$$

$$= -B \frac{8\mu_n}{\pi(m^2-1)} \int_{-1}^{1} \Delta^3(s) C_{m-2}^2(s) T_n(s) ds$$

where

$$\mu_0 = \ln(2) \text{ and } \mu_n = \frac{1}{n} \text{ for } n \geq 1$$

Thus,

$$\beta_{mn} = B \begin{cases} -\dfrac{3\pi\delta_{m2}}{m^2-1} \ln(2), & n = 0 \text{ and } m \geq 2 \\ -\dfrac{\pi}{2n(m^2-1)} \left\{ (m+1)\delta_{mn+2} - 2m\delta_{mn} + (m-1)\delta_{mn-2} \right\}, & n \geq 1 \text{ and } m \geq 2 \end{cases}$$

Finally the matrix for the bounded, regular part of the kernel is given.

$$D_{mn} = \frac{8}{\pi(m^2-1)} \int_{-1}^{1} \Delta^3(s) C_{m-2}^2(s) \int_{a}^{b} \frac{T_n(t)}{\Delta(t)} D(s,t) dtds$$

In order to approximate the regular part, it will be advantageous for us to use a Gauss-Tchebyshev quadrature since we have an appropriate weight function embedded in the double integral. Hence, define the following quadrature nodes and weights, respectively.

$$t_k = \cos\left(\frac{2k-1}{2NQ_T}\pi\right) \text{ and } \eta_k = \frac{\pi}{NQ_T} \text{ for } k = 1,2,\ldots NQ_T$$

In addition, define the Gauss-Legendre nodes and weights by

$$s_j \text{ and } \omega_j \text{ for } j = 1, 2,\ldots, NQ_L$$

Therefore, for $m = 2, 3,\ldots, M$ and $n = 0, 1, 2, \ldots, M$, we have

$$\begin{aligned} D_{mn} &= \frac{8}{\pi(m^2-1)}\int_{-1}^{1}\int_{-1}^{1}\frac{1}{\Delta(t)}\Delta^3(s)C_{m-2}^2(s)T_n(t)D(s,t)dtds \\ &\approx \frac{8}{\pi(m^2-1)}\frac{\pi}{NQ_T}\sum_{j=1}^{NQ_L}\sum_{k=1}^{NQ_T}\omega_j\Delta^3(s_j)C_{m-2}^2(s_j)T_n(t_k)D(s_j,t_k) \end{aligned} \tag{3.52}$$

Finally, for $m = 2, 3, \ldots, M$, the right hand side vector is given by,

$$\begin{aligned} g_m &= \frac{8}{\pi(m^2-1)}\int_{-1}^{1}\Delta^3(s)C_{m-2}^2(s)g(s)ds \\ &\approx \frac{8}{\pi(m^2-1)}\sum_{j=1}^{NQ_L}\omega_j\Delta^3(s_j)C_{m-2}^2(s_j)g(s_j) \end{aligned}$$

Hence, the integral equation produces $(M-1)$ equations in $(M+1)$ unknowns

$$\sum_{n=0}^{M}\left[\alpha_{mn}+\beta_{mn}+D_{mn}\right]f_n = g_m \text{ for } m = 2,3,\ldots, M$$

This is precisely why the subsidiary conditions are needed. These conditions take the following form

$$W_m f = g_m \text{ for } m = 0, 1$$

and provide the two additional equations

$$W_m f = W_m \sum_{n=0}^{M} f_n T_n(t) \text{ for } m = 0, 1$$

Examples of subsidiary conditions

1. $f(-1) = g_0 \Rightarrow \sum_{n=0}^{M} (-1)^n f_n = g_0$

2. $f(1) = g_1 \Rightarrow \sum_{n=0}^{M} f_n = g_1$

3. $\int_{-1}^{1} w(t) f(t) dt = g_0 \Rightarrow \sum_{n=0}^{M} w_{0n} f_n = g_0$

where $w_{0n} = \int_{-1}^{1} w(t) T_n(t) dt = \frac{\pi}{NQ_T} \sum_{k=1}^{NQ_T} \Delta(t_k) w(t_k) T_n(t_k)$

3.5 Collocation Method Algorithm

A theoretical proof of the convergence of the collocation method has not yet been given. However, it has been observed that numerical experiments yield valid solutions. Furthermore, the computational efficiency of the collocation method appears to be far superior to that of the Galerkin method. Therefore, a collocation algorithm will be introduced and numerical experiments conducted to verify that valid solutions are obtained.

Consider the integral equation

$$\int_{-1}^{1} \frac{f(t)}{\Delta(t)} \left\{ \frac{A}{(s-t)^2} + B \ln|s-t| + D(s,t) \right\} dt = g(s) \text{ for } |s| \le 1 \tag{3.53}$$

with subsidiary conditions

$$W_k f = g_k \text{ for } k = 0, 1 \tag{3.54}$$

where A and B are constants, D is a bounded function and $\Delta(t)=\sqrt{1-t^2}$.

We begin by approximating the unknown solution by a finite expansion of Tchebyshev polynomials of the first kind

$$f(t)=\sum_{n=0}^{M} f_n T_n(t). \tag{3.55}$$

With this approximation the subsidiary conditions (3.54) take the form

$$\sum_{n=0}^{M} f_n w_{ni} \quad \text{for } i=0,1$$

where

$$w_{ni}=W_i(t_n)$$

In particular, the integral type subsidiary condition can be written by

$$w_{ni}=\int_{-1}^{1}\frac{1}{\Delta(t)}w_i(t)T_n(t)dt$$

and for the left end condition and the right end conditions, respectively, we have

$$w_{ni}=(-1)^n \quad \text{and} \quad w_{ni}=1$$

By making use of the following analytic and numerical results, we will reduce (3.53) and (3.54) to a system of algebraic equations.

$$\int_{-1}^{1}\frac{1}{\Delta(t)}\frac{T_n(t)}{(s-t)^2}dt=\begin{cases}0, & n=0,1\\ 2\pi C_{n-2}^2(s), & n\geq 2\end{cases} \tag{3.56}$$

$$\int_{-1}^{1}\frac{1}{\Delta(t)}T_n(t)\ln|s-t|dt=-\pi\mu_n T_n(s) \quad \text{for } n=0,\,1,\,\ldots,\,M \tag{3.57}$$

where $\mu_0=\ln 2$ and $\mu_n=\dfrac{1}{n}$ for $n\geq 1$

$$\int_{-1}^{1} \frac{1}{\Delta(t)} T_n(t) D(s,t)dt \approx \frac{\pi}{NQ_T} \sum_{k=1}^{NQ_T} T_n(t_k) D(s,t_k) \tag{3.58}$$

where $t_k = \cos\left(\frac{2k-1}{2NQ_T}\pi\right)$ for $k = 1, 2, \ldots, NQ_T$.

Combining equations (3.55) - (3.58) yields the following system of equations.

$$\sum_{n=0}^{M} f_n K_n(s) = g(s) \text{ for } s \in (-1,1) \tag{3.59}$$

where

$$K_n(s) = 2\pi A(1-\delta_{n0})(1-\delta_{n1})C_{n-2}^2(s) - \pi B\mu_n T_n(s) + D_n(s) \tag{3.60}$$

and $D_n(s)$ is given by

$$D_n(s) = \int_{-1}^{1} \frac{1}{\Delta(t)} T_n(t) D(s,t)dt. \tag{3.61}$$

With a suitable choice of collocation points, s_i for $i = 2,3,\ldots, M$, equation (3.59) together with the subsidiary conditions (3.54) yields the following linear system of equations for the unknown coefficients, f_n.

$$\begin{aligned} &\sum_{n=0}^{M} f_n w_{ni} = g_i \text{ for } i = 0,1 \\ &\sum_{n=0}^{M} f_n K_n(s_i) = g(s_i) \text{ for } i = 2,3,\ldots, M \end{aligned} \tag{3.62}$$

We will compare the use of two choices of collocation nodes. The first set, denoted $s_i^{(0)}$, are taken to be the zeros of $T_{M-1}(x)$ and the second set, denoted $s_i^{(1)}$, are taken to be the zeros of $U_{M-1}(x)$.

$$s_i^{(0)} = \cos\left(\frac{2i-3}{2M-2}\pi\right) \text{ for } i = 2,3,\ldots, M \tag{3.63}$$

and

$$s_i^{(1)} = \cos\left(\frac{i-1}{M}\pi\right) \text{ for } i = 2,3,\ldots,M \tag{3.64}$$

3.6 Numerical Results

In order to test the veracity of the technique developed here, we will construct examples with known analytic solution for varying subsidiary conditions and right hand sides. The examples will be constructed from the following equation

$$\int_{-1}^{1} \frac{f(t)}{\sqrt{1-t^2}}\left\{\frac{1}{(s-t)^2} + \ln|s-t| + 2(s-t)^2\right\}dt = g(s) \text{ for } |s| \le 1 \tag{3.65}$$

with subsidiary condition

$$W_0 f = g_0 \text{ and } W_1 f = g_1. \tag{3.66}$$

Firstly, we will impose two end-point subsidiary conditions. The equation to solve is given by

$$\int_{-1}^{1} \frac{f(t)}{\sqrt{1-t^2}}\left\{\frac{1}{(s-t)^2} + \ln|s-t| + 2(s-t)^2\right\}dt = g(s) \text{ for } |s| \le 1 \tag{3.67}$$

with subsidiary conditions

$$f(-1) = f(1) = 0 \tag{3.68}$$

and

$$g(s) = \frac{16\pi}{(5-4s)^2} + \pi\ln\left(\frac{5-4s}{8}\right) + \frac{\pi}{12}\left(20\ln 2 - 5 + 24s - 16s^2\right). \tag{3.69}$$

Equations (3.67) - (3.69) have the closed form solution

$$\begin{aligned} f(t) &= \frac{3}{5-4t} - \frac{5}{3} - \frac{4}{3}t \\ &= \sum_{n=0}^{\infty} \varepsilon_n 2^{-n} T_n(t) - \frac{5}{3}T_0(t) - \frac{4}{3}T_1(t) \end{aligned} \tag{3.70}$$

where $\varepsilon_0 = 1$ and $\varepsilon_n = 2$ for $n \geq 1$.

In Figure 3.1, the known analytic solution is compared with the solutions obtained via collocation and Galerkin. Clearly both methods agree extremely well.

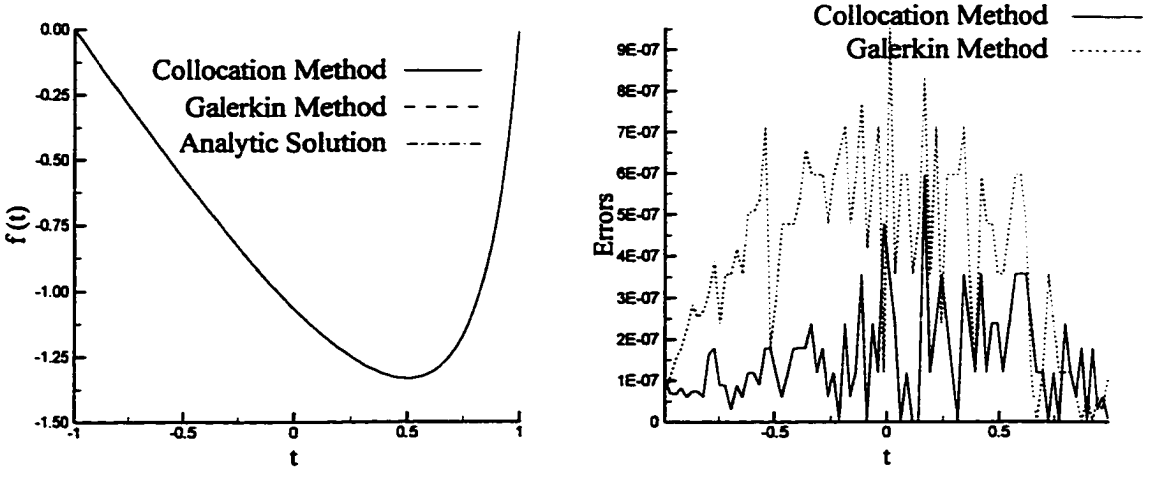

Figure 3.1 Collocation and Galerkin methods with 2 end-point subsidiary conditions compared with the analytic solution

Now, instead of two end-point type subsidiary conditions, we will impose one end-point and one integral type subsidiary condition. The problem is stated as follows:

$$\int_{-1}^{1} \frac{f(t)}{\sqrt{1-t^2}} \left\{ \frac{1}{(s-t)^2} + \ln|s-t| + 2(s-t)^2 \right\} dt = g(s) \quad \text{for} \quad |s| \leq 1$$

with subsidiary conditions

$$f(-1) = 0 \text{ and } \int_{-1}^{1} \frac{f(t)}{\sqrt{1-t^2}} dt = 0$$

and right hand side

$$g(s) = \frac{16\pi}{(5-4s)^2} + \pi \ln\left(\frac{5-4s}{8}\right) + \pi\left(\ln 2 + \frac{1}{4}\right)$$

The closed form solution for this example is given below

$$f(t)=\frac{3}{5-4t}-1-\frac{2t}{3}$$
$$=\sum_{n=0}^{\infty}\varepsilon_n 2^{-n}T_n(t)-T_0(t)-\frac{2}{3}T_1(t)$$

Below are the plot of the analytic solution compared to the numerical solutions obtained by the collocation and Galerkin methods. Again, the accuracy is exceptional.

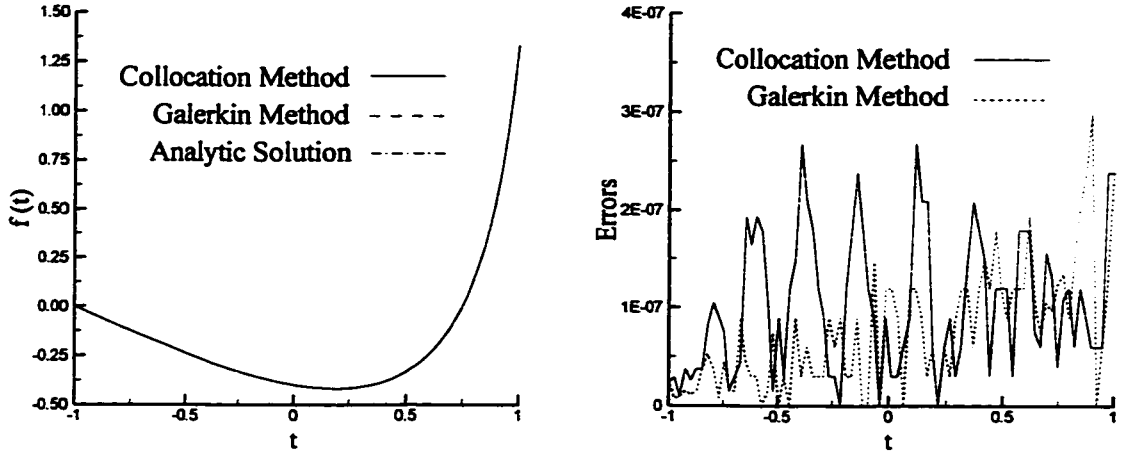

Figure 3.2 Collocation and Galerkin methods with 1 end-point and 1 integral subsidiary conditions compared with the analytic solution

Lastly, we will impose two integral type subsidiary conditions. Solve

$$\int_{-1}^{1}\frac{f(t)}{\sqrt{1-t^2}}\left\{\frac{1}{(s-t)^2}+\ln|s-t|+2(s-t)^2\right\}dt=g(s)\ \text{ for }\ |s|\le 1$$

with subsidiary conditions

$$\int_{-1}^{1}\frac{f(t)}{\sqrt{1-t^2}}dt=0\ \text{ and }\ \int_{-1}^{1}\frac{tf(t)}{\sqrt{1-t^2}}dt=0$$

and right hand side

$$g(s)=\frac{16\pi}{(5-4s)^2}+\pi\ln\left(\frac{5-4s}{8}\right)+\pi\left[\ln 2+\frac{1}{4}+s\right].$$

The closed form solution is

$$f(t)=\frac{3}{5-4t}-1-s$$
$$=\sum_{n=0}^{\infty}\varepsilon_n 2^{-n}T_n(t)-T_0(t)-T_1(t)$$

Again we see very good results. The errors are very small in all three test cases.

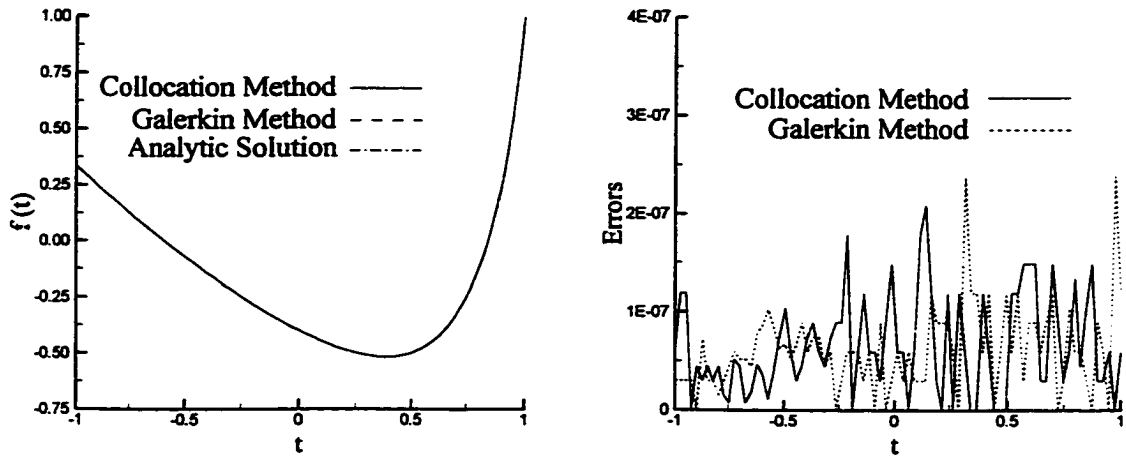

Figure 3.3 Collocation and Galerkin methods with 2 integral type subsidiary conditions compared with the analytic solution

To further test the method, an example with some relevance later is considered.

The integral equation to solve is

$$\int_{-1}^{1}\frac{f(t)}{\Delta(t)}\frac{kH_1^{(2)}(k|s-t|)}{|s-t|}dt=k\cos\alpha e^{iks\cos\alpha} \tag{3.71}$$

with subsidiary conditions

$$f(-1)=f(1)=0 \tag{3.72}$$

For small argument, $|s-t|<<1$, it is easily shown that

$$\frac{kH_1^{(2)}(k|s-t|)}{|s-t|} = \frac{2i}{\pi}\frac{1}{(s-t)^2} - \frac{ik^2}{\pi}\ln|s-t| - \frac{ik^2}{\pi}\left(\ln\frac{k}{2} + \gamma - \frac{1}{2} + \frac{i\pi}{2}\right) + O\left(|s-t|^2\right)$$

where $H_\nu^{(2)}(x)$ is the νth order Hankel function of the second kind and γ is Euler's constant.

Equation (3.71) can therefore, be rewritten as

$$\int_{-1}^{1} \frac{f(t)}{\Delta(t)}\left\{\frac{2i/\pi}{(s-t)^2} - \frac{ik^2}{\pi}\ln|s-t| + D(s,t)\right\}dt = k\cos\alpha e^{ik s\cos\alpha} \tag{3.73}$$

where

$$D(s-t) = \frac{kH_1^{(2)}(k|s-t|)}{|s-t|} - \frac{2i/\pi}{(s-t)^2} + \frac{ik^2}{\pi}\ln|s-t| \tag{3.74}$$

The first set of results we consider is the comparison between different choices of collocation points. Recall the two sets of collocation nodes used are given in equations (3.63) and (3.64). Figure 3.4 shows the error in the solutions between the two choices of collocation points.

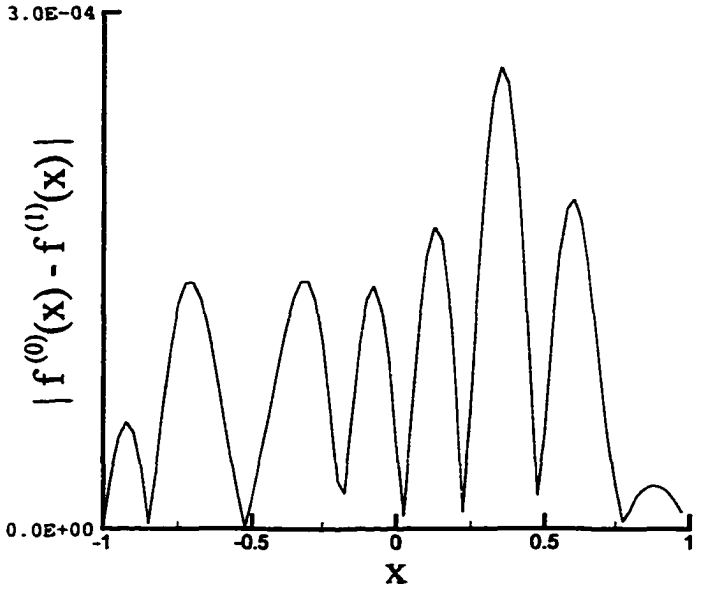

Figure 3.4 Comparison between choice of collocation nodes

The error caused by using different collocation nodes seems to be small. Therefore we will be using both sets of collocation nodes when comparing to the solution of the collocation method with the solution of the Galerkin method.

We clearly demonstrated the computational efficiency of the collocation method in the previous chapter. This chapter, therefore, will only focus on the convergence of the three methods.

In order to test the convergence of the collocation methods against the Galerkin method, we will obtain a solution to the integral equation, in each of the three cases, by taking $M = 2k$ terms in the eigenfunction expansion and then obtain another solution using $M = 2k + 20$. Table 3.1 shows the relative percentage error of the k^{th} term in each of the three cases for varying values of k. Collocation 1 and collocation 2 denote the use of the collocation nodes from equations (3.63) and (3.64), respectively.

Table 3.1
Relative percentage errors of the k^{th} solution component for two collocation methods and the Galerkin method by taking $2k$ and $2k$+20 terms in the solution

k	Collocation nodes eq. (3.63)	Collocation nodes eq. (3.64)	Galerkin method
10	0.65	0.83	1.01
12	0.57	0.71	0.87
14	0.74	0.97	1.19
16	0.69	0.90	1.11
18	0.66	0.85	1.04
20	0.80	1.06	1.31
22	0.70	0.92	1.12
24	0.73	0.96	1.17
26	0.81	1.08	1.33
28	0.70	0.92	1.12
30	0.78	1.03	1.26
32	0.79	1.06	1.29
34	0.70	0.92	1.12
36	0.80	1.07	1.31
38	0.75	1.01	1.24
40	0.72	0.94	1.15
42	0.81	1.08	1.32
44	0.72	0.96	1.18
46	0.74	0.97	1.19
48	0.79	1.06	1.30
50	0.70	0.93	1.13

Surprisingly, the collocation method using the collocation nodes given by equation (3.63) seems to have the fastest rate of convergence. This gives veracity to the claim that the collocation method is superior to the Galerkin method.

Next we consider several examples involving the same integral equation but with different subsidiary conditions. The problems to be considered are

$$\int_{-1}^{1} \frac{f(t)}{\Delta(t)} \frac{kH_1^{(2)}(k|s-t|)}{|s-t|} dt = k\cos\alpha e^{iks\cos\alpha} \tag{3.75}$$

with subsidiary conditions

1. $$\int_{-1}^{1} \frac{f(t)}{\Delta(t)} dt = 0 \text{ and } f(1) = 0 \tag{3.76}$$

2. $$f(-1) = 1 \text{ and } \int_{-1}^{1} \frac{tf(t)}{\Delta(t)} dt = 0 \tag{3.77}$$

3. $$\int_{-1}^{1} f(t) dt = 0 \text{ and } \int_{-1}^{1} \frac{tf(t)}{\Delta(t)} dt = 0 \tag{3.78}$$

4. $$f(-1) = -1 \text{ and } f(1) = 1 \tag{3.79}$$

The solutions $f(t)$ are plotted in Figure 3.5 for $k = 3\pi$, $\alpha = 0$. The figure in the upper left corresponds to subsidiary condition (3.76), upper right figure with (3.77), lower left with (3.78) and lower right with (3.79).

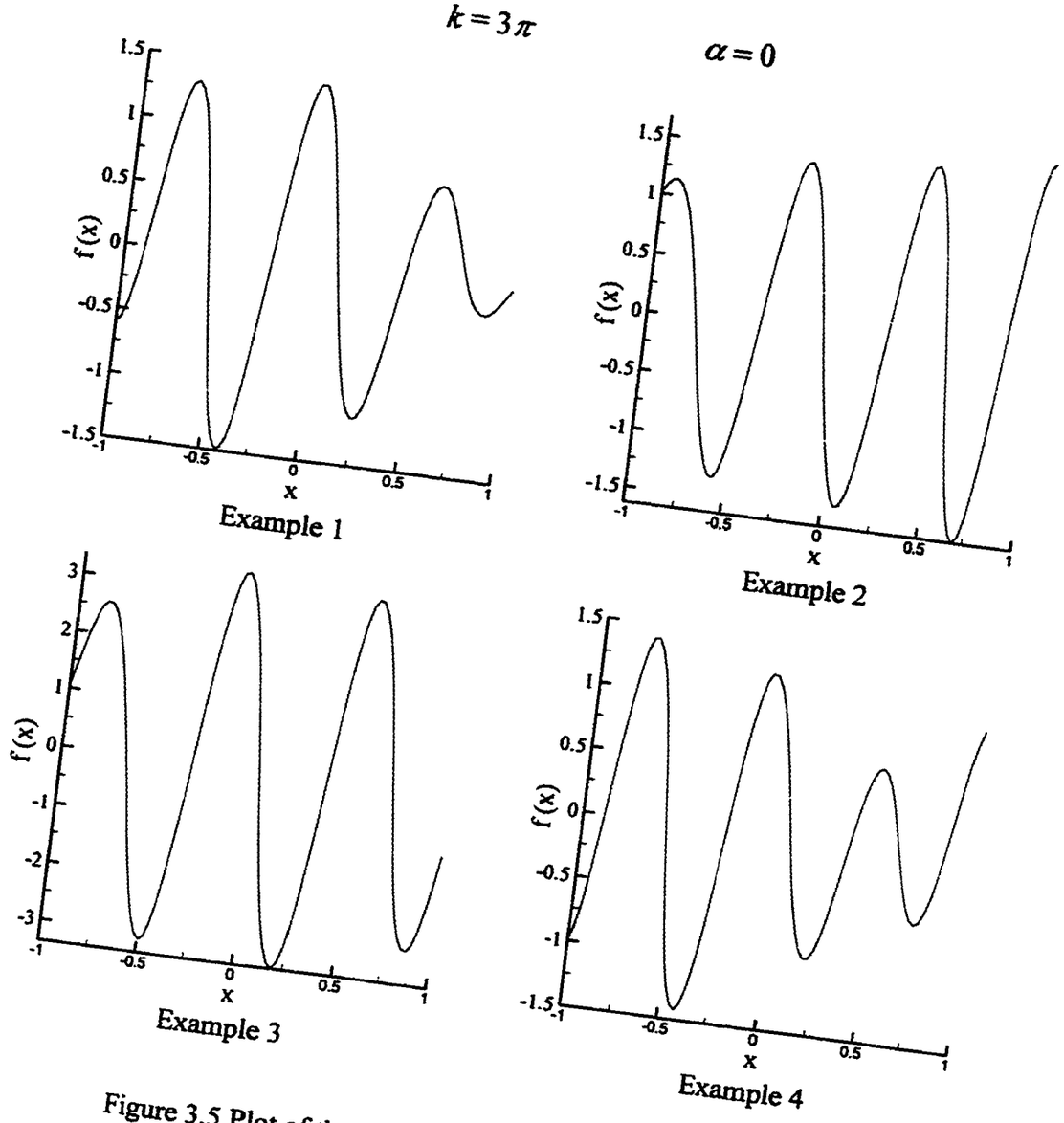

Figure 3.5 Plot of the solution for various subsidiary conditions

SECTION 4

DIFFRACTION OF AN OUT OF PLANE SHEAR WAVE BY A GRIFFITH CRACK

4.1 Introduction

The study of the Griffith crack originated from the observation that remote loading can cause very large stresses for an elliptic cutout located in an infinite, homogeneous medium. In fact, as the minor axis of an elliptic cutout approaches zero, the ellipse degenerates to a line crack and it can easily be shown that the stresses at the end of this line crack approach infinity and thus, any loading of the material will result in material failure.

By studying the energy changes caused by the extension of a line crack, Griffith [15] determined that a line crack is capable of undergoing a constant load without material failure. He concluded that two conditions are necessary for the extension of the crack. The stress ahead of the crack must be above some critical stress value and the total energy must be reduced by an incremental extension of the crack.

In work by Irwin [17] a relationship between the stresses at the tip of a line crack and the strain energy release rate was demonstrated. From this relationship he was able to show that for some critical stress value, the crack would propagate. The notation of a Stress Intensity Factor (SIF) is used to measure the stresses concentrated in a localized region. For the line crack we are interested in the region located at the end of a Griffith

crack and therefore by studying SIF we are able to determine the critical stress value required for crack propagation.

The problem discussed here is that of determining the SIF and the elastic field in an infinite solid containing a finite line crack or "Griffith crack" which diffracts an out of plane shear wave. Although Griffith did not consider a case involving dynamic loading, it has been an active area of research.

Dynamic crack problems are of particular interest for two reasons. Firstly, it has been observed that the dynamic Stress Intensity Factors may be about 30% higher than the corresponding static SIF [29]. Secondly, the dynamic fracture toughness value has been experimentally shown to be considerably lower than the static fracture toughness value [20]. In a paper by Loeber and Sih [24] the solution for the dynamic diffraction problem is given for a Griffith crack. The problem is also addressed by Mal [26]. The difference between the two is the frequency range over which the solutions are valid. Loeber and Sih solve the problem for low and intermediate frequencies whereas Mal solves the near field problem without restrictions on the frequency. Clearly, we would like to solve this problem for all frequencies and have a solution that is valid everywhere in the displacement field.

The goal of this chapter is to develop an efficient, numerical technique for solving the dynamic crack problem. Furthermore, we wish to relax the intermediate frequency restriction made by Loeber and Sih and construct a solution which is valid everywhere in the displacement field. In addition, the numerical technique we develop must be versatile enough to apply to a class of crack problems, not just the single Griffith crack problem.

Nonetheless, the first case to be studied is the single crack problem. In later chapters, the dynamic crack problem is solved for multiple cracks.

The method used to solve the dynamic Griffith crack problem is straight forward and it is easily adapted to other problems related to the diffraction of an out-of-plane shear wave by multiple but disjoint cracks. Once a boundary value problem is derived, it is converted to an equivalent system of hypersingular integral equation similar to the ones discussed in chapter 2. Upon solving the integral equations the total displacement field is known and from the displacement field, the SIF is computed. Numerical experiments are conducted and the results are then compared with results obtained by others, in particular Loeber and Sih, and Mal. We will see that the results agree very well and we were able to relax the low frequency restriction required by Loeber and Sih and we were able to obtain a solution valid in everywhere in the displacement field, not just the near-field.

4.2 Boundary Value Problem Derivation

A crack is located in an elastic, homogenous, isotropic medium. In the rectangular coordinate system (x,y,z), the crack is located in the region $a \le x \le b$, $y = h$ and $-\infty \le z \le \infty$. See Figure 4.1

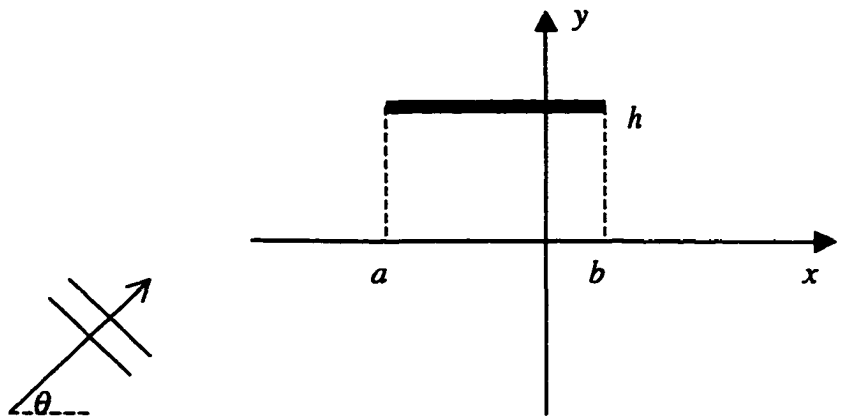

Figure 4.1 Geometry for Griffith crack

Under the assumptions of linear elasticity, the equation of motion is given by

$$\sigma_{ij,j} + F_i = \rho \ddot{u}_i \tag{4.1}$$

where σ_{ij} are the stresses, F_i are body forces per unit volume and ρ is mass per unit volume. In equation (4.1) the summation convention applies, so that

$$\sigma_{ij,j} = \frac{\partial \sigma_{i1}}{\partial x_1} + \frac{\partial \sigma_{i2}}{\partial x_2} + \frac{\partial \sigma_{i3}}{\partial x_3} \quad \text{for } i = 1,2,3. \tag{4.2}$$

and

$$\ddot{u}_i = \frac{\partial^2}{\partial t^2}(u_i) \tag{4.3}$$

Furthermore, the independent variables are defined by

$$x_1 = x,\ x_2 = y,\ x_3 = z$$

and the stress and displacement notation is defined as

$$\sigma_{ij} = \sigma_{x_i x_j} \text{ and } u_i = u_{x_i}.$$

So, from the assumption of out of plane shear, the only non-vanishing displacement lies in the $x_3 = z$ direction, $u_z = u_z(x,y,t)$ and the only non-vanishing components of stress are

$$\sigma_{xz} = \mu \frac{\partial u_z}{\partial x} \text{ and } \sigma_{yz} = \mu \frac{\partial u_z}{\partial y} \tag{4.4}$$

Hence, assuming no body forces, equation (4.1) reduces to

$$\frac{\partial^2 u_z}{\partial x^2} + \frac{\partial^2 u_z}{\partial y^2} = \frac{1}{c^2} \frac{\partial^2 u_z}{\partial t^2} \tag{4.5}$$

where $c^2 = \frac{\mu}{\rho}$ is the shear wave velocity, and μ is the shear modulus.

The displacement $u_z(x,y,t)$ is assumed to be time harmonic and hence, we may define a new dependant variable U by

$$u_z(x,y,t) = e^{-i\omega t} U(x,y). \tag{4.6}$$

Substituting (4.6) into the wave equation (4.5), yields the Helmholtz wave equation

$$\frac{\partial^2 U}{\partial x^2} + \frac{\partial^2 U}{\partial y^2} + k^2 U = 0 \tag{4.7}$$

where $k = \frac{\omega}{c}$.

The total displacement field is composed of an incident displacement and a scattered displacement that is due to the presence of the crack. The total displacement is thus,

$$U(x,y) = U^i(x,y) + U^s(x,y) \tag{4.8}$$

where U^i represents a known incident displacement and U^s denotes the scattered displacement. The known incident displacement is assumed to be continuous across the

crack and satisfies (4.7) everywhere in the field. Hence, the scattered displacement must satisfy,

$$\frac{\partial^2 U^s}{\partial x^2}+\frac{\partial^2 U^s}{\partial y^2}+k^2 U^s=0 \tag{4.9}$$

Since the crack is traction free, the total field must satisfy the boundary condition,

$$\sigma_{yz}(x,h)=0 \text{ for } a<x<b \tag{4.10}$$

In terms of the displacements, this boundary condition becomes

$$\frac{\partial U}{\partial y}(x,h)=0 \text{ for } a<x<b \tag{4.11}$$

In addition, energy considerations require that the crack opening displacement be bounded and lastly, since the scattered waves originate at the crack site, they must satisfy an outgoing radiation wave condition at infinity.

To finalize the boundary value problem derivation, a summary of the governing equations for the scattered displacement in terms of a known incident displacement will be given.

$$\frac{\partial^2 U^s}{\partial x^2}+\frac{\partial^2 U^s}{\partial y^2}+k^2 U^s=0 \tag{4.12}$$

$$\frac{\partial U^s}{\partial y}(x,h)=-\frac{\partial U^i}{\partial y}(x,h) \text{ for } a<x<b \tag{4.13}$$

$$\lim_{r\to\infty}\sqrt{r}\left(\frac{\partial U^s}{\partial r}-ikU^s\right)=0 \text{ for } r=\sqrt{x^2+y^2} \tag{4.14}$$

$$\lim_{x\to a^+}\Delta U(x,h)=\lim_{x\to b^-}\Delta U(x,h)=0 \tag{4.15}$$

where

$$\Delta U(x,h) = \lim_{y \to h^+} U(x,y) - \lim_{y \to h^-} U(x,y) \tag{4.16}$$

4.3 Integral Equation Derivation

The Green's function for the two-dimensional Helmholtz operator that implicitly satisfies the radiation condition is given by

$$G(x-X, y-Y) = \frac{i}{4} H_0^{(1)}(kr) \tag{4.17}$$

where

$$r = \sqrt{(x-X)^2 + (y-Y)^2} \tag{4.18}$$

For an arbitrary field function f, define the following field operators.

$$\mathbf{d}[f](x,y) = \int_a^b f(X) d(x-X, y) dX \tag{4.19}$$

$$\mathbf{d}_y[f](x,y) = \int_a^b f(X) d_y(x-X, y) dX \tag{4.20}$$

where,

$$\begin{aligned} d(x-X,y) &= \frac{\partial G}{\partial Y}(x-X, y-h) \\ &= \frac{ik}{4} \frac{H_1^{(1)}(kr_h)}{r_h} \end{aligned} \tag{4.21}$$

$$\begin{aligned} d_y(x-X,y) &= \frac{\partial^2 G}{\partial y \partial Y}(x-X, y-h) \\ &= \frac{ik}{4} \frac{H_1^{(1)}(kr_h)}{r_h} - \frac{ik}{4} \frac{(y-h_h)^2}{r_h^3} \left[2H_1^{(1)}(kr_h) - kr_h H_0^{(1)}(kr_h) \right] \end{aligned} \tag{4.22}$$

and

$$r_h = \sqrt{(x-X)^2 + (y-h)^2}$$

Using results from potential theory [12], the scattered field can be written in terms of a double layer potential, with unknown double layer density Q.

$$U^s(x,y) = \mathbf{d}[Q](x,y) \tag{4.23}$$

Therefore, the total displacement takes the form

$$U(x,y) = \mathbf{d}[Q](x,y) + U^i(x,y) \tag{4.24}$$

In anticipation of evaluating the field operator on the crack, we will introduce the following surface operators. For an arbitrary field function f,

$$\mathbf{D}_y[f](x) = \mathbf{d}_y[f](x,h) = \int_a^b f(X) D_y(x-X)dX \tag{4.25}$$

where

$$D_y(x-X) = \lim_{y\to h} \frac{\partial^2 G}{\partial y \partial Y} = \frac{ik}{4} \frac{H_1^{(1)}(k|x-X|)}{|x-X|} \quad \text{for } a < x < b \tag{4.26}$$

Hence, applying boundary condition (4.13) to (4.23) yields the hypersingular integral equation for the unknown layer density Q

$$\mathbf{D}_y[Q](x) = -\frac{\partial U^i}{\partial y}(x,h) \text{ for } a < x < b \tag{4.27}$$

Asymptotic analysis about the edges of the crack shows that the layer density must have the form

$$Q(X) = \sqrt{(b-X)(X-a)}\ F(X) \quad \text{for } a < X < b \tag{4.28}$$

A brief summary of the system of hypersingular integral equation is now given. The unknown double layer density $Q(X)$ is uniquely determined by the following set of equations.

$$\mathbf{D}_y[Q](x) = -\frac{\partial U^i}{\partial y}(x,h) \text{ for } a < x < b \tag{4.29}$$

$$Q(X) = \sqrt{(b-X)(X-a)}\ F(X) \text{ for } a < X < b \tag{4.30}$$

4.4 Singular Kernel Analysis

The kernel is composed of a Hadamard term, a logarithmic term, and a bounded term.

$$\begin{aligned} D_y(x-X) &= \frac{ik}{4}\frac{H_1^{(1)}(k|x-X|)}{|x-X|} \\ &= \frac{1}{2\pi}\frac{1}{(x-X)^2} - \frac{k^2}{4\pi}\ln|x-X| + K_{reg}(x,X) \end{aligned} \tag{4.31}$$

where

$$K_{reg}(x,X) = \frac{ik}{4}\frac{H_1^{(1)}(k|x-X|)}{|x-X|} - \frac{1}{2\pi}\frac{1}{(x-X)^2} + \frac{k^2}{4\pi}\ln|x-X| \tag{4.32}$$

Furthermore, it can be easily shown that $K_{reg}(x,X) = O(1)$. This integral equation is solvable with the method outlined in chapter 2.

To complete this section, an overview of the integral equation is now given. We wish to solve

$$\int_a^b \Delta(X)F(X)\left\{\frac{1/2\pi}{(x-X)^2} - \frac{k^2}{4\pi}\ln|x-X| + K_{reg}(x,X)\right\}dX = -\frac{\partial U^i}{\partial y}(x,h) \tag{4.33}$$

for $a \le x \le b$, where $\Delta(X) = \sqrt{(b-X)(X-a)}$ and K_{reg} is given in equation (4.32). Equation (4.33) is solvable via the method outlined in chapter 2 by making a transformation from the interval $[a,b]$ to the interval $[-1,1]$.

4.5 Results

The stress intensity factors at the crack tips are defined by:

$$K_3(a) = \lim_{x \to a^+} \frac{\mu}{2} \frac{\Delta U(x,h)}{\sqrt{2(x-a)}} \quad \text{and} \quad K_3(b) = \lim_{x \to b^-} \frac{\mu}{2} \frac{\Delta U(x,h)}{\sqrt{2(b-x)}}$$

or equivalently,

$$K_3(a) = \frac{\mu w_0}{2} \sqrt{\frac{b-a}{2}}\, F(a) \quad \text{and} \quad K_3(b) = \frac{\mu w_0}{2} \sqrt{\frac{b-a}{2}}\, F(b). \tag{4.34}$$

In order to compare these results with those from Loeber and Sih [24], we will assume the incident displacement is given by a horizontally polarized shear wave (SH wave) with frequency k and let this wave impinge at an angle of θ with the x - axis.

$$U^i(x,y) = w_0 e^{-ik(x\cos\theta + y\sin\theta)} \tag{4.35}$$

Furthermore, define the following reference quantities

Semi-crack length: $L = \dfrac{b-a}{2}$

Reference stress: $\tau_0 = k\mu w_0 \sin\theta$

Reference stress intensity: $K_{ref} = \tau_0 \sqrt{L}$

Reference displacement: $U_{ref} = \dfrac{\tau_0 L}{\mu}$

Figure 4.2 shows the intensity factor vs. normalized wave number. It should be noted that $k = 0$ is the corresponding static case. Hence, the claim that the dynamic crack problem produces SIF about 30% higher than the corresponding static ones is demonstrated. In particular, for $\theta = 90^o$, the maximum SIF occurs at $kL = 0.95$.

Secondly, Figure 4.3 shows the SIF plotted against the angle of incidence. Interestingly, the maximum SIF occurs at an angle of 110 °.

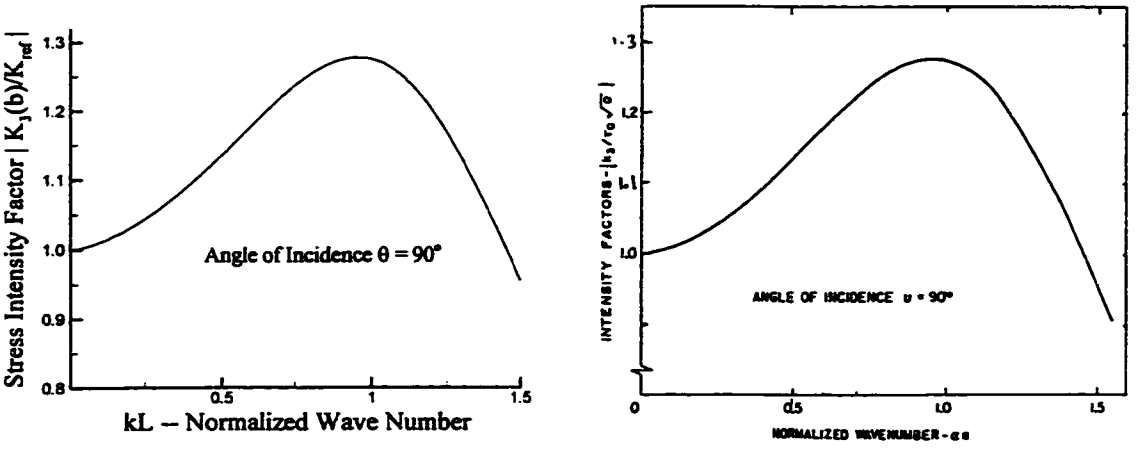

Figure 4.2 SIF v. Normalized wave number (comparison with Loeber and Sih)

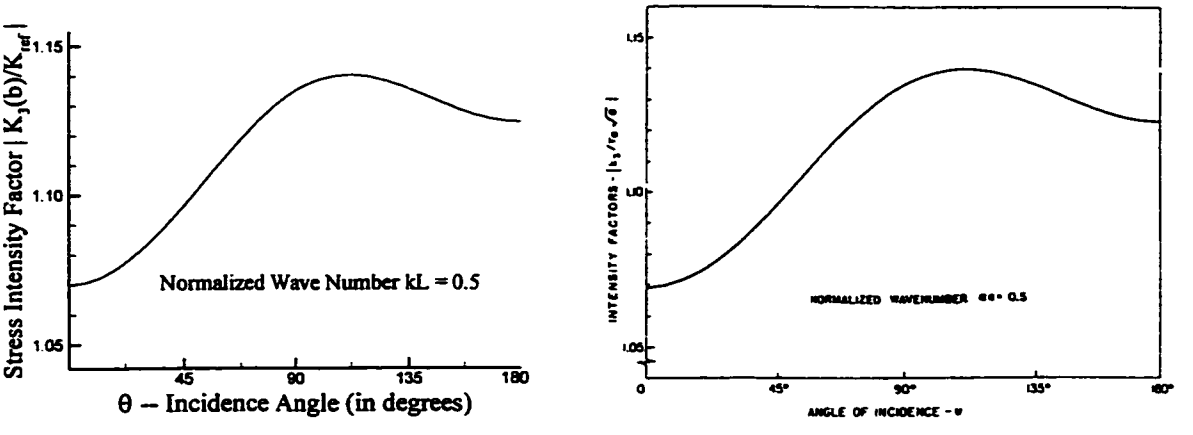

Figure 4.3 SIF v. Angle of incidence (comparison with Loeber and Sih)

Lastly, Figure 4.4 demonstrates that with an angle of 110° and $kL = 1.0$, the dynamic crack problem produces a SIF approximately 35% higher than the static case.

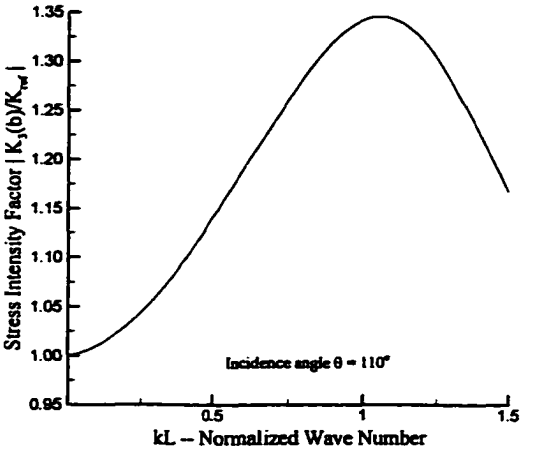

Figure 4.4 SIF v. kL with 110 degrees incidenct angle

In all three figures, the graph on the right was taken directly from Loeber and Sih [24]. The results above agree with those from Loeber and Sih. Now we will focus on comparing our results with those from Mal. In particular, the result from Mal that is not given by Loeber and Sih is a plot of the SIF for higher frequencies. Using the same parameters as above we will plot the SIF for a normalized frequency range of 0 to 8.

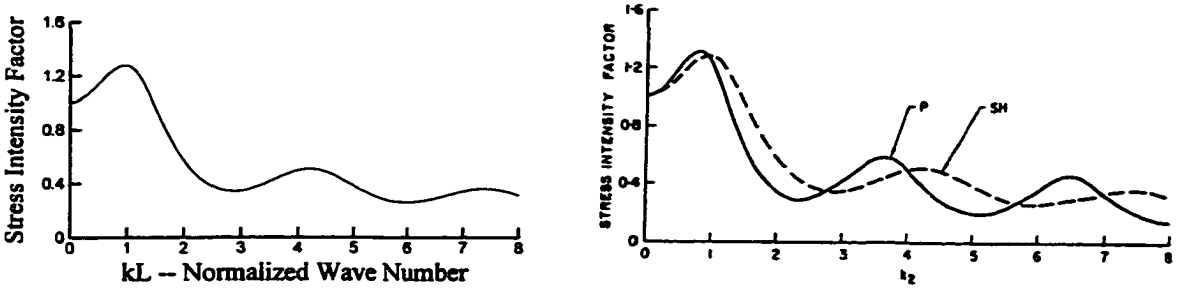

Figure 4.5 SIF for higher frequencies

The graph on the right was taken directly from the paper by Mal [26], so it is clear that these results are in agreement with those from Mal.

Now we will consider the crack opening displacement plots. In Figure 4.6 the crack opening displacements are plotted from the method derived here. The right part of Figure 4.7 is the graph given by Loeber and Sih whereas the left side is the plot from Mal. Seemingly, Loeber and Sih, and Mal have yielded the same results for the crack opening displacement. However, it appears as though Loeber and Sih have an error in the case corresponding to $kL = 1.5$. All other results from both papers agree with the results derived here.

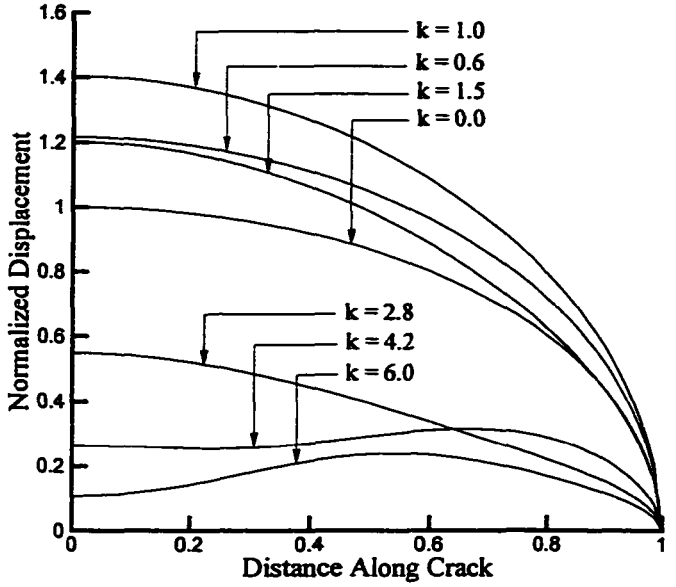

Figure 4.6 Normalized magnitude of the crack opening displacement

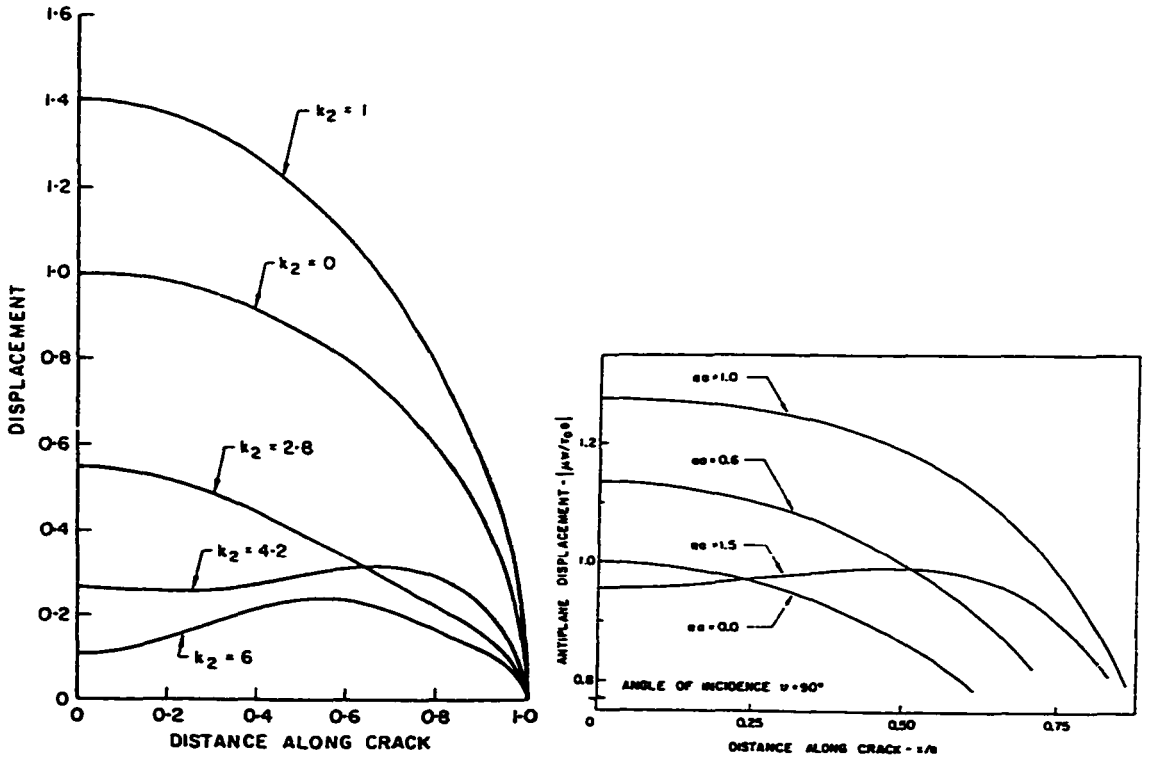

Figure 4.7 Graphs from Mal and Loeber and Sih

4.6 Conclusions

The observations made by Loeber and Sih, as well as Mal, have been substantiated here. Moreover, the low to intermediate frequency restriction has been lifted, allowing for the solutions to a wider range of problems. Furthermore, since we made no simplifying assumptions about the solution, our solution is valid everywhere in the displacement field, not just in the near field.

In this chapter we developed an efficient, accurate numerical procedure for solving a dynamic crack problem. This method is versatile enough to apply to other dynamic crack problems, as will be shown in later chapters where it is applied to problems involving a pair of parallel cracks and a pair of perpendicular cracks. In fact, this numerical procedure is sufficiently versatile to apply to an array of disjoint parallel and perpendicular cracks without increasing the numerical complexity.

SECTION 5

DIFFRACTION OF AN OUT OF PLANE SHEAR WAVE BY TWO PARALLEL GRIFFITH CRACKS

5.1 Introduction

In the previous chapter we demonstrated that for a Griffith crack a dynamic incident displacement could produce stress intensity factors (SIF) as much as 35% higher than the corresponding static Griffith crack problem. Another factor that may effect SIF is the introduction of a second Griffith crack. This chapter focuses on the interaction of a second parallel Griffith crack and the corresponding SIF related to this interaction.

In a paper by, Jain and Kanwal [19], the solution for the diffraction of a dynamic incident displacement is given for two symmetric, coplanar cracks. Their solution method is based on expanding the wave number, which is assumed to be small, in a power series. Clearly, for large wave numbers their method becomes invalid. Itou [18] was able to solve the coplanar Griffith crack problem for intermediate wave numbers but his method is only valid in the near field. Furthermore, he assumes the cracks are symmetric and coplanar. Our goal here is to expand on this work by solving the problem for any wave number and any two parallel, disjoint cracks.

In a manner similar to that used in the previous chapter we will derive the governing Neumann boundary value problem, convert it to a system of hypersingular integral equations and solve the system of integral equations via collocation. Upon solving for the total displacement field, the SIF is computed using several different crack

configurations. In particular, comparisons are made between the solution given by Itou [18] and the solutions given by the method derived here as well as some examples not solvable by Itou.

5.2 Governing Equations Derivation

Two cracks are located in an elastic, homogenous, isotropic medium. In the rectangular coordinate system (x, y, z), the cracks are located in the regions $a_1 \le x \le b_1$, $y = h_1$ and $a_2 \le x \le b_2$, $y = h_2$ and $-\infty \le z \le \infty$. See Figure 5.1.

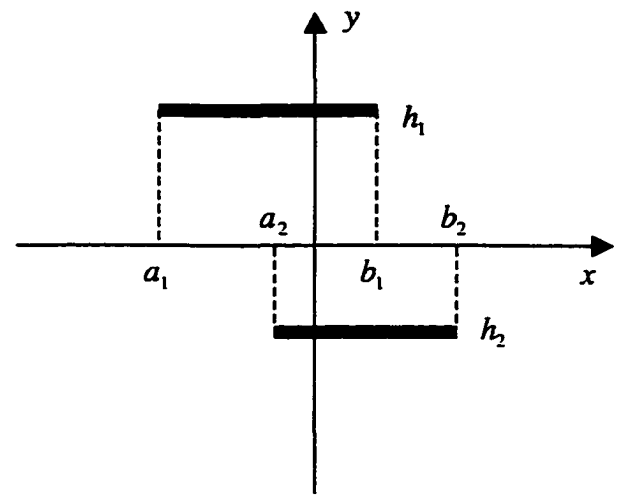

Figure 5.1: Geometry for parallel cracks

Note that the two cracks can be coplanar as long as they remain completely disjoint. That is, if $h_1 = h_2 = h$, then $b_1 < a_2$.

Due to out-of-plane shear and temporal frequency ω, the total displacement in the z – direction satisfies the Helmholtz wave equation,

$$\frac{\partial^2 U}{\partial x^2} + \frac{\partial^2 U}{\partial y^2} + k^2 U = 0 \tag{5.1}$$

where $k = \frac{\omega}{c}$, $c^2 = \frac{\mu}{\rho}$ is the shear wave velocity, μ is the shear modulus, and ρ is the density.

The total displacement field is composed of a scattered displacement due to each crack and an incident displacement. Thus, the total displacement is,

$$U(x,y) = U^i(x,y) + \sum_{j=1}^{2} U_j^s(x,y) \tag{5.2}$$

where U^i represents a known incident displacement and U_j^s denote the displacement due to the j^{th} crack (scattered displacement). The known incident displacement is assumed to be continuous across both cracks and satisfies (5.1) everywhere in the displacement field. Hence, the scattered displacements must satisfy,

$$\frac{\partial^2 U_j^s}{\partial x^2} + \frac{\partial^2 U_j^s}{\partial y^2} + k^2 U_j^s = 0 \text{ for } j = 1,2 \tag{5.3}$$

The main difference between the single crack and parallel cracks exists in the boundary conditions. Since both cracks are traction free, the total displacement field must satisfy the boundary conditions, for $j = 1, 2$

$$\sigma_{yz}(x, h_j) = 0 \text{ for } a_j < x < b_j \tag{5.4}$$

In addition, it will be necessary to impose the outgoing radiation condition at infinity and to assume that the crack opening displacements are bounded.

In summary, the boundary value problem to be solved is given by

$$\frac{\partial^2 U_j^s}{\partial x^2} + \frac{\partial^2 U_j^s}{\partial y^2} + k^2 U_j^s = 0 \tag{5.5}$$

$$\frac{\partial U_j^s}{\partial y}(x,h_j) = -\frac{\partial U^i}{\partial y}(x,h_j) \text{ for } a_j < x < b_j \tag{5.6}$$

$$\lim_{r\to\infty}\sqrt{r}\left(\frac{\partial U_j^s}{\partial r} - ikU_j^s\right) = 0 \text{ where } r = \sqrt{x^2+y^2} \tag{5.7}$$

$$\lim_{x\to a_j^+}\Delta U(x,h_j) = \lim_{x\to b_j^-}\Delta U(x,h_j) = 0 \tag{5.8}$$

$$\Delta U(x,h_j) = \lim_{y\to h_j^+} U(x,y) - \lim_{y\to h_j^-} U(x,y) \tag{5.9}$$

for $j = 1, 2$.

The Green's function for the two-dimensional Helmholtz operator that implicitly satisfies the radiation conditions is the same one used in chapter 4, namely

$$G(x-X,y-Y) = \frac{i}{4}H_0^{(1)}(kr) \tag{5.10}$$

where

$$r = \sqrt{(x-X)^2+(y-Y)^2} \tag{5.11}$$

Now we will introduce the field and surface operators. For an arbitrary field function f and for $j = 1, 2$, define the following field operators.

$$\mathbf{d}^j[f](x,y) = \int_{a_j}^{b_j} f(X)d^j(x-X,y)dX \tag{5.12}$$

$$\mathbf{d}_y^j[f](x,y) = \int_{a_j}^{b_j} f(X)d_y^j(x-X,y)dX \tag{5.13}$$

where,

$$\begin{aligned} d^j(x-X,y) &= \frac{\partial G}{\partial Y}(x-X,y-h_j) \\ &= \frac{ik}{4}(y-h_j)\frac{H_1^{(1)}(kr_j)}{r_j} \end{aligned} \tag{5.14}$$

and

$$d_y^j(x-X,y)=\frac{\partial^2}{\partial y\partial Y}G(x-X,y-h_j)$$
$$=\frac{ik}{4}\frac{H_1^{(1)}(kr_j)}{r_j}-\frac{ik}{4}\frac{(x-h_j)^2}{r_j^3}\left[2H_1^{(1)}(kr_j)-kr_jH_0^{(1)}(kr_j)\right] \tag{5.15}$$

where

$$r_j=\sqrt{(x-X)^2+(y-h_j)} \quad \text{for } j=1,2 \tag{5.16}$$

Using results from potential theory [30], the scattered field can be written in the form

$$U_1^s(x,y)+U_2^s(x,y)=\mathbf{d}^1[Q_1](x,y)+\mathbf{d}^2[Q_2](x,y) \tag{5.17}$$

where Q_1 and Q_2 are the double layer densities of the upper and lower cracks, respectively. Therefore the total displacement takes the form

$$U(x,y)=U^i(x,y)+\mathbf{d}^1[Q_1](x,y)+\mathbf{d}^2[Q_2](x,y) \tag{5.18}$$

Define the following surface operators. For an arbitrary field function f and for $j=1,2$

$$\mathbf{D}_y^j[f](x)=\mathbf{d}_y^j[f](x,h_j)=\int_{a_j}^{b_j}f(X)D_y(x-X)dX \tag{5.19}$$

where

$$D_y^j(x-X)=\lim_{y\to h_j}\frac{\partial^2 G}{\partial y\partial Y}=\frac{ik}{4}\frac{H_1^{(1)}(k|x-X|)}{|x-X|} \quad \text{for } a_j<x<b_j \tag{5.20}$$

Hence, applying boundary conditions (5.6) to equation (5.17) yields the set of integral equations

$$\mathbf{D}_y^1[Q_1](x)+\mathbf{d}_y^2[Q_2](x,h_1)=-\frac{\partial U^i}{\partial y}(x,h_1) \text{ for } a_1<x<b_1 \tag{5.21}$$

and

$$\mathbf{d}_y^1[Q_1](x,h_2)+\mathbf{D}_y^2[Q_2](x)=-\frac{\partial U^i}{\partial y}(x,h_2) \text{ for } a_2 < x < b_2 \tag{5.22}$$

Equations (5.21) and (5.22) form a system of hypersingular integral equations for the unknown layer densities Q_1 and Q_2. Since the operators $\mathbf{d}_y^2[\phi](x,h_1)$ and $\mathbf{d}_y^1[\phi](x,h_2)$ are continuous, bounded linear operators, the asymptotic analysis about the edges of the cracks yields results similar to those for the single crack problem namely,

$$Q_j(X)=\sqrt{(b_j-X)(X-a_j)}\ F_j(X) \text{ for } a_j < X < b_j \text{ and } j=1,2 \tag{5.23}$$

A brief summary of the system of hypersingular integral equations is now given. The unknown layer densities $Q_1(X)$ and $Q_2(X)$ are uniquely determined by the following set of equations.

$$\mathbf{D}_y^1[Q_1](x)+\mathbf{d}_y^2[Q_2](x,h_1)=-\frac{\partial U^i}{\partial y}(x,h_1) \text{ for } a_1 < x < b_1 \tag{5.24}$$

$$\mathbf{d}_y^1[Q_1](x,h_2)+\mathbf{D}_y^2[Q_2](x)=-\frac{\partial U^i}{\partial y}(x,h_2) \text{ for } a_2 < x < b_2 \tag{5.25}$$

$$Q_j(X)=\sqrt{(b_j-X)(X-a_j)}\ F_j(X) \text{ for } a_j < X < b_j \text{ and } j=1,2 \tag{5.26}$$

It is clear that the equations (5.24) - (5.26) are no more difficult to solve than the single Griffith crack problem. The numerical procedure is the same except for the additional bounded kernel. Thus, the unknown densities are expanded as follows

$$Q_j(X)=\sqrt{(b_j-X)(X-a_j)}\sum_{n=0}^{M} f_n^j u_n^j(X) \text{ for } a_j \le X \le b_j \text{ and } j=1,2 \tag{5.27}$$

where $u_n^j(X)$ denote the shifted Tchebyshev polynomials of the second kind. The coefficients f_n^j are determined by using a collocation method.

5.3 Results

As in the single crack case, the numerical results are focused on finding the stress intensity factors at the crack tips. By analogy with the single crack case, for $j = 1,2$, the stress intensity factors are given by

$$K_j(a) = \frac{\mu w_0}{2}\sqrt{L_j}\, F_j(a) \tag{5.28}$$

and

$$K_j(b) = \frac{\mu w_0}{2}\sqrt{L_j}\, F_j(b) \tag{5.29}$$

where $L_j = \frac{b_j - a_j}{2}$.

Results are given in this section for the case of horizontally polarized incident waves (SH waves).

$$U^i(x,y) = w_0 e^{-ik(x\cos\theta + y\sin\theta)}$$

Furthermore, the following reference quantities are defined. For $j = 1, 2$

Semi-crack length: $L_j = \frac{b_j - a_j}{2}$

Stress: $\tau_0 = k\mu w_0 \sin\theta$

Stress intensity: $K_{j_{ref}} = \tau_0\sqrt{L_j}$

Displacement: $U_{ref}(x,y) = \frac{\tau_0 L_j}{\mu}$ for $a_j \le x \le b_j$ and $y = h_j$

Our first comparison is with the results of Itou [18]. Therefore, we use symmetric, coplanar cracks. Hence, let $h_1 = h_2 = 0$ and on the $x-$axis the cracks are located from $-b$ to $-a$ and a to b, respectively; see Figure 5.2

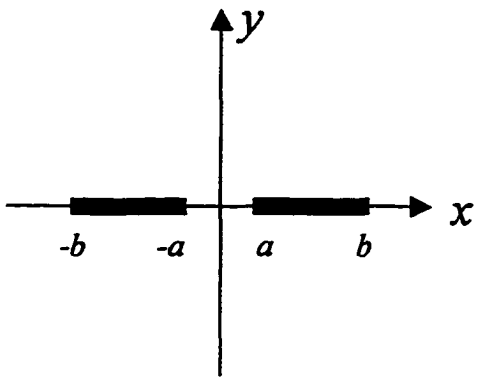

Figure 5.2 Geometry for coplanar symmetric cracks

In addition, we will assume the out of plane shear wave impinges the cracks at a right angle, $\theta = 90°$.

In Figure 5.3 and Figure 5.4, the stress intensity factors K_j are plotted for a/b = 0.1, 0.2, 0.5, 0.9, corresponding to the relative distances between the two coplanar cracks. In particular, the case for a/b = 0.9 approximates the single crack case. Figure 5.3 shows the SIF at the inner edge of the crack whereas Figure 5.4 shows the SIF of the outer edge of the crack. In both figures, the graphs on the right were taken directly from the paper by Itou [18].

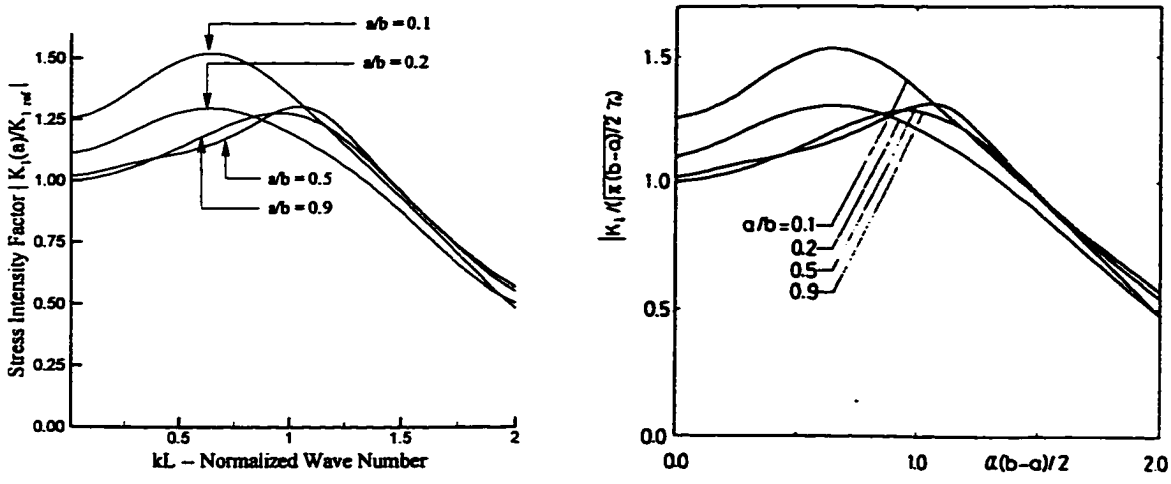

Figure 5.3 Stress Intensity Factors of the inner edges of symmetric, coplanar cracks (comparisons with Itou)

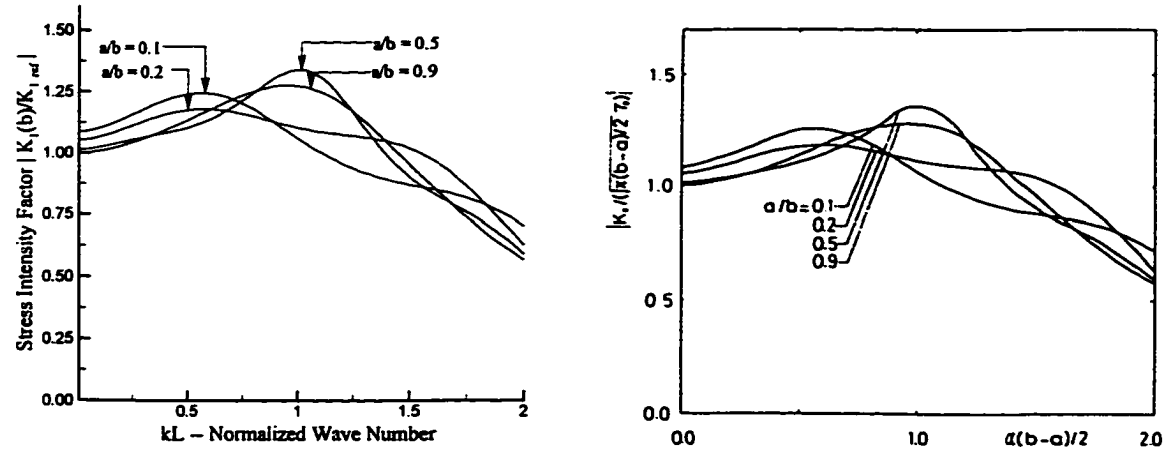

Figure 5.4 Stress Intensity Factors of the outer edges of symmetric, coplanar cracks (comparisons with Itou)

The case, $a/b = 0.9$, approximates the single crack and the results agree very well with that case. Moreover, the results derived here agree extremely well with those from Itou.

The stress intensity factors for $a/b = 0.1$, at the inner edge yields the largest magnitude. This leads to the question, what if the strips are not coplanar? The next set of

results is concerned with SIF of the inner edges of symmetric, non-coplanar cracks. The two cracks will be offset in the y direction by the values $\varepsilon = 0.05, 0.10, 0.15$, and 0.20 and axially located between $-1 \le x \le 0$ and $0 \le x \le 1$, see Figure 5.5

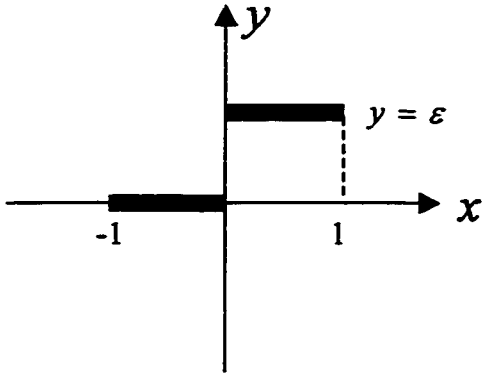

Figure 5.5 Geometry for offset cracks

The results are intuitively clear. Figure 5.6 gives the SIF of the inner edge of the top crack and Figure 5.7 gives the SIF for the inner edge of the lower crack. As the distance between the two cracks approaches zero the SIF of both inner edges increases. However, the increase in not a linear increase. Nonetheless, the shapes of the SIF for both the inner and outer edges are similar. However, for kL between 1 and 2, the SIF of the lower crack is larger than the upper crack. This observation lead to the staggered parallel crack problem.

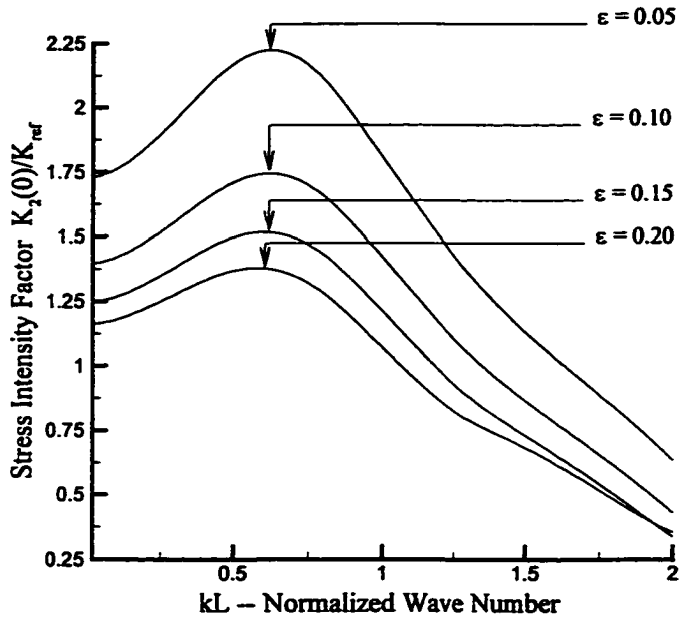

Figure 5.6 Stress Intensity Factors of offset cracks (top crack)

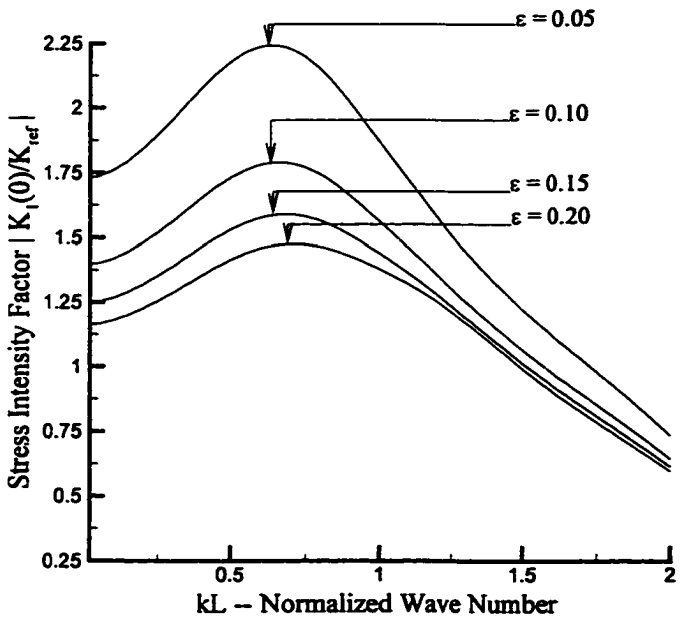

Figure 5.7 Stress Intensity Factors of offset cracks (lower crack)

The staggered crack problem focuses on two parallel, disjoint cracks that are a distance $h = 0.1,\ 0.2,\ 0.3,$ and 0.4 apart but the inner edge of one crack is positioned above the other crack. In particular, let the lower crack be located at $-1.5 \le x \le 1.5$ and the upper crack at $0 \le x \le 3$. See Figure 5.8

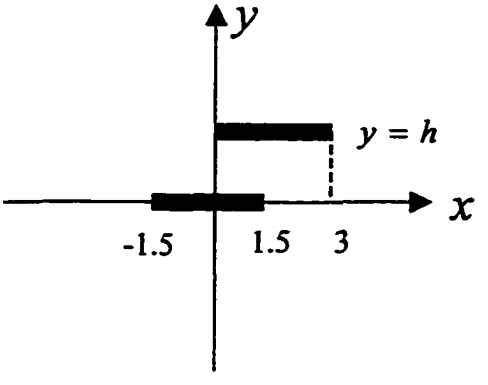

Figure 5.8 Geometry for staggered cracks

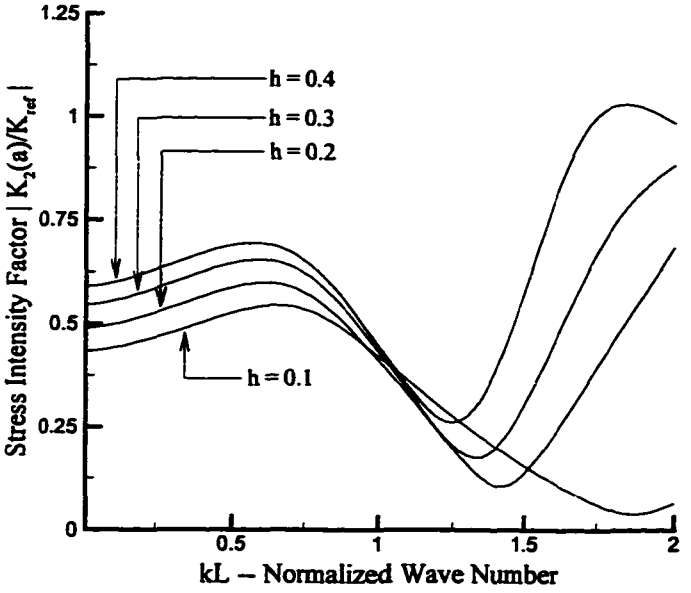

Figure 5.9 Stress Intensity Factor for staggered cracks (top crack)

This is particularly interesting. As h get smaller and kL < 1, the SIF of the top crack is reduced. It appears as though the lower crack is shielding the edge of the top crack. The next figure shows the SIF of the lower crack.

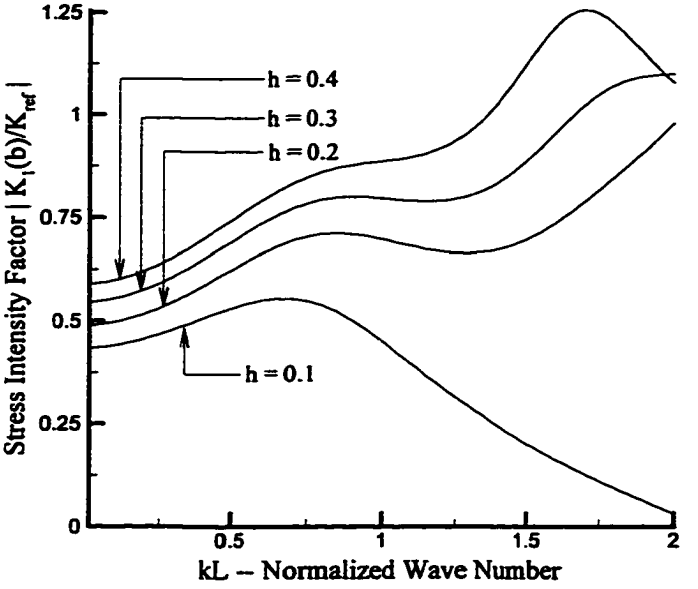

Figure 5.10 Stress Intensity Factor for staggered cracks (lower crack)

Figure 5.10 demonstrates the same type of behavior as Figure 5.9. A more in-depth study is a topic for further research.

Lastly, we will consider non-symmetric, coplanar cracks. We will hold one crack length fixed, say, $l_1 = 1$ and allow the other length to take the values, $l_2 = \alpha l_1$, where $\alpha = 2.00,\ 1.00,\ 0.50,$ and 0.25. See Figure 5.11

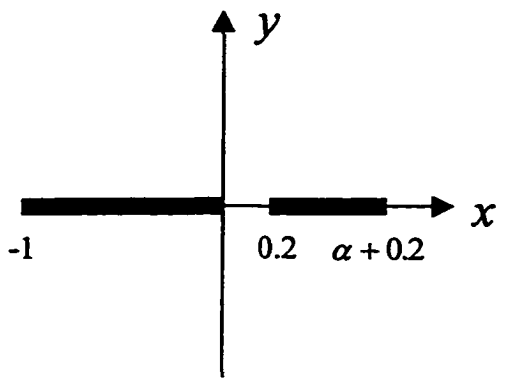

Figure 5.11 Geometry for non-symmetric cracks

It is important to note that the distance between the two cracks will remain fixed. Hence, the effect of the length of the second crack on the SIF of the first crack is examined.

Figure 5.12

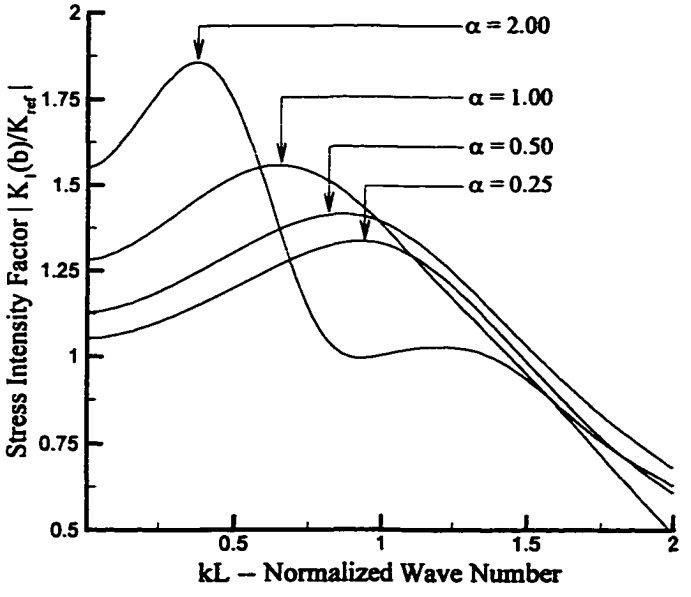

Figure 5.12 Stress Intensity Factor for non-symmetric cracks

Of particular interest are the cases $\alpha = 2$ and $\alpha = 0.5$, corresponding to crack 2 being twice and long and half as long as crack 1, respectively. From Figure 5.12, it is clear that the larger crack has a much greater effect on the SIF than the smaller crack. In fact, it is considerably higher for smaller wave numbers but considerably lower for larger wave numbers. This area of research will be left for future papers.

5.4 Conclusions

In this chapter we not only were able to reproduce results from others, we were able to expand on their research. Due to the flexibility of the crack length and locations, we were able to gain new insight into seeing what effect a second parallel Griffith crack has on the SIF.

In the next section the method is adapted to deal with the case of perpendicular Griffith cracks. We will conduct numerical studies similar to the ones conduct in this chapter.

SECTION 6

DIFFRACTION OF AN OUT OF PLANE SHEAR WAVE BY TWO PERPENDICULAR GRIFFITH CRACKS

6.1 Introduction

Section 5 demonstrated that the stress intensity factor of a Griffith crack is greatly effected by the interaction of a second, parallel Griffith crack. This observation led us to study what effect a second perpendicular Griffith crack has on the SIF. To the knowledge of the author, very little research exists for this problem. Therefore, we expect to gain new insight to this perpendicular Griffith crack problem.

The same methodology is used to derive the boundary value problem, convert it to an equivalent system of hypersingular integral equations and solve the system. Numerical studies similar to the studies from the parallel crack problem are performed.

6.2 Governing Equations Derivation

Find the stress intensity factors for a pair of perpendicular Griffith cracks. The two disjoint cracks are located in a homogeneous, isotropic, elastic material and must have no points in common. They occupy the regions of space $a_1 \le x \le b_1$, $y = h_1$, $|z| < \infty$ and $a_2 \le y \le b_2$, $x = h_2$, $|z| < \infty$. See Figure 6.1

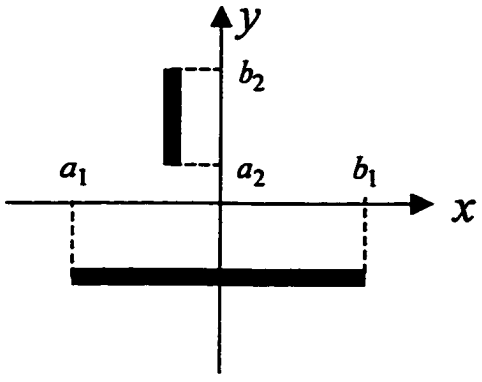

Figure 6.1 Geometry for perpendicular cracks

The derivation of the governing equations is very similar to that of the parallel crack case. The difference will come in the boundary conditions of the BVP and in the double layer representation in the boundary integral representation. Under the assumption of linear elasticity and assuming zero body forces and a time harmonic solution, the governing differential equation is given by

$$\frac{\partial^2 U}{\partial x^2}+\frac{\partial^2 U}{\partial y^2}+k^2 U=0 \tag{6.1}$$

and using a scattering approach we get the total displacement is expressible as a sum of the incident displacement and the scattered displacement.

$$U(x,y)=U^i(x,y)+U^s(x,y) \tag{6.2}$$

The differential equation for the scattered field is unchanged from the parallel crack case, namely,

$$\frac{\partial^2 U^s}{\partial x^2}+\frac{\partial^2 U^s}{\partial y^2}+k^2 U^s=0 \tag{6.3}$$

Assuming the cracks are traction free, we get the following boundary conditions.

$$\begin{aligned} \sigma_{yz}(x,h_1)&=0 \text{ for } a_1 \le x \le b_1 \\ \sigma_{xz}(h_2,y)&=0 \text{ for } a_2 \le y \le b_2 \end{aligned} \tag{6.4}$$

Using equation (6.2) in equations (6.3) and (6.4) we obtain the following BVP.

$$\frac{\partial^2 U^s}{\partial x^2}+\frac{\partial^2 U^s}{\partial y^2}+k^2 U^s=0 \tag{6.5}$$

$$\begin{aligned} \frac{\partial}{\partial y}U^s(x,h_1)&=-\frac{\partial}{\partial y}U^i(x,h_1) \text{ for } a_1 \le x \le b_1 \\ \frac{\partial}{\partial x}U^s(h_2,y)&=-\frac{\partial}{\partial x}U^i(h_2,y) \text{ for } a_2 \le y \le b_2 \end{aligned} \tag{6.6}$$

Using the Sommerfeld radiation condition and similar edge condition as before, equations (6.5) and (6.6) uniquely determine the scattered displacement field.

The Green's function for the Helmholtz equation that implicitly satisfies the Sommerfeld radiation condition is given by

$$G(x-X,y-Y)=\frac{i}{4}H_0^{(1)}(kr)$$

where

$$r=\sqrt{(x-X)^2+(y-Y)^2}$$

We now define the field operators. For an arbitrary field function f, define the field operators for the horizontal and perpendicular cracks, respectively

$$\mathbf{d}^1[f](x,y)=\int_{a_1}^{b_1} f(X)d^1(x-X,y)dX \tag{6.7}$$

$$\mathbf{d}^2[f](x,y)=\int_{a_2}^{b_2} f(Y)d^2(x,y-Y)dY \tag{6.8}$$

where

$$d^1(x-X,y)=\frac{\partial G}{\partial Y}(x-X,y-h_1)$$
$$=\frac{ik}{4}(y-h_1)\frac{H_1^{(1)}(kr_1)}{r_1} \tag{6.9}$$

and

$$d^2(x,y-Y)=\frac{\partial G}{\partial X}(x-h_2,y-Y)$$
$$=\frac{ik}{4}(x-h_2)\frac{H_1^{(2)}(kr_2)}{r_2} \tag{6.10}$$

Now we will define the field operators by taking the derivatives of the field operators $\mathbf{d^1}$ and $\mathbf{d^2}$.

$$\mathbf{d_y^1}[f](x,y)=\int_{a_1}^{b_1}f(X)d_y^1(x-X,y)dX \tag{6.11}$$

$$\mathbf{d_y^2}[f](x,y)=\int_{a_2}^{b_2}f(Y)d_y^2(x,y-Y)dY \tag{6.12}$$

$$\mathbf{d_x^1}[f](x,y)=\int_{a_1}^{b_1}f(X)d_x^1(x-X,y)dX \tag{6.13}$$

$$\mathbf{d_x^2}[f](x,y)=\int_{a_2}^{b_2}f(Y)d_x^2(x,y-Y)dY \tag{6.14}$$

where

$$d_y^1(x-X,y)=\frac{\partial^2}{\partial y\partial Y}G(x-X,y-h_1)$$
$$=\frac{ik}{4}\frac{H_1^{(1)}(kr_1)}{r_1}-\frac{ik}{4}\frac{(y-h_1)^2}{r_1^3}\left[2H_1^{(1)}(kr_1)-kr_1H_0^{(1)}(kr_1)\right] \tag{6.15}$$

$$d_x^1(x-X,y)=\frac{\partial^2}{\partial x\partial Y}G(x-X,y-h_1)$$
$$=-\frac{ik}{4}\frac{(y-h_1)(x-X)}{r_1^3}\left[2H_1^{(1)}(kr_1)-kr_1H_0^{(1)}(kr_1)\right] \tag{6.16}$$

$$d_y^2(x,y-Y)=\frac{\partial^2}{\partial y\partial X}G(x-h_2,y-Y)$$
$$=-\frac{ik}{4}\frac{(x-h_2)(y-Y)}{r_2^{\,3}}\left[2H_1^{(1)}(kr_2)-kr_2H_0^{(1)}(kr_2)\right] \tag{6.17}$$

$$d_x^2(x,y-Y)=\frac{\partial^2}{\partial x\partial X}G(x-h_2,y-Y)$$
$$=\frac{ik}{4}\frac{H_1^{(1)}(kr_2)}{r_2}-\frac{ik}{4}\frac{(x-h_2)^2}{r_2^{\,3}}\left[2H_1^{(1)}(kr_2)-kr_2H_0^{(1)}(kr_2)\right] \tag{6.18}$$

and

$$r_1=\sqrt{(x-X)^2+(y-h_1)^2}\ \text{ and }\ r_2=\sqrt{(x-h_2)^2+(y-Y)^2} \tag{6.19}$$

It will be useful to define the surface operators for the horizontal and vertical cracks. Therefore, for an arbitrary field function f, define

$$\mathbf{D_y^1}[f](x)=\mathbf{d_y^1}[f](x,h_1)$$
$$=\int_{a_1}^{b_1}f(X)D_y^1(x-X)dX\ \text{ for }\ a_1\le x\le b_1 \tag{6.20}$$

and

$$\mathbf{D_x^2}[f](y)=\mathbf{d_x^2}[f](h_2,y)$$
$$=\int_{a_2}^{b_2}f(Y)D_x^2(y-Y)dY\ \text{ for }\ a_2\le y\le b_2 \tag{6.21}$$

where

$$D_y^1(x-X)=\lim_{y\to h_1}\frac{\partial^2 G}{\partial y\partial Y}$$
$$=\frac{ik}{4}\frac{H_1^{(1)}(k|x-X|)}{|x-X|}\ \text{ for }\ a_1\le x\le b_1 \tag{6.22}$$

$$D_x^2(y-Y) = \lim_{x \to h_2} \frac{\partial^2 G}{\partial x \partial X} = \frac{ik}{4} \frac{H_1^{(1)}(k|y-Y|)}{|y-Y|} \quad \text{for } a_2 \le y \le b_2 \tag{6.23}$$

Using standard results from potential theory, the scattered field can be written in terms of the double layer potentials. Hence,

$$U^s(x,y) = \mathbf{d}^1[Q_1](x,y) + \mathbf{d}^2[Q_2](x,y) \tag{6.24}$$

where Q_1 and Q_2 are the double layer densities of the horizontal and vertical cracks respectively. Applying boundary conditions (6.6) yields the following operator notation for the system of integral equations.

$$\mathbf{D}_y^1[Q_1](x) + \mathbf{d}_y^2[Q_2](x,h_1) = -\frac{\partial}{\partial y} U^i(x,h_1) \quad \text{for } a_1 \le x \le b_1 \tag{6.25}$$

$$\mathbf{d}_x^1[Q_1](h_2,y) + \mathbf{D}_x^2[Q_2](y) = -\frac{\partial}{\partial x} U^i(h_2,y) \quad \text{for } a_2 \le y \le b_2 \tag{6.26}$$

Clearly, equations (6.25) and (6.26) comprise a set of hypersingular integral equations. The solution technique is the same as the parallel case. It should be noted, however, that the numerical complexity of the perpendicular crack problem is similar to that of the parallel crack problem. Details are therefore omitted.

6.3 Results

Each set of results will consist of two cases. The first will be for the crack arrangement to be hit by an incident wave with angle of incidence 45° and the second will use an incident wave with angle of incidence 225°.

For the first set of results we will consider two perpendicular cracks with the same length and being hit by an incident wave with incident angle 45° . See Figure 6.2

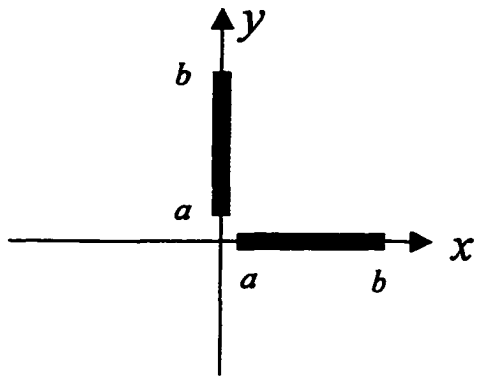

Figure 6.2 Geometry for symmetric perpendicular cracks

The crack lengths are adjusted such that a/b = 0.1, 0.2, 0.4, 0.8. The SIF of the inner edges is plotted vs. the normalized wave number kL.

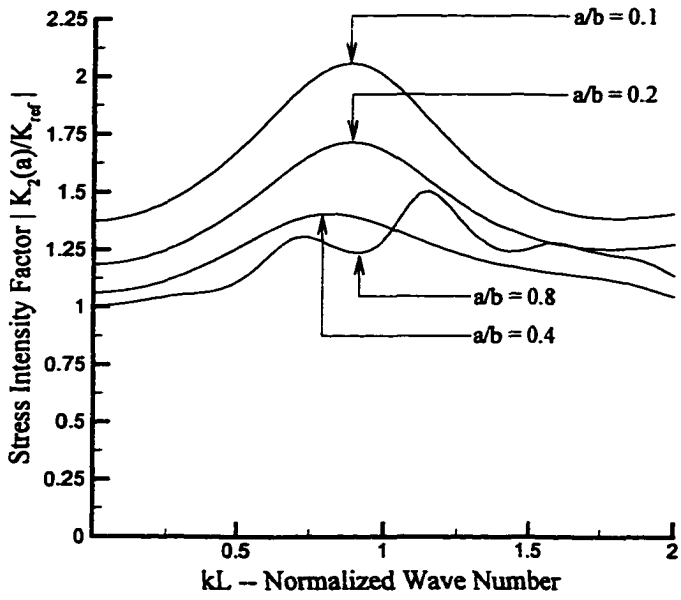

Figure 6.3 Stress Intensity Factors for symmetric perpendicular cracks (45 degrees)

In the next graph, the same parameters are used, except in the case the incident impinges on the cracks at an angle of 225 degrees.

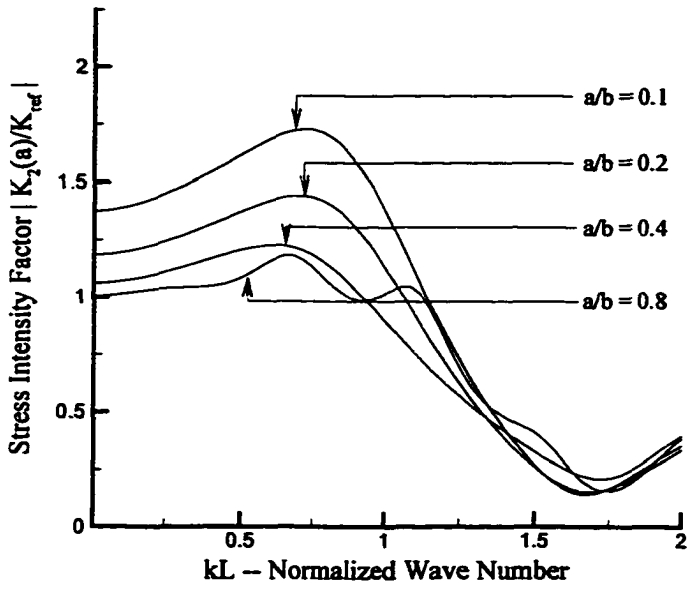

Figure 6.4 Stress Intensity Factor for symmetric perpendicular cracks (225 degrees)

Comparing Figure 6.3 and Figure 6.4 gives us some insight. Specifically, the SIF in Figure 6.3 are considerably higher than the SIF from the 225 degrees incident displacement. In addition, the SIF drop off much faster for the 225 degrees case. This observation leads to the next set of results for the perpendicular crack problem.

We will look at the effects on SIF by placing the vertical crack above the horizontal crack. Again, the angle of incidence will be 45 and 225 degrees respectively. See Figure 6.5

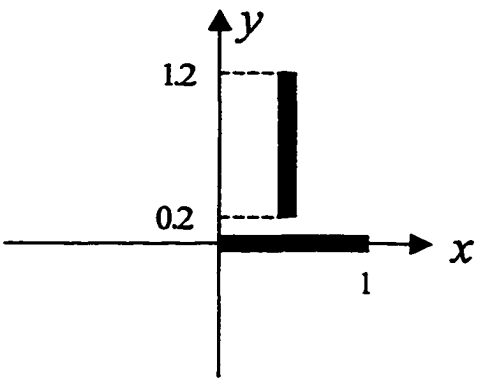

Figure 6.5 Geometry of staggered perpendicular cracks

Let h denote the distance from the vertical crack to the $y-$ axis. In the figures to follow, h is assigned as, $h = 0$, 0.25, 0.50, and 0.75. The stress intensity factor of the horizontal crack is examined.

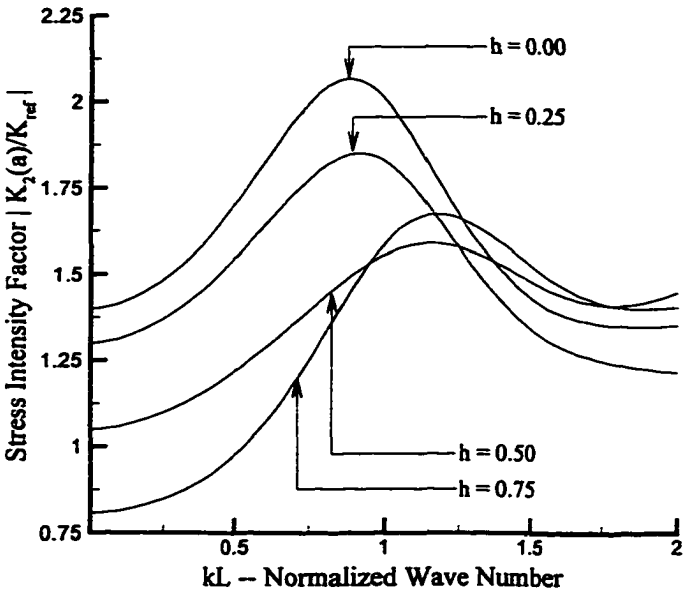

Figure 6.6 Stress Intensity Factor for staggered perpendicular cracks (45 degrees)

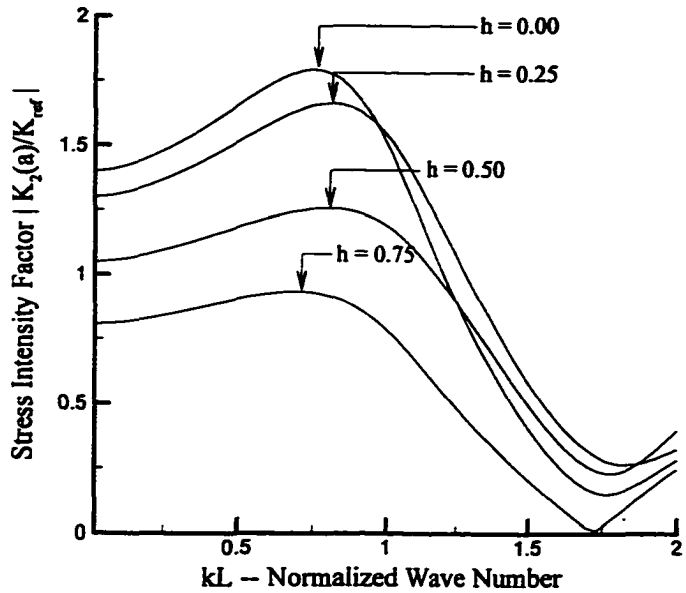

Figure 6.7 Stress Intensity Factor for staggered perpendicular cracks (225 degrees)

The last case examined is performed by holding the horizontal cracks fixed and vary the length of the perpendicular crack, being sure to maintain a constant distance between the two cracks. See Figure 6.8

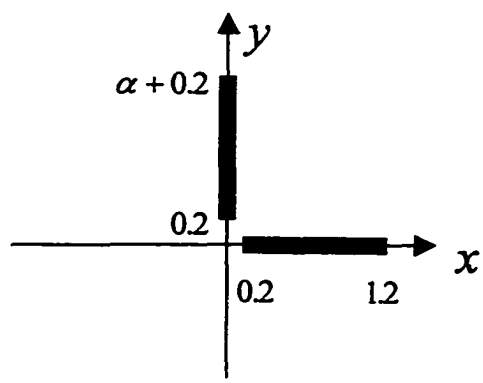

Figure 6.8 Geometry for non-symmetric perpendicular cracks

Let $\alpha = 2, 1, 0.5,$ and 0.25.

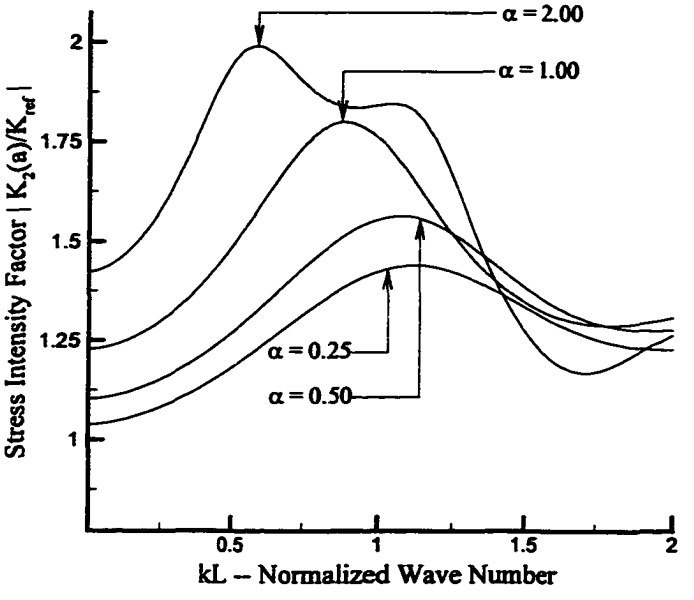

Figure 6.9 Stress Intensity Factor for non-symmetric perpendicular cracks (45 degrees)

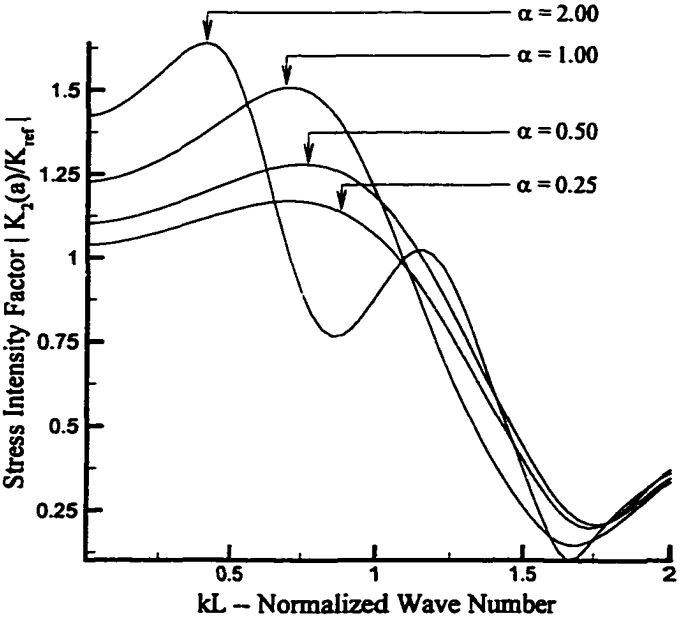

Figure 6.10 Stress Intensity Factor for non-symmetric perpendicular cracks (225 degrees)

6.4 Conclusions

As we expected, we have gained new insight into what effect a second perpendicular crack has on the SIF. Clearly, more study is required for the perpendicular cracks, but we noticed that the length and location of the perpendicular crack greatly effects the SIF of the other crack.

SECTION 7

SCATTERING OF AN INCIDENT WAVE BY A THIN MOVING WING

7.1 Introduction

Consider a wing, with uniform velocity, moving through a known sound field. The wing will scatter the acoustic pressure as it passes through the sound field and it is our goal here to model the effects of this scattering on the total acoustic pressure.

The wing is approximated by a finite, infinitesimally thin strip moving in the positive $\tilde{x}$ (axial) direction with uniform velocity $\tilde{V}_F$. The wing is located in the region of space define by $\tilde{s} = \left\{(\tilde{x},\tilde{y}) : \tilde{a} + \tilde{V}_F\tilde{t} \le \tilde{x} \le \tilde{b} + \tilde{V}_F\tilde{t},\ \tilde{y} = \tilde{h}\right\}$, see Figure 7.1. Furthermore, the wing is assumed to be rigid. That is, no sound can penetrate the strip, which means that the normal component of velocity is zero. A two-dimensional model is used, wherein the wave front of a known incident wave is in the $\tilde{x}\,\tilde{y}$ plane.

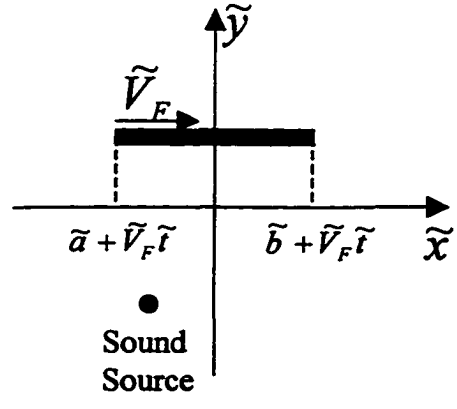

Figure 7.1 Moving wing geometry

In the sections to follow, a Neumann boundary value problem (BVP) for the scattered pressure is derived, non-dimensionalized and converted into an equivalent hypersingular integral equation using a boundary integral equation method (BIEM). This integral equation for the unknown scattered pressure is then solved using a collocation method outlined beforehand in this dissertation. Upon solving for the scattered pressure, the total acoustic pressure can be easily computed anywhere in the sound field.

7.2 Boundary Value Problem Derivation

A scattering approach is used. That is, the total acoustic pressure is expressed as a sum of a known incident pressure and an unknown scattered pressure,

$$\tilde{p}(\tilde{x},\tilde{y},\tilde{t}) = \tilde{p}_i(\tilde{x},\tilde{y},\tilde{t}) + \tilde{p}_s(\tilde{x},\tilde{y},\tilde{t}) \tag{7.1}$$

The incident pressure, $\tilde{p}_i$, is known a priori and solves the homogeneous wave equation everywhere in the sound field except at sound sources. The scattered pressure, $\tilde{p}_s$, solves the homogeneous wave equation everywhere in the sound field except on the moving wing. Hence, the total acoustic pressure satisfies the homogeneous wave equation everywhere in the sound field except on the moving wing and sound sources,

$$\left(\frac{\partial^2}{\partial\tilde{x}^2}+\frac{\partial^2}{\partial\tilde{y}^2}-\frac{1}{\tilde{c}^2}\frac{\partial^2}{\partial\tilde{t}^2}\right)\tilde{p}(\tilde{x},\tilde{y},\tilde{t}) = 0 \text{ for } (\tilde{x},\tilde{y}) \notin \{\tilde{s} \cup \text{sources}\} \tag{7.2}$$

7.3 Non-dimensionlization

Using SI units, non-dimensionalize length by $\tilde{L}$, time by $\tilde{L}/\tilde{c}$, and mass by $\tilde{\rho}_0\tilde{L}^3$. Now, define the non-dimensional variables below,

$$x=\frac{\tilde{x}}{\tilde{L}} \quad p=\frac{\tilde{p}}{\tilde{\rho}_0\tilde{c}^2} \quad a=\frac{\tilde{a}}{\tilde{L}} \quad M=\frac{\tilde{V}_F}{\tilde{c}}$$

$$y=\frac{\tilde{y}}{\tilde{L}} \quad p_i=\frac{\tilde{p}_i}{\tilde{\rho}_0\tilde{c}^2} \quad b=\frac{\tilde{b}}{\tilde{L}} \quad k=\frac{\tilde{\omega}\tilde{L}}{\tilde{c}} \tag{7.3}$$

$$t=\frac{\tilde{t}\,\tilde{c}}{\tilde{L}} \quad p_s=\frac{\tilde{p}_s}{\tilde{\rho}_0\tilde{c}^2} \quad h=\frac{\tilde{h}}{\tilde{L}} \quad \kappa=\frac{k}{\beta}$$

where $\tilde{L}$ is an arbitrary unit length, $\tilde{c}$ is the ambient speed of sound and $\tilde{\rho}_0$ is the ambient density and $\beta=\sqrt{1-M^2}$

Thus, equation (7.2) reduces to the non-dimensional wave equation

$$\left(\frac{\partial^2}{\partial x^2}+\frac{\partial^2}{\partial y^2}-\frac{\partial^2}{\partial t^2}\right)p(x,y,t)=0 \text{ for } (x,y)\notin\{s\cup\text{sources}\} \tag{7.4}$$

where

$$s=\{(x,y): a+Mt\le x\le b+Mt, y=h\} \tag{7.5}$$

7.4 Change of Variables

By choosing an appropriate change of variables, (7.4) can be written in a concise form, making the derivation of the integral equation much simpler. This section will outline the change of variables used.

Currently, the frame of reference is fixed in space. Therefore, the first change of variables will make use of a stretched, moving frame of reference

$$\begin{pmatrix} X \\ y \\ t \end{pmatrix}=\begin{pmatrix} \dfrac{x-Mt}{\beta} \\ y \\ t \end{pmatrix} \tag{7.6}$$

and in this moving frame, the wing is located in the region of space defined by

$$S = \{(X,y) : A \le X \le B, y = h\}, \text{ where } A = \frac{a}{\beta} \text{ and } B = \frac{b}{\beta} \tag{7.7}$$

and $\beta = \sqrt{1 - M^2}$ is the non-dimensional stretching constant. Upon making this change of the independent variables, the wave equation (7.2) becomes

$$\left(\frac{\partial^2}{\partial X^2} + \frac{\partial^2}{\partial y^2} + \frac{2M}{\beta}\frac{\partial^2}{\partial X \partial t} - \frac{\partial}{\partial t^2}\right) P(X,y,t) = 0 \tag{7.8}$$

where

$$P(X,y,t) = p(x,y,t) \tag{7.9}$$

Furthermore, the total acoustic pressure is assumed to be time harmonic with temporal frequency $\tilde{\omega}$. Hence, the time variable and the mixed partial derivative can be eliminated from (7.8) by making the following transformation of the dependant variables

$$P(X,y,t) = Q(X,y)e^{i(kx - \kappa M X)} \tag{7.10}$$

$$P_i(X,y,t) = Q_i(X,y)e^{i(kx - \kappa M X)} \tag{7.11}$$

$$P_s(X,y,t) = Q_s(X,y)e^{i(kx - \kappa M X)} \tag{7.12}$$

Combining (7.10) with (7.8) yields the Helmholtz equation for the new total acoustic pressure, Q,

$$\left(\frac{\partial^2}{\partial X^2} + \frac{\partial^2}{\partial y^2} + \kappa^2\right) Q(X,y) = 0 \text{ for } (X,y) \notin \{S \cup \text{sources}\} \tag{7.13}$$

where $\kappa = \frac{k}{\beta}$ is the stretched wave number and $k = \frac{\tilde{\omega}\tilde{L}}{\tilde{c}}$ is the dimensionless wave number. Furthermore, a scattering approach can be used for the new total acoustics pressure,

$$Q(X,y) = Q_i(X,y) + Q_s(X,y) \tag{7.14}$$

7.5 Boundary Condition Derivation

The total acoustic pressure and acoustic velocity are related via the acoustic momentum equation

$$\tilde{\rho}_0 \frac{\partial \tilde{\vec{u}}}{\partial \tilde{t}} + \tilde{\nabla} \tilde{p} = 0 \tag{7.15}$$

In order to make a relationship between the normal derivative of the pressure to the wing and the velocity, the y component of the momentum equation is written below,

$$\tilde{\rho}_0 \frac{\partial \tilde{u}_y}{\partial \tilde{t}} + \frac{\partial \tilde{p}}{\partial \tilde{y}} = 0 \tag{7.16}$$

where $\tilde{u}_y$ denotes the y component of the velocity. By making use of the non-dimensionalization (7.3) and $u_y = \frac{\tilde{u}_y}{\tilde{c}}$, the non-dimensional form of (7.16) is given below.

$$\frac{\partial u_y}{\partial t} + \frac{\partial p}{\partial y} = 0 \tag{7.17}$$

Using the change of variables (7.10) and (7.18) below

$$u_y(x,y,t) = V_y(X,y)e^{i(kt-\kappa MX)} \tag{7.18}$$

equation (7.17) can be written as,

$$\frac{M}{\beta}\frac{\partial V_y}{\partial X} - i\frac{\kappa}{\beta}V_y = \frac{\partial Q}{\partial y} \tag{7.19}$$

Note that in the absence of inflow, $M = 0$, equation (7.19) simplifies to

$$kV_y = i\frac{\partial Q}{\partial y} \tag{7.20}$$

otherwise, solving the first order linear O.D.E. for the velocity function in (7.19) yields the velocity written in terms of the pressure.

$$e^{-i\frac{\kappa}{M}X}V_y(X,y)=\frac{\beta}{M}\int_{-\infty}^{X}e^{-i\frac{\kappa}{M}X'}\frac{\partial Q}{\partial y}(X',y)dX' \text{ for } M\geq 0 \tag{7.21}$$

In order to express the boundary conditions in a concise manner, the introduction of field and surface functions will be defined. For an arbitrary field function $f(X,y)$, define the surface functions by,

$$f^{\pm}(X)=\lim_{y\to h^{\pm}}f(X,y) \tag{7.22}$$

where $y\to h^{+}$ implies that y approaches h in such a way that $y-h>0$, and $y\to h^{-}$ implies that y approaches h in such a way that $y-h<0$.

The wing is assumed to be rigid. Therefore, no sound can penetrate the strip. Hence, the normal component of the velocity vector across the wing is zero.

$$\left(V_y\right)^{\pm}(X)=0 \text{ for } A\leq X\leq B \tag{7.23}$$

By using condition (7.23) in (7.21), the normal velocity can be eliminated. Hence, for $M\geq 0$, the first set of boundary conditions can be written as

$$\left(\frac{\partial Q}{\partial y}\right)^{\pm}(X)=0 \text{ for } X\in[A,B] \tag{7.24}$$

and

$$\int_{-\infty}^{A}e^{-i\frac{\kappa}{M}X'}\frac{\partial Q}{\partial y}(X',y)dX'=0 \tag{7.25}$$

For $M = 0$, equation (7.25) is satisfied trivially and adds no additional information.

By approximating the wing by an infinitesimally thin strip, sharp edges are produce on both the leading and trailing edges. This will lead to non-unique solutions of (7.13) and (7.24) – (7.25). In order to guarantee uniqueness, the introduction of additional physical conditions is required. The first of these, called the Kutta condition, is imposed at the trailing edge and requires that

$$\lim_{X \to A^+} \left| Q^+(X) - Q^-(X) \right| = 0 \tag{7.26}$$

In addition, require that the total acoustic pressure be integrable over any finite region of two-dimensional space.

$$\iint_{Area} |Q| dArea < \infty \tag{7.27}$$

Lastly, the boundary value problem is finalized by imposing the Sommerfeld radiation condition, which is given by

$$\lim_{R=\sqrt{X^2+y^2} \to \infty} \sqrt{R}\left(\frac{\partial Q}{\partial R} + i\kappa Q \right) = 0 . \tag{7.28}$$

This radiation condition will guarantee that only outward traveling waves are possible at infinity.

7.6 Boundary Value Problem Summary

To complete this section, a brief summary of the Neumann boundary value problem for the scattered pressure will be given. Assume that the known incident wave Q_i and its derivative are continuous everywhere in the sound field except in source regions and satisfy the radiation conditions (7.28). By making use of (7.14) in (7.24) – (7.28), the BVP for the scattered pressure is given by

$$\left(\frac{\partial^2}{\partial X^2}+\frac{\partial^2}{\partial y^2}+\kappa^2\right)Q_s(X,y)=0 \text{ for } (X,y)\notin S \tag{7.29}$$

$$\left(\frac{\partial Q_s}{\partial y}\right)^{\pm}(X)=-\frac{\partial Q_i}{\partial y}(X,h) \tag{7.30}$$

$$\int_{-\infty}^{A} e^{-i\frac{\kappa}{M}X'}\frac{\partial Q_s}{\partial y}(X',y)dX'=-\int_{-\infty}^{A} e^{-i\frac{\kappa}{M}X'}\frac{\partial Q_i}{\partial y}(X',y)dX' \tag{7.31}$$

$$\lim_{X\to A^+}\left|Q_s^+(X)-Q_s^-(X)\right|=0 \tag{7.32}$$

$$\iint_{Area}|Q_s|dArea<\infty \tag{7.33}$$

$$\lim_{R\to\infty}\sqrt{R}\left(\frac{\partial Q}{\partial R}+i\kappa Q\right)=0 \text{ where } R=\sqrt{X^2+y^2} \tag{7.34}$$

Equations (7.29)–(7.34) uniquely determine the scattered pressure $Q_s(X,y)$ in terms of $Q_i(X,y)$ and therefore, the total pressure is determined by (7.14).

7.7 Boundary Integral Equation Method

In this section, equations (7.29) –(7.34) from the BVP are converted to an equivalent hypersingular integral equation. By using standard results from potential theory, the scattered pressure is written as a double layer Helmholtz potential. The problem of solving for the scattered pressure reduces to that of solving for an unknown double layer density. After solving for the layer density, the scattered pressure is explicitly calculated by evaluating the double layer potential.

The boundary integral formulation coupled with the solution technique is called Boundary Integral Equation Method (BIEM). BIEM has advantages over other numerical techniques such as finite difference and finite element methods. In particular,

the later techniques require the computation of the entire sound field to find the sound at any point in the sound field. In addition, extraordinary measures must be taken in order to satisfy the radiation condition. BIEM, on the other hand, solves for the boundary values only. Whence the total pressure can be evaluated at any point without having to compute the entire field. Furthermore, the far field radiation condition is implicitly satisfied. Due to the efficiency of BIEM, most calculations can be done on any mainstream PC in a few minutes.

The two-dimensional Green's function for the Helmholtz operator (7.29) that implicitly satisfies the radiation condition (7.34) is

$$G(X-X',y-y')=\frac{i}{4}H_0^{(2)}(\kappa R) \tag{7.35}$$

where

$$R=\sqrt{(X-X')^2+(y-y')^2} \tag{7.36}$$

and

$$H_0^{(2)}(Z)=J_0(Z)-iY_0(Z) \tag{7.37}$$

is the Hankel function of order zero.

In order to express the equations in a concise, readable manner, field and surface operators are introduced. The double layer field operator, **d**, is defined as follows. For an arbitrary field density f,

$$\mathbf{d}[f](X,y)=\int_A^B f(X')d(X-X',y)dX' \tag{7.38}$$

where $A=\frac{a}{\beta}$, $B=\frac{b}{\beta}$, and

$$d(X-X',y)=\frac{\partial G}{\partial y'}(X-X',y-h)=\frac{i\kappa}{4}(y-h)\frac{H_1^{(2)}(\kappa R_h)}{R_h} \tag{7.39}$$

and

$$R_h=\sqrt{(X-X')^2+(y-h)^2}$$

In addition, define a new field operator by taking the normal derivative to the wing of (7.38). This field operator takes the form

$$\mathbf{d_y}[f](X,y)=\int_A^B f(X')d_y(X-X',y)dX' \tag{7.40}$$

where

$$\begin{aligned} d_y(X-X',y) &= \frac{\partial^2 G}{\partial y\partial y'}(X-X',y-h) \\ &= \frac{i\kappa}{4}\frac{H_1^{(2)}(\kappa R_h)}{R_h}-\frac{i\kappa}{4}\frac{(y-h)^2}{R_h^3}\left[2H_1^{(2)}(\kappa R_h)-\kappa R_h H_0^{(2)}(\kappa R_h)\right] \end{aligned} \tag{7.41}$$

The operators **d** and $\mathbf{d_y}$ are continuous everywhere in the sound field except on the moving wing. The kernels, evaluated on the moving wing, are singular. The precise degree of the singularity of these operators will be discussed later.

Using results from Helmholtz potential theory, the scattered pressure can be written in terms of the double layer field operator,

$$Q_s(X,y)=\mathbf{d}[Q_2](X,y) \tag{7.42}$$

After solving for the double layer density Q_2, the total acoustic pressure is known everywhere in the sound field by

$$Q(X,y)=\mathbf{d}[Q_2](X,y)+Q_i(X,y) \tag{7.43}$$

The application of the boundary conditions (7.30) will necessitate the evaluation of $\mathbf{d}_y$ on the moving wing. Therefore, for an arbitrary field density f, define the double layer surface operator

$$\mathbf{D}_y[f](X) = \mathbf{d}_y[f](X,h) = \int_A^B f(X')D_y(X-X')dX' \tag{7.44}$$

where

$$D_y(X-X') = \lim_{y\to h}\frac{\partial^2 G}{\partial y \partial y'} = \frac{i\kappa}{4}\frac{H_1^{(2)}(\kappa|X-X'|)}{|X-X'|} \text{ for } X,X'\in(A,B) \tag{7.45}$$

For small arguments, $|X-X'| << 1$, equation (7.45) exhibits the asymptotic behavior,

$$\begin{aligned} D_y(X-X') &= \frac{i\kappa}{4}\frac{H_1^{(2)}(\kappa|X-X'|)}{|X-X'|} \\ &= -\frac{1}{2\pi}\frac{1}{(X-X')^2} + \frac{\kappa^2}{4\pi}\ln|X-X'| + D_B(X-X') \end{aligned} \tag{7.46}$$

where D_B is a bounded, continuous function across the wing. In contrast, the first term is hypersingular. That is, the corresponding divergent integral exists only in a finite part sense [16]. The logarithmic term has been extracted because although analytically integrable, it exhibits numerical difficulties. Numerical techniques have already been developed to handle these types of kernels.

The continuity of the field operators (7.38) and (7.40) is stated without proof. For sufficiently smooth field functions f,

$$\lim_{y\to h^{\pm}} \mathbf{d}[f](X,y) = \mp\frac{1}{2}f(X) \text{ for } X\in(A,B) \tag{7.47}$$

and

$$\lim_{y\to h^{\pm}} \mathbf{d}_y[f](X,y) = \mathbf{D}_y[f](X) \text{ for } X\in(A,B) \tag{7.48}$$

by applying (7.47) to (7.42), a relationship between the unknown layer density Q_2 and the jump in the scattered pressure across the wing is derived; namely

$$(Q_s)^+(X)-(Q_s)^-(X)=-Q_2(X) \text{ for } X\in(A,B). \tag{7.50}$$

By making use of the boundary conditions (7.30), the integral equation for the unknown layer density Q_2 is given by

$$\mathbf{D}_y[Q_2](X)=-\frac{\partial Q_i}{\partial y}(X,h) \text{ for } X\in(A,B). \tag{7.51}$$

Equation (7.51) is a hypersingular integral equation of the first kind with unknown double layer density Q_2.

Equation (7.51) alone does not have a unique solution Q_2. The non-uniqueness is removed by virtue of the boundary conditions (7.31) –(7.32). Asymptotic analysis about the edges of the wing along with Kutta boundary conditions (7.32) shows that the layer density can be written in the form

$$Q_2(X)=M\Phi_0\sqrt{\frac{X-A}{B-X}}+\sqrt{(B-X)(X-A)}\,F(X) \tag{7.52}$$

where Φ_0 is an unknown constant and $F(X)$ is an unknown smooth function. In the presence of motion, layer density $Q_2(x)$ has a square root singularity at the leading edge whereas at the trailing edge it is bounded due to the Kutta condition. In the absence of motion, the layer density is bounded at both edges.

Lastly, the boundary integral equation (7.51) is completed by the auxiliary condition (7.31). The boundary value problem is now replaced by an equivalent boundary integral equation

$$\mathbf{D}_y[Q_2](X) = -\frac{\partial Q_i}{\partial y}(X,h) \text{ for } X \in (A,B) \tag{7.53}$$

with subsidiary condition,

$$\int_{-\infty}^{A} e^{-i\frac{\kappa}{M}X'} \mathbf{d}_y[Q_2](X',h)dX' = -\int_{-\infty}^{A} e^{-i\frac{\kappa}{M}X'} \frac{\partial Q_i}{\partial y}(X',h)dX' \tag{7.54}$$

and a solution of the form

$$Q_2(X) = M\Phi_0\sqrt{\frac{X-A}{B-X}} + \sqrt{(B-X)(X-A)}\,F(X) \text{ for } X \in (A,B) \tag{7.55}$$

Recall that for $M = 0$, equation (7.54) is satisfied trivially and provides no additional information.

The solution of (7.53) - (7.55) is obtainable via the technique described in chapter 3. The unknown density can be written as

$$Q_2(X) = \frac{f(X)}{\Delta(X)} \text{ where } \Delta(X) = \sqrt{(B-X)(X-A)}. \tag{7.56}$$

The governing integral equations can therefore be written in the form,

$$\mathbf{D}_y[Q_2](X) = -\frac{\partial Q_i}{\partial y}(X,h) \text{ for } X \in (A,B) \tag{7.57}$$

with subsidiary conditions

$$f(A) = 0 \text{ and } \int_{-\infty}^{A} e^{-i\frac{\kappa}{M}X'} \mathbf{d}_y[Q_2](X',h)dX' = -\int_{-\infty}^{A} e^{-i\frac{\kappa}{M}X'} \frac{\partial Q_i}{\partial y}(X',h)dX' \tag{7.58}$$

7.8 Results

Consider the scattering of an incident plane wave by a thin moving wing. In the stretched, moving frame of reference the incident plane wave takes the form,

$$Q_i(X,y) = ve^{i\kappa\left(\frac{M-\cos\theta}{1-M\cos\theta}X - \frac{\beta\sin\theta}{1-M\cos\theta}y\right)} \tag{7.59}$$

in which θ is the angle between the positive axis and the direction of propagation. We will use $\theta = 225^o$ for the examples which follow.

In order to give physical meaning, dimensional units will be specified. The kinematics are chosen to approximate an airplane wing during take-off,

$$\begin{aligned} \tilde{\rho}_0 &= 1.21 \ {}^{kg}/_{m^3} \\ \tilde{c} &= 342 \ {}^{m}/_{sec} \\ \tilde{\omega} &= 7.182 \ \text{kHz} \\ \tilde{v} &= 95.55 \ \text{Pa} \end{aligned} \tag{7.60}$$

At time $\tilde{t} = 0$, the location of the wing is given by,

$$-1 \text{ m} \le \tilde{x} \le 1 \text{ m} \ ; \ \tilde{y} = 0 \text{ m} \tag{7.61}$$

In the picture that follows, the real part of the total acoustic pressure is plotted in a contour flood plot.

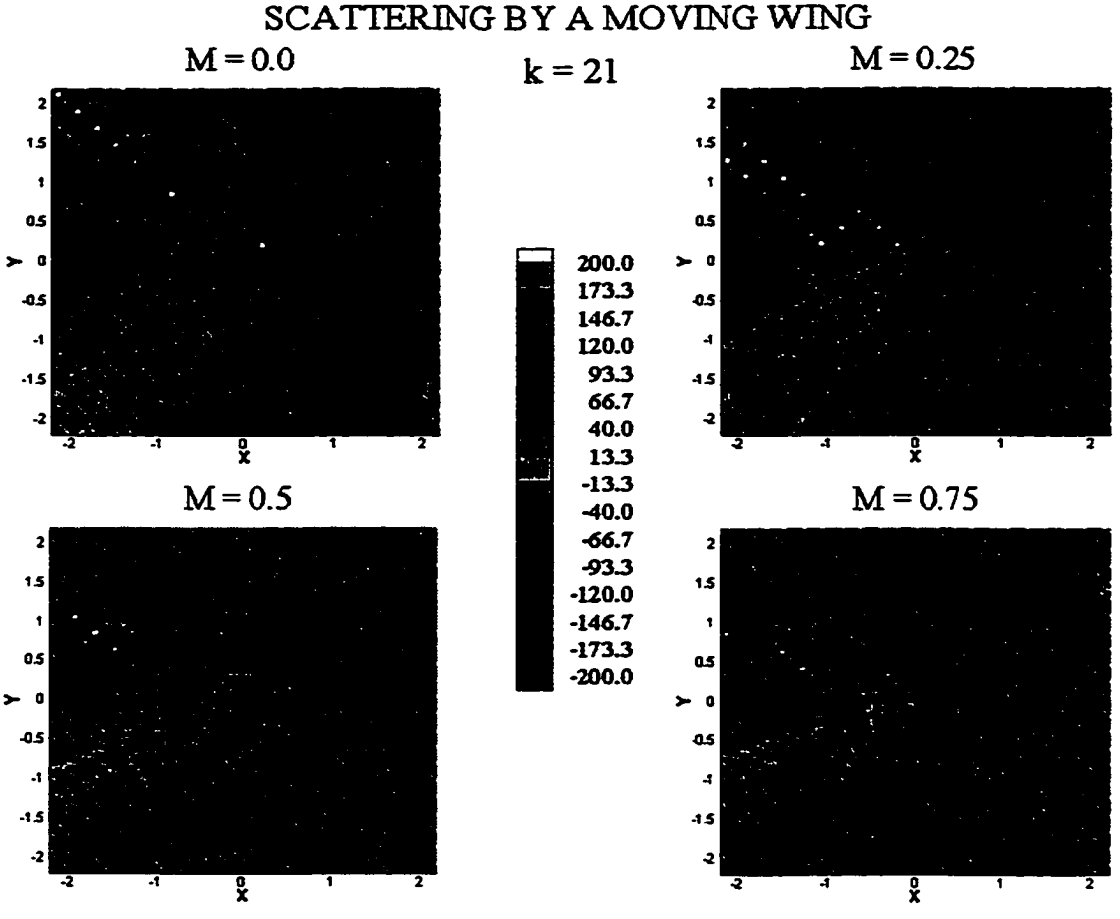

Figure 7.2 Acoustic pressure (Pascals) for a moving wing with various mach numbers

The Sound Pressure Levels, denoted SPL, of Figure 7.2 are plotted in the next picture. The sound pressure levels, measure in decibels, are given by the formula

$$SPL = 10 \log\left(\left(\frac{Q}{Q_{ref}}\right)^2\right) \tag{7.62}$$

where $Q_{ref} = 2 \times 10^{-5}$ is used to approximate the acoustic pressure due to a whisper.

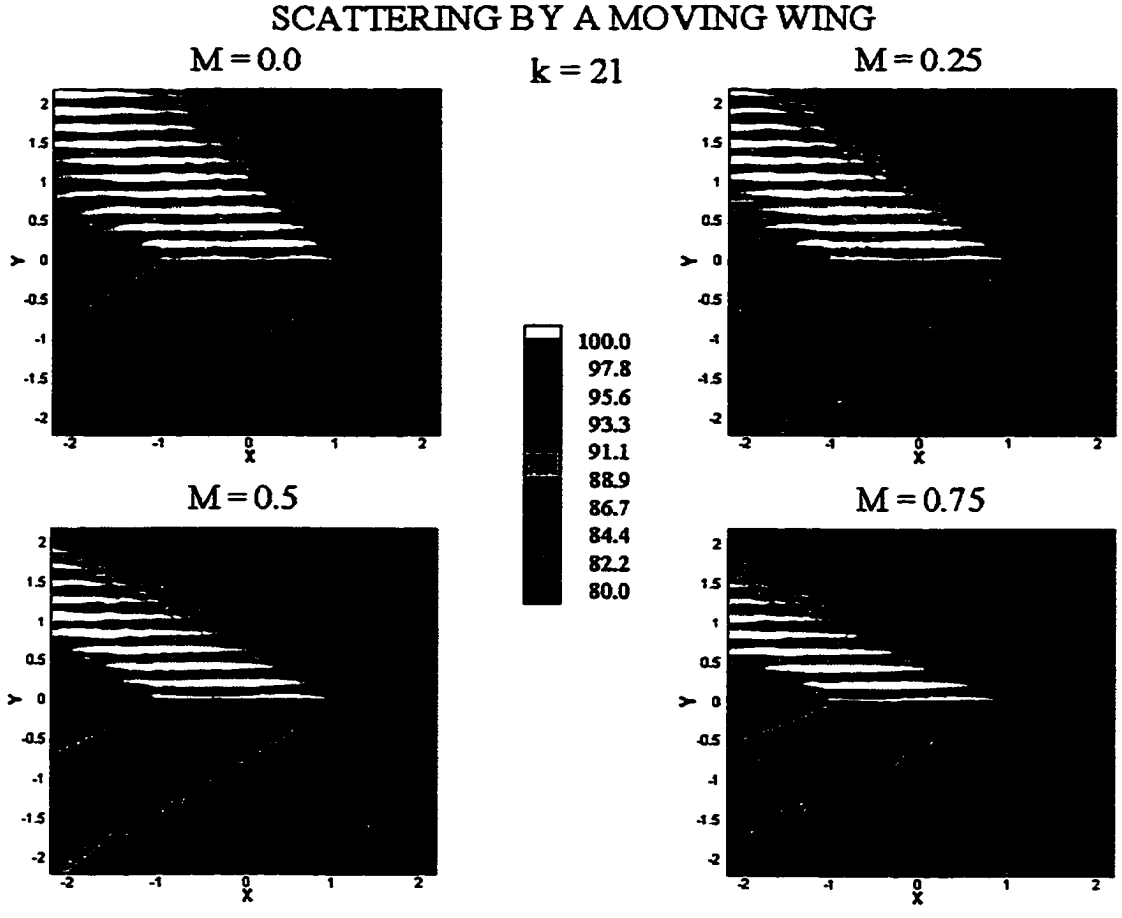

Figure 7.3 Sound pressure level (dB Re μ Pa) for a moving wing with various mach numbers

As one might expect, both plots show a very distinct shadow pattern below the wing and a reflected region above the wing.

7.9 Conclusions

The boundary integral equation method is excellent for solving the moving wing problem. In fact, this technique is fast and versatile enough to run on any mainstream PC in about 45 seconds. If we tried to run the same case using a FEM, we would not be able

to efficiently run it on a PC. For this reason, we see that the BIEM is far superior to other traditional methods.

In the next section we will consider the effects of scattering by two parallel moving strips. This problem will be termed the moving duct problem and it will be used to model an airplane engine in motion.

SECTION 8

SOUND RADIATED FROM A TWO-DIMENSIONAL FINITE DUCT

8.1 Introduction

In section 7 we established a numerical procedure for solving the moving wing problem. We solved the moving wing problem in order to develop an efficient numerical procedure for solving a more general acoustics problem. This problem is known as the moving duct problem.

For a known incident wave inside a finite, moving duct, we wish to model the effects due scattering by the duct walls of the total acoustic pressure. The geometry for the moving duct problem is given by Figure 8.1. We wish to make the shape of the duct as general as possible so we can solve a variety of problems.

Literature exists for the scattering of an incident wave by a semi-infinite duct [1, 2, 27]. The semi-infinite duct geometry is given by extending the trailing edges of the duct to negative infinity and forming an arbitrary duct inlet configuration. The dominant procedure for solving this problem is the Wiener-Hopf technique. Our goal here is to relax the semi-infinite restriction and gain new prospective to the effects of scattering for a finite, moving duct. It should be noted that the infinite duct problem, given by extending both the leading and trailing edges to infinity, is solvable in "closed form" by implementing the separation of variable technique.

Three major areas of study will be considered. The first will compare the finite duct results with the infinite duct results. Since the infinite duct has a "closed form" solution we can easily compute the spectrum for the infinite duct and compare it to the finite duct spectrum. A great deal of time will be spent on verifying that we have the correct spectrum in the finite duct solution. The reason for this is the second area of study.

After showing that the solution obtained via BIEM contains the correct spectrum we will look at the effects of a scarf inlet configuration on radiated sound. The reason we need to verify the spectral composition of the solution is that it will be shown that the direction of prominent sound radiation is directly related to the spectral composition inside the duct. In fact, we will expand on research by Peake [27]. Peake, using ray acoustic methods and a semi-infinite duct, has determined that scarf inlet designs are effective at redirecting sound away from sensitive areas. This is a form of passive noise control. Furthermore, he concluded that, for modes which are near cut-off frequency, scarf inlet is an extremely effective passive noise control technique.

The last major topic considered is the effects of resonance. It is well known that the infinite duct problem is not solvable at certain eigenfrequencies, whereas the finite duct is solvable for all frequencies. However, near the eigenfrequencies of the infinite duct, the numerical solution to the finite duct may become unstable and resonance may occur.

The geometry for the finite duct is described by two disjoint, parallel, infinitesimally thin strips see Figure 8.1. The two disjoint strips are assumed to form a duct with width $\tilde{W}$ and have inflow in the positive $\tilde{x}$ (axial) direction with uniform speed

$\tilde{V}_F$. Furthermore, the interior of the duct is assumed to be rigid. The following notation convention will be used: subscript 1 refers to the top of the duct whereas subscript 2 refers to the bottom of the duct.

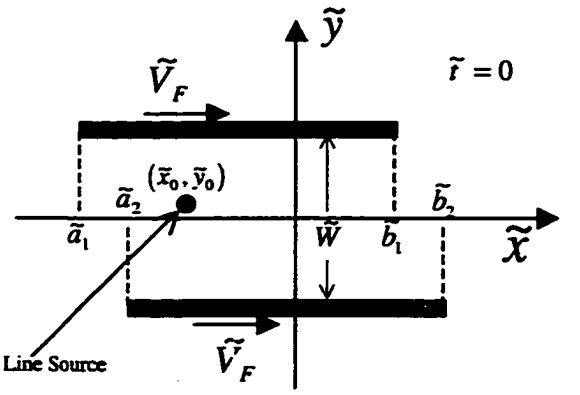

Figure 8.1 Duct geometry -- ground fixed reference frame

Define the location of the duct by

$$\tilde{s}=\left\{(\tilde{x},\tilde{y}):\tilde{a}_j+\tilde{V}_F\tilde{t}\le\tilde{x}\le\tilde{b}_j+\tilde{V}_F\tilde{t},\ \tilde{y}=\tilde{h}_j \text{ for } j=1,2\right\}. \tag{8.1}$$

8.2 Boundary Value Problem Derivation

By using a scattering approach, the total acoustic pressure is written as the sum of a known incident and an unknown scattered pressure.

$$\tilde{p}(\tilde{x},\tilde{y},\tilde{t})=\tilde{p}_i(\tilde{x},\tilde{y},\tilde{t})+\tilde{p}_s(\tilde{x},\tilde{y},\tilde{t}). \tag{8.2}$$

The total acoustic pressure satisfies the homogeneous wave equation everywhere in the sound field except on the moving wing and at sound sources $\tilde{\Omega}$. Hence,

$$\left(\frac{\partial^2}{\partial\tilde{x}^2}+\frac{\partial^2}{\partial\tilde{y}^2}-\frac{1}{\tilde{c}^2}\frac{\partial^2}{\partial\tilde{t}^2}\right)\tilde{p}(\tilde{x},\tilde{y},\tilde{t})=0 \text{ for } (\tilde{x},\tilde{y})\notin\tilde{s}\cup\tilde{\Omega}. \tag{8.3}$$

8.3 Non-dimensionalization

We will non-dimensionalize length by the duct width $\tilde{W}$, time by $\tilde{W}/\tilde{c}$, and mass by $\tilde{\rho}_0\tilde{W}^3$; where $\tilde{\rho}_0$ is the ambient density and $\tilde{c}$ is the ambient speed of sound. Hence, for $j = 1, 2$ define the following non-dimensional variables,

$$x = \frac{\tilde{x}}{\tilde{W}} \quad p = \frac{\tilde{p}}{\tilde{\rho}_0\tilde{c}^2} \quad a_j = \frac{\tilde{a}_j}{\tilde{W}} \quad M = \frac{\tilde{V}_F}{\tilde{c}}$$

$$y = \frac{\tilde{y}}{\tilde{W}} \quad p_i = \frac{\tilde{p}_i}{\tilde{\rho}_0\tilde{c}^2} \quad b_j = \frac{\tilde{b}_j}{\tilde{W}} \quad k = \frac{\tilde{\omega}\tilde{L}}{\tilde{c}} \tag{8.4}$$

$$t = \frac{\tilde{t}\tilde{c}}{\tilde{W}} \quad p_s = \frac{\tilde{p}_s}{\tilde{\rho}_0\tilde{c}^2} \quad h_j = \frac{\tilde{h}_j}{\tilde{W}} \quad \kappa = \frac{k}{\beta}$$

where $\beta = \sqrt{1 - M^2}$ is a stretching constant. Thus, equation (8.3) has the non-dimensional representation

$$\left(\frac{\partial^2}{\partial x^2} + \frac{\partial^2}{\partial y^2} - \frac{\partial^2}{\partial t^2}\right) p(x,y,t) = 0 \text{ for } (x,y) \notin s \cup \Omega \tag{8.5}$$

and for $j = 1, 2$

$$s = \left\{(x,y) : a_j + Mt \le x \le b_j + Mt,\ y = h_j\right\} \tag{8.6}$$

and Ω is the non-dimensional form of the sound source.

8.4 Change of Variables

As we did in the moving wing problem, we will introduce a stretched moving frame coordinate system,

$$\begin{pmatrix} X \\ y \\ t \end{pmatrix} = \begin{pmatrix} \dfrac{x - Mt}{\beta} \\ y \\ t \end{pmatrix} \tag{8.7}$$

Define the new dependent pressure variables below,

$$P(X,y,t) = Q(X,y)e^{i(kt-\kappa MX)} \tag{8.8}$$

$$P_i(X,y,t) = Q_i(X,y)e^{i(kt-\kappa MX)} \tag{8.9}$$

$$P_s(X,y,t) = Q_s(X,y)e^{i(kt-\kappa MX)} \tag{8.10}$$

Hence, the wave equation (8.5) is replaced by the Helmholtz equation below

$$\left(\frac{\partial^2}{\partial X^2} + \frac{\partial^2}{\partial y^2} + \kappa^2\right) Q(X,y) = 0 \text{ for } (X,y) \notin S \cup \Omega \tag{8.11}$$

where for $j = 1, 2$

$$S = \left\{(X,y): A_j \le X \le B_j,\ y = h_j\right\} \text{ with } A_j = \frac{a_j}{\beta} \text{ and } B_j = \frac{b_j}{\beta} \tag{8.12}$$

8.5 Boundary Condition Derivation

The total acoustic pressure and acoustic velocity are related via the acoustic momentum equation

$$\frac{\partial \bar{u}}{\partial t} + \nabla p = 0 \tag{8.13}$$

Furthermore, by defining the new y – component of velocity as

$$u_y(x,y,t) = V_y(X,y)e^{i(kt-\kappa MX)} \tag{8.14}$$

and making use of (8.8) the y – component of the momentum equation becomes,

$$\frac{M}{\beta}\frac{\partial V_y}{\partial X} - i\frac{\kappa}{\beta}V_y = \frac{\partial Q}{\partial y} \tag{8.15}$$

Hence,

$$e^{-i\frac{\kappa}{M}X}V_y(X,y) = \frac{\beta}{M}\int_{-\infty}^{X} e^{-i\frac{\kappa}{M}X'}\frac{\partial Q}{\partial y}(X',y)dX' \text{ for } M \geq 0 \tag{8.16}$$

In the absence of flow, equation (8.16) reduces to

$$kV_y(x,y) = i\frac{\partial Q}{\partial y} \text{ for } M = 0 \tag{8.17}$$

To better discuss the boundary conditions, surface operator notation is introduced. For an arbitrary field function $f(X,y)$, define the surface functions $f_j^{\pm}(X)$ for $j = 1,2$ by evaluating f on both sides of the duct wall, i.e.

$$f_j^{\pm}(X) = \lim_{y \to y_j^{\pm}} f(X,y) \text{ for } X \in (A_j, B_j) \tag{8.18}$$

where the notation $y \to y_j^{+}\ (y_j^{-})$ implies that y approaches y_j such that $y - y_j$ is always positive (negative).

Using surface function notation, the hardwall boundary conditions can be written as

$$(V_y)_j^{\pm}(X) = 0 \text{ for } X \in (A_j, B_j) \text{ and } j = 1,2 \tag{8.19}$$

It is convenient to express the boundary conditions in terms of pressure. Therefore, the normal velocity is eliminated by applying the momentum equation, (8.16), to (8.19). Hence, for $j = 1,2$ and $M \geq 0$, we get the following set of equations

$$\left(\frac{\partial Q}{\partial y}\right)_j^{\pm}(X) = 0 \text{ for } X \in (A_j, B_j) \tag{8.20}$$

and

$$\int_{-\infty}^{A_j} e^{-i\frac{\kappa}{M}X'} \frac{\partial Q}{\partial y}(X',y)dX' = 0. \tag{8.21}$$

Clearly, for $M = 0$ equation (8.21) is trivially satisfied and thus, provides no information.

The Kutta conditions for the duct are given by

$$\lim_{X \to A_j^-} \left[Q_j^+(X) - Q_j^-(X) \right] = 0 \text{ for } j = 1,2. \tag{8.22}$$

In addition to the Kutta condition, a farfield behavior must be specified. In particular, to ensure that only outgoing waves are possible at infinity, we impose the Sommerfeld radiation condition

$$\lim_{R \to \infty} \sqrt{R}\left(\frac{\partial Q}{\partial R} + i\kappa Q \right) = 0 \text{ where } R = \sqrt{X^2 + y^2} \tag{8.23}$$

Lastly, we will need to constrain the solution further by requiring the total acoustic pressure to be integrable over any finite region of two-dimensional space.

Now a summary of the Neumann boundary value problem for the unknown scattered pressure in terms of the known incident pressure is given. It is assumed that the incident pressure and its derivatives are continuous everywhere in the sound field except at sound sources. Furthermore, the incident pressure is assumed to satisfy the Sommerfeld radiation condition. Hence, the BVP is written as,

$$\left(\frac{\partial^2}{\partial X^2} + \frac{\partial^2}{\partial y^2} + \kappa^2 \right) Q_s(X,y) = 0 \text{ for } (X,y) \notin S \tag{8.24}$$

$$\left(\frac{\partial Q_s}{\partial y} \right)_j^{\pm} (X) = -\frac{\partial Q_i}{\partial y}(X, y_j) \text{ for } X \in (A_j, B_j) \text{ and } j = 1,2 \tag{8.25}$$

$$\int_{-\infty}^{A_j} e^{-i\frac{\kappa}{M}X'} \frac{\partial Q_s}{\partial y}(X', y_j)dX' = -\int_{-\infty}^{A_j} e^{-i\frac{\kappa}{M}X'} \frac{\partial Q_i}{\partial y}(X', y_j)dX' \text{ for } j = 1,2 \tag{8.26}$$

$$\lim_{X \to A_j^+} \left[(Q_s)_j^+(X) - (Q_s)_j^-(X) \right] = 0 \quad \text{for } j = 1,2 \tag{8.27}$$

$$\int_{\mathcal{R}} |Q_s| d\mathcal{R} < \infty \quad \mathcal{R} \text{ is any 2 - D region} \tag{8.28}$$

$$\lim_{R \to \infty} \sqrt{R} \left(\frac{\partial Q_s}{\partial R} + i\kappa Q_s \right) = 0 \quad \text{where } R = \sqrt{X^2 + y^2} \tag{8.29}$$

8.6 Boundary Integral Equation Method

In this section equations (8.24) - (8.29) are converted to an equivalent system of hypersingular integral equations. From standard potential theory results, the scattered pressure can be written as a sum of the double layer potentials. Therefore, solving for the unknown scattered pressure is reduced to solving for unknown double layer densities.

The two-dimensional Green's function for the Helmholtz operator (8.24) that implicitly satisfies the Sommerfeld radiation condition (8.29) is given by

$$G(X - X', y - y') = \frac{i}{4} H_0^{(2)}(\kappa R) \tag{8.30}$$

where

$$R = \sqrt{(X - X')^2 + (y - y')^2} \tag{8.31}$$

and

$$H_\nu^{(2)}(Z) = J_\nu(Z) - iY_\nu(Z) \tag{8.32}$$

is the ν^{th} order Hankel function of the second kind.

So that we can write the equations in a concise manner we will introduce field and surface operators. For field densities $f_j(X)$ where $X \in (A_j, B_j)$ for $j = 1,2$, define the double layer field operators, $\mathbf{d}^j$, as follows:

$$\mathbf{d}^{j}[f_j](X,y) = \int_{A_j}^{B_j} f_j(X')d^{j}(X-X',y)dX' \tag{8.33}$$

where

$$\begin{aligned} d^{j}(X-X',y) &= \frac{\partial G}{\partial y'}(X-X',y-y_j) \\ &= \frac{i\kappa}{4}(y-y_j)\frac{H_1^{(2)}(\kappa R_j)}{R_j} \end{aligned} \tag{8.34}$$

and

$$R_j = \sqrt{(X-X')^2+(y-y_j)^2} \tag{8.35}$$

The application of the boundary conditions (8.25) will necessitate taking the y - derivative of equations (8.33). Hence, the field operators $\mathbf{d}_{\mathbf{y}}^{\mathbf{j}}$ are defined by taking the y derivative of (8.33).

$$\mathbf{d}_{\mathbf{y}}^{\mathbf{j}}[f_j](X,y) = \int_{A_j}^{B_j} f_j(X')d_y^{j}(X-X',y)dX' \text{ for } j=1,2 \tag{8.36}$$

where

$$d_y^{j}(X-X',y) = \frac{i\kappa}{4}\frac{H_1^{(2)}(\kappa R_j)}{R_j} - \frac{i\kappa}{4}\frac{(y-y_j)^2}{R_j^3}\left[2H_1^{(2)}(\kappa R_j) - \kappa R_j H_0^{(2)}(\kappa R_j)\right] \tag{8.37}$$

The operators $\mathbf{d}^{\mathbf{1}}$ and $\mathbf{d}_{\mathbf{y}}^{\mathbf{1}}$ $\left(\mathbf{d}^{\mathbf{2}} \text{ and } \mathbf{d}_{\mathbf{y}}^{\mathbf{2}}\right)$ are well defined and continuous everywhere in the sound field except possibly for points on the upper (lower) part of the duct. These kernels, evaluated on the duct surface, are singular and the precise degree of singularity will be discussed later.

Using results from potential theory the scattered pressure can be written as a sum of the double layer potentials [9, 30]

$$Q_s(X,y) = \mathbf{d}^{1}[Q_1](X,y) + \mathbf{d}^{2}[Q_2](X,y). \tag{8.38}$$

The functions Q_1 and Q_2 are the unknown double layer densities on the upper and lower duct strips, respectively. Once the layer densities have been determined, equation (8.38) is evaluated to find the scattered acoustic pressure and hence, the total acoustic pressure is known at any desired location.

By direct application of boundary conditions (8.25), a system of integral equations is derived for Q_1 and Q_2. However, to apply (8.25) to (8.38) it is necessary to evaluate the field operator on the duct surface. Hence, the following surface operators are defined

$$\begin{aligned}\mathbf{D}_{\mathbf{y}}^{j}[f_j](X) &= \mathbf{d}_{\mathbf{y}}^{j}[f_j](X, y_j) \\ &= \int_{A_j}^{B_j} f_j(X') D_y^j(X - X')\, dX' \quad \text{for } X \in (A_j, B_j) \text{ and } j = 1,2\end{aligned} \tag{8.39}$$

where

$$\begin{aligned}D_y^j(X - X') &= \lim_{y \to y_j} \frac{\partial^2 G}{\partial y \partial y'} \\ &= \frac{i\kappa}{4} \frac{H_1^{(2)}(\kappa |X - X'|)}{|X - X'|} \quad \text{for } X, X' \in (A_j, B_j)\end{aligned} \tag{8.40}$$

The kernels (8.40) are singular and small argument analysis of the Hankel function yields the following result

$$D_y^j(X - X') = -\frac{1}{2\pi} \frac{1}{(X - X')^2} + \frac{\kappa}{4\pi} \ln|X - X'| + D_B^j(X - X') \text{ as } |X - X'| \to 0 \tag{8.41}$$

where $D_B^j = O(1)$. The leading term in (8.41) is hypersingular. Consequently, integrals such as (8.39) are divergent and must be interpreted in the Hadamard finite part sense [16]. In addition, the logarithmic term has been extracted because although integration involving the logarithmic term is analytically feasible, difficulties arise upon evaluating the integral numerically.

The continuity of the field operators (8.33) and (8.36) is stated without proof. For sufficiently smooth surface functions $f_j(X), j=1,2$, defined for $X \in (A_j, B_j)$, the following limits are given:

$$\lim_{y \to y_j^{\pm}} \mathbf{d}^j[f_j](X,y) = \mp\frac{1}{2} f_j(X) \text{ for } X \in (A_j, B_j) \tag{8.42}$$

and

$$\lim_{y \to y_j^{\pm}} \mathbf{d}_{\mathbf{y}}^j[f_j](X,y) = \mathbf{D}_{\mathbf{y}}^j[f_j](X) \text{ for } X \in (A_j, B_j). \tag{8.43}$$

Applying (8.42) to (8.38) yields the well-known results

$$(Q_s)_j^+(X) - (Q_s)_j^-(X) = -Q_j(X) \text{ for } X \in (A_j, B_j) \text{ and } j = 1,2. \tag{8.44}$$

That is, the double layer densities are equivalent to the jump in scattered pressure across the duct surface.

By applying (8.38) to the boundary conditions (8.25) and making use of the surface operator notation, the system of hypersingular integral equation can be written as

$$\mathbf{D}_{\mathbf{y}}^1[Q_1](X) + \mathbf{d}_{\mathbf{y}}^2[Q_2](X, y_1) = -\frac{\partial Q_i}{\partial y}(X, y_1) \text{ for } X \in (A_1, B_1) \tag{8.45}$$

and

$$\mathbf{d}_{\mathbf{y}}^1[Q_1](X, y_2) + \mathbf{D}_{\mathbf{y}}^2[Q_2](X) = -\frac{\partial Q_i}{\partial y}(X, y_2) \text{ for } X \in (A_2, B_2). \tag{8.46}$$

Equations (8.45) and (8.46) comprise a system of one dimensional, hypersingular integral equations of the first kind for the unknown double layer densities Q_1 and Q_2. However, to uniquely determine Q_1 and Q_2, the boundary conditions (8.26) - (8.28) are needed. Asymptotic analysis of (8.45) and (8.46) about the duct edges together with conditions (8.26) and (8.28) show that the layer densities must have the form [12]

$$Q_j(X) = M\Phi_j\sqrt{\frac{X-A_j}{B_j-X}} + \sqrt{(B_j-X)(X-A_j)}\,F_j(X) \text{ for } X \in (A_j, B_j) \text{ and } j = 1,2 \quad (8.47)$$

In (8.47), Φ_j are unknown constants and F_j are unknown smooth functions. In the presence of flow, the layer densities have square root singularities at the leading edges of the duct whereas at the trailing edges they are zero due to the Kutta condition. In the absence of motion, the layer densities are zero at both ends.

A summary of the boundary integral equations will now be given. For $j = 1, 2$

$$\mathbf{D}_y^1[Q_1](X) + \mathbf{d}_y^2[Q_2](X, y_1) = -\frac{\partial Q_i}{\partial y}(X, y_1) \text{ for } X \in (A_1, B_1) \quad (8.48)$$

$$\mathbf{d}_y^1[Q_1](X, y_2) + \mathbf{D}_y^2[Q_2](X) = -\frac{\partial Q_i}{\partial y}(X, y_2) \text{ for } X \in (A_2, B_2) \quad (8.49)$$

$$\int_{-\infty}^{A_j} e^{-i\frac{\kappa}{M}X'} \left\{\mathbf{d}_y^1[Q_1](X', y_j) + \mathbf{d}_y^2[Q_2](X', y_j)\right\} dX' = -\int_{-\infty}^{A_j} e^{-i\frac{\kappa}{M}X'} \frac{\partial Q_i}{\partial y}(X', y_j) dX' \quad (8.50)$$

$$Q_j(X) = M\Phi_0\sqrt{\frac{X-A_j}{B_j-X}} + \sqrt{(B_j-X)(X-A_j)}\,F_j(X) \text{ for } X \in (A_j, B_j) \quad (8.51)$$

Recall that for $M = 0$, equations (8.50) provides no additional information and the first term in (8.51) vanishes.

A collocation method for solving (8.48) - (8.51) has been developed by the author and coworkers [7]. In particular, a FORTRAN subroutine, TBIEM2D [31], has been written to numerically solve (8.48) - (8.51) and is used to obtain the results which follow.

8.7 Spectral Analysis

In order to test the accuracy of the numerical procedure, the spectrum of the infinite duct is compared to the spectrum of the finite duct. It is clear that for a

sufficiently long duct, the spectrum of the finite duct approaches the axial wave numbers of the infinite duct. It will be this approximation on which we focus.

Assume the infinite duct has width $2h$ and is symmetrically located about the $x-$ axis. In the stretched moving frame, at time $t=0$, the infinite duct problem is given by

$$\begin{gathered}\left(\frac{\partial^2}{\partial X^2}+\frac{\partial^2}{\partial y^2}+\kappa^2\right)\left\{e^{i\kappa MX}P(X,y)\right\}=0 \\ \frac{\partial}{\partial y}\left\{e^{i\kappa MX}P(X,\pm h)\right\}=0\end{gathered} \tag{8.52}$$

Using separation of variables let $P(X,y)=F(X)Y(y)$. Hence, equations (8.52) reduces to

$$\begin{gathered}\left\{F''+2i\kappa MF'-\kappa^2M^2F\right\}Y+Y''F+\kappa^2FY=0 \\ Y'(\pm h)=0\end{gathered} \tag{8.53}$$

Therefore,

$$\frac{Y''}{Y}=-\kappa^2-\frac{F''+2i\kappa MF'-\kappa^2M^2F}{F}=-\lambda^2 \tag{8.54}$$

$$\begin{aligned}&\Rightarrow Y''+\kappa^2Y=0 \text{ with } Y'(\pm h)=0 \\ &\Rightarrow Y_n(y)=A_1\cos\left[\lambda_n(y-h)\right]\end{aligned} \tag{8.55}$$

where

$$\lambda_n=\frac{n\pi}{2h} \text{ for } n=0,1,... \tag{8.56}$$

and the O.D.E for F becomes

$$F''+2i\kappa MF'-\left(\kappa^2M^2+\lambda^2-\kappa^2\right)F=0 \tag{8.57}$$

Hence,

$$F_n(X)=A_n^+e^{i\Gamma_n^+X}+A_n^-e^{i\Gamma_n^-X} \tag{8.58}$$

where

$$\Gamma_n^{\pm} = \kappa M \pm \sqrt{\kappa^2 - \lambda_n{}^2} \tag{8.59}$$

So, in the unstretched, moving frame of reference,

$$f_n(x) = A_n^+ e^{i\gamma_n^+ x} + A_n^- e^{i\gamma_n^- x} \text{ where } \gamma_n^{\pm} = \frac{\Gamma_n^{\pm}}{\beta} \tag{8.60}$$

where $f_n(x) = F_n(X)$

Hence, in the unstretched, moving frame of reference, the pressure field inside the duct has the form

$$p(x,y,t) = e^{ikt} \sum_{n=0}^{N} \cos\left[\lambda_n (y-h)\right] \left\{ A_n^+ e^{i\gamma_n^+ x} + A_n^- e^{i\gamma_n^- x} \right\} \tag{8.61}$$

where $A_n^{\pm}$ are constants such that the only the propagating modes are present. Hence,

$$0 \le N < \frac{2h\kappa}{\pi} \tag{8.62}$$

Furthermore, γ_n^+ denotes left travelling wave, whereas

$$\gamma_n^- = \begin{cases} \text{right travelling waves for } n < \dfrac{2hk}{\pi} \\ \text{left travelling for } n > \dfrac{2hk}{\pi} \end{cases} \tag{8.63}$$

8.8 Spectral Analysis Results

Throughout the results to follow, combinations of axial dipole line sources will be used as the sound source. In the stretched, moving frame the non-dimensional axial dipole, centered at (X_0, y_0), produced the incident field

$$Q_i(X,y)=v\left\{(X-X_0)\frac{H_1^{(2)}(\kappa r)}{r}+iMH_0^{(2)}(\kappa r)\right\} \tag{8.64}$$

where

$$r=\sqrt{(X-X_0)^2+(y-y_0)^2}\,. \tag{8.65}$$

and $v=\dfrac{\tilde{v}}{\tilde{W}\tilde{\rho}_0\tilde{c}^2}$ is the non-dimensional source strength. The SI units of the sound source are given by $^{\text{Newtons}}/_{\text{unit length}}$. Furthermore, it will be understood that all results are taken at time $\tilde{t}=0$ with the following choice of parameters, unless otherwise stated.

$$\begin{aligned}&\tilde{\rho}_0=1.21\ {}^{\text{kg}}/_{\text{m}^3}\\&\tilde{c}=342\ {}^{\text{m}}/_{\text{sec}}\\&\tilde{W}=1\text{ m}\\&\text{Duct length}=2\text{ m}\end{aligned} \tag{8.66}$$

The first case will focus on a stationary, symmetric duct of length 2 meters with one axial dipole centered in the center of the duct, see Figure 8.2

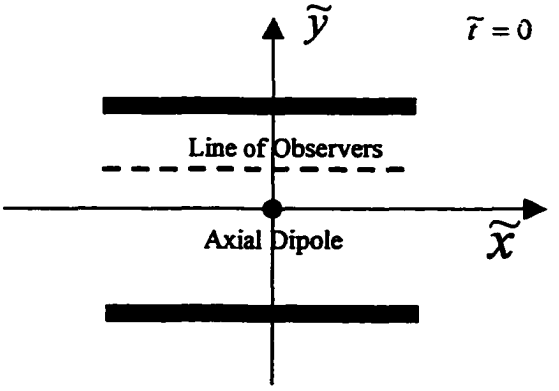

Figure 8.2 Geometry for one symmetrically placed axial dipole line source

In order to test the accuracy of the method used to solve the finite duct problem, we will compare the axial spectrum from the infinite duct with the axial spectrum from the finite duct. The spectrum of the infinite duct is computed analytically from equation (8.60). For the finite duct, the total acoustic pressure is computed for a line of observers inside the duct. The Fourier transform is computed for this line of observer to see the spectral compositions for the pressure. This is compared with the spectrum computed from the infinite duct. It should be noted that the location and type of source will effect which modes are cut on and which are not. Three cases will be examined: one with only even modes, one with only odd modes, and one with even and odd modes.

Firstly, we wish to use a source that will produce only even modes. The axial dipole is an even function in y about its center. Therefore, due to the symmetry of the duct, only the coefficients of the even eigenfunctions are nonzero. Therefore, only the even axial spectrum is present. The top graphic in Figure 8.3 shows the analytic spectrum compared to the finite duct spectrum for $\tilde{\omega} = 6.498$ kHz and a source strength of $\tilde{\nu} = 150\ {}^{N}/_{m}$. The lower left picture is the total acoustic pressure, measured in Pascals and the lower right is a plot of the sound pressure levels, measured in decibels, where

$$SPL = 20\log\left(\frac{P}{P_{ref}}\right) \text{ where } P_{ref} = 2.0\times10^{-5} \tag{8.67}$$

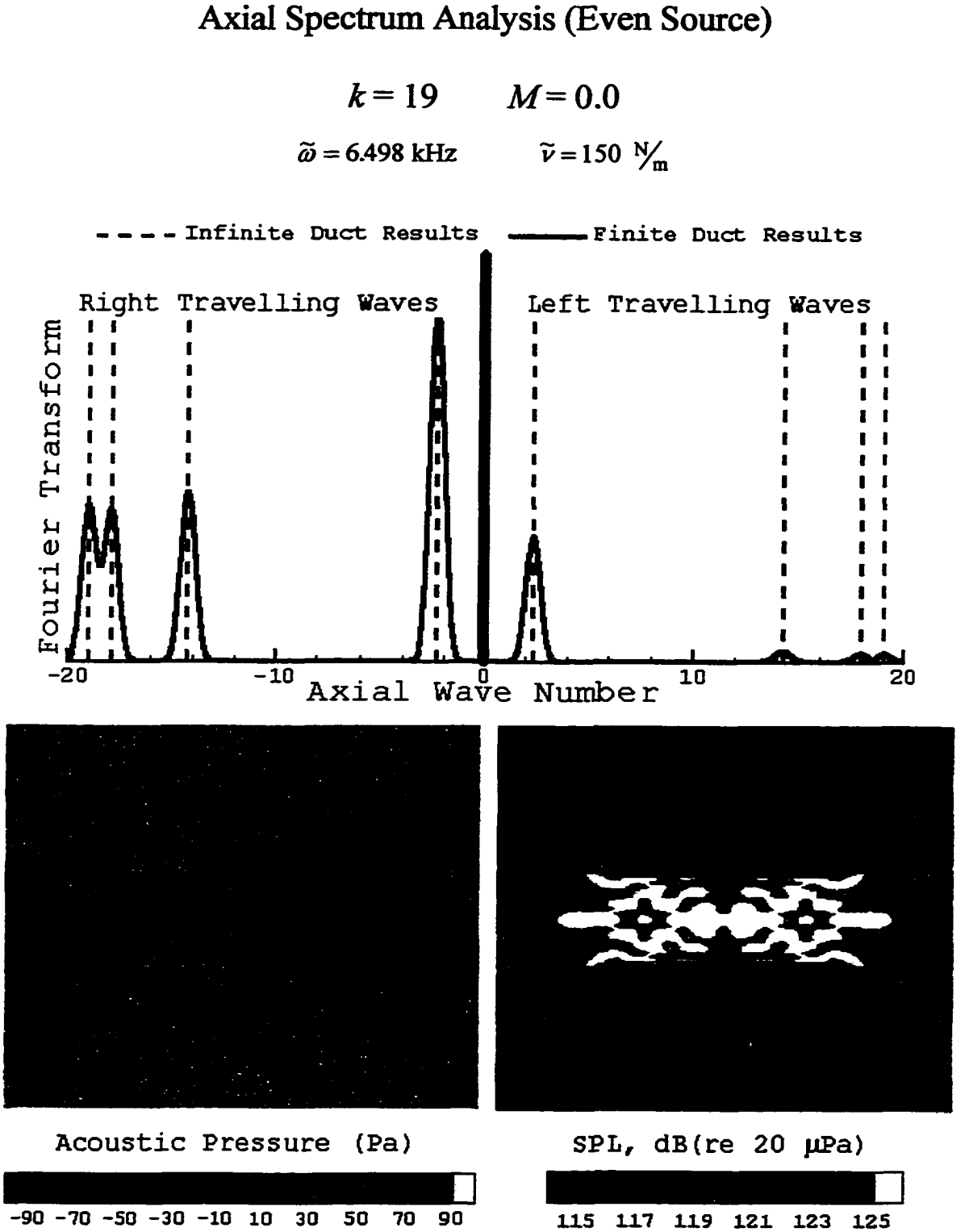

Figure 8.3 Conventional, stationary duct with one symmetrically placed axial dipole line source

Clearly, the finite duct spectrum agrees very well with the infinite duct theory. In particular, no extraneous numerical noise is present and only the correct modes are turned on.

To further test the technique developed for the finite duct problem, consider using an odd sound source, meaning that only the odd eigenfunctions are present in the analytic solution. Using two axial dipole line sources of opposite strength placed symmetrically about the x – axis can do this. See Figure 8.4

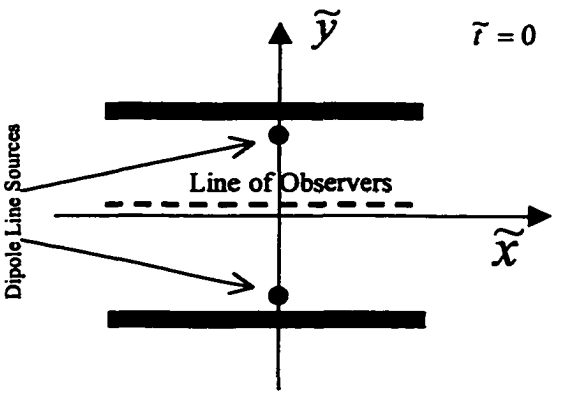

Figure 8.4 Geometry for two symmetrically placed axial dipoles with opposite strengths

Using this array of axial dipoles, the total sound source is an odd function in y about the x – axis. Therefore, the only nonzero components of the solution are the odd eigenfunctions. Using the parameters from equation (8.66), $\tilde{\omega} = 6.498$ kHz, and the source strengths are $\tilde{v}_1 = 150\ {}^{N}/_{m}$ and $\tilde{v}_2 = -150\ {}^{N}/_{m}$.

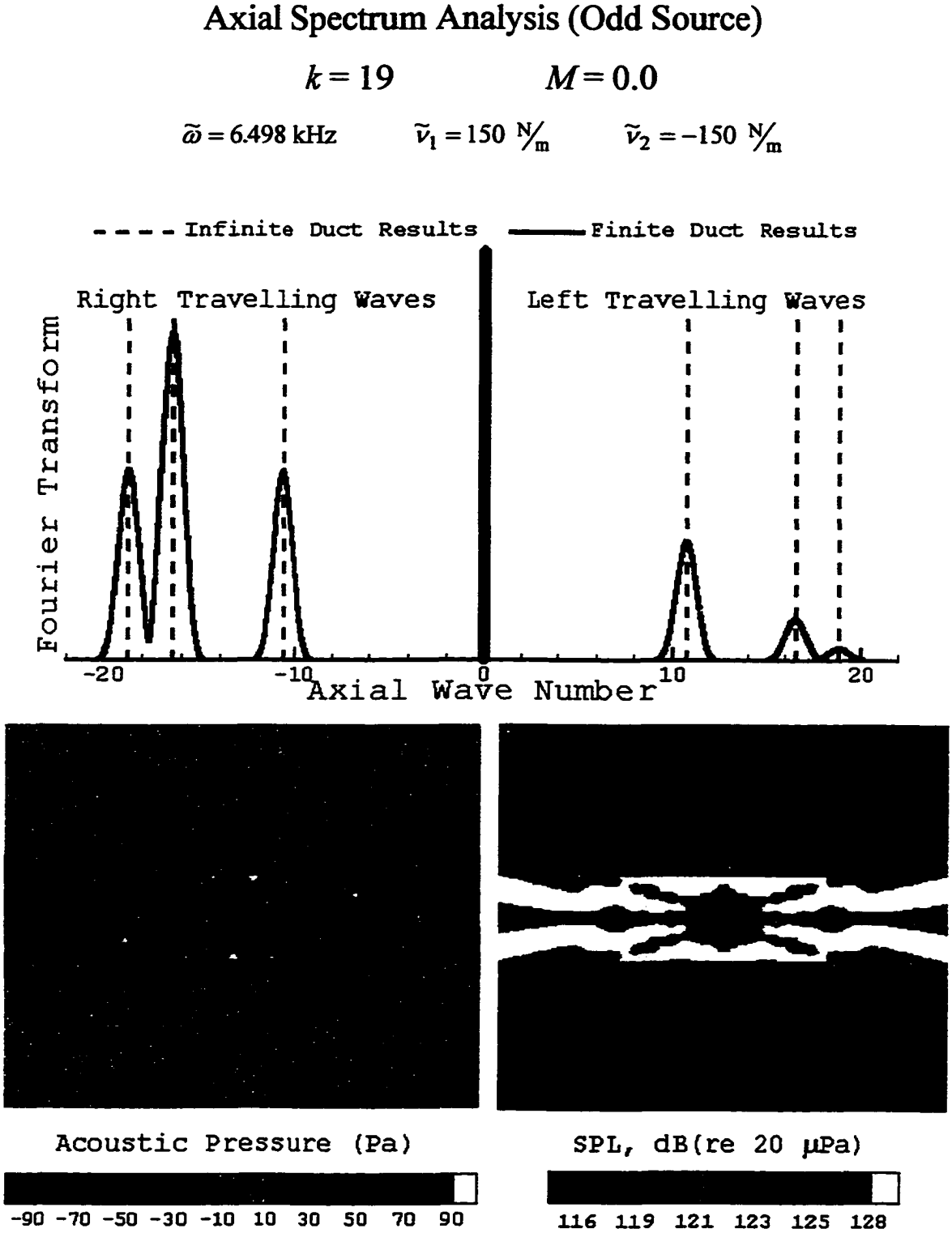

Figure 8.5 Conventional, stationary duct with
two symmetrically placed axial dipole line sources of opposite strength

Again, the spectrum of the finite duct agrees very well with the infinite duct case. However, the SPL plot shows that the noise is exiting the duct in a narrow channel whereas in the single dipole case, the noise was in a much wider pattern. This phenomenon will be examined in depth in the section on Ray Acoustics.

The next example will look at a source that is neither even nor odd. Therefore all cut-on modes are present. Using one axial dipole line source located non-symmetrically in the duct accomplishes this. See Figure 8.6

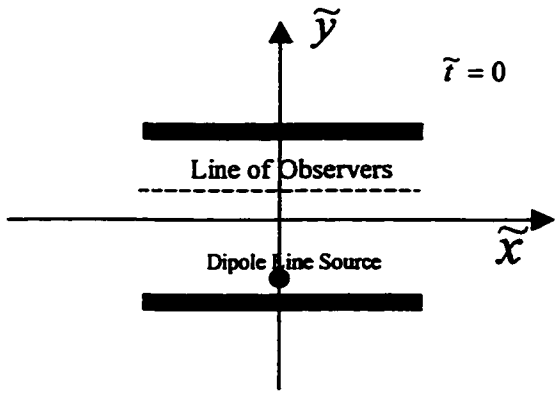

Figure 8.6 Geometry for one non-symmetrically placed axial dipole line source

The parameters used are given by (8.66). Furthermore, the frequency and source strength given by $\tilde{\omega} = 6.498$ kHz and $\tilde{v} = 150\ {}^{N}/_{m}$.

The spectrum for the infinite duct case is very complicated with the above parameters. In particular, there are 14 cut-on modes; seven right travelling and seven left travelling waves. The following graphic shows the comparisons. Of particular interest are the 0^{th} and the 1^{st} modes. It appears that the finite duct does not contain both modes. However, from the two previous examples, it seems as though both are included. This

implies that in the asymmetric case, the 0^{th} and 1^{st} modes are present but they are so close together that the are undistinguishable. A very long duct is required to isolate those two modes.

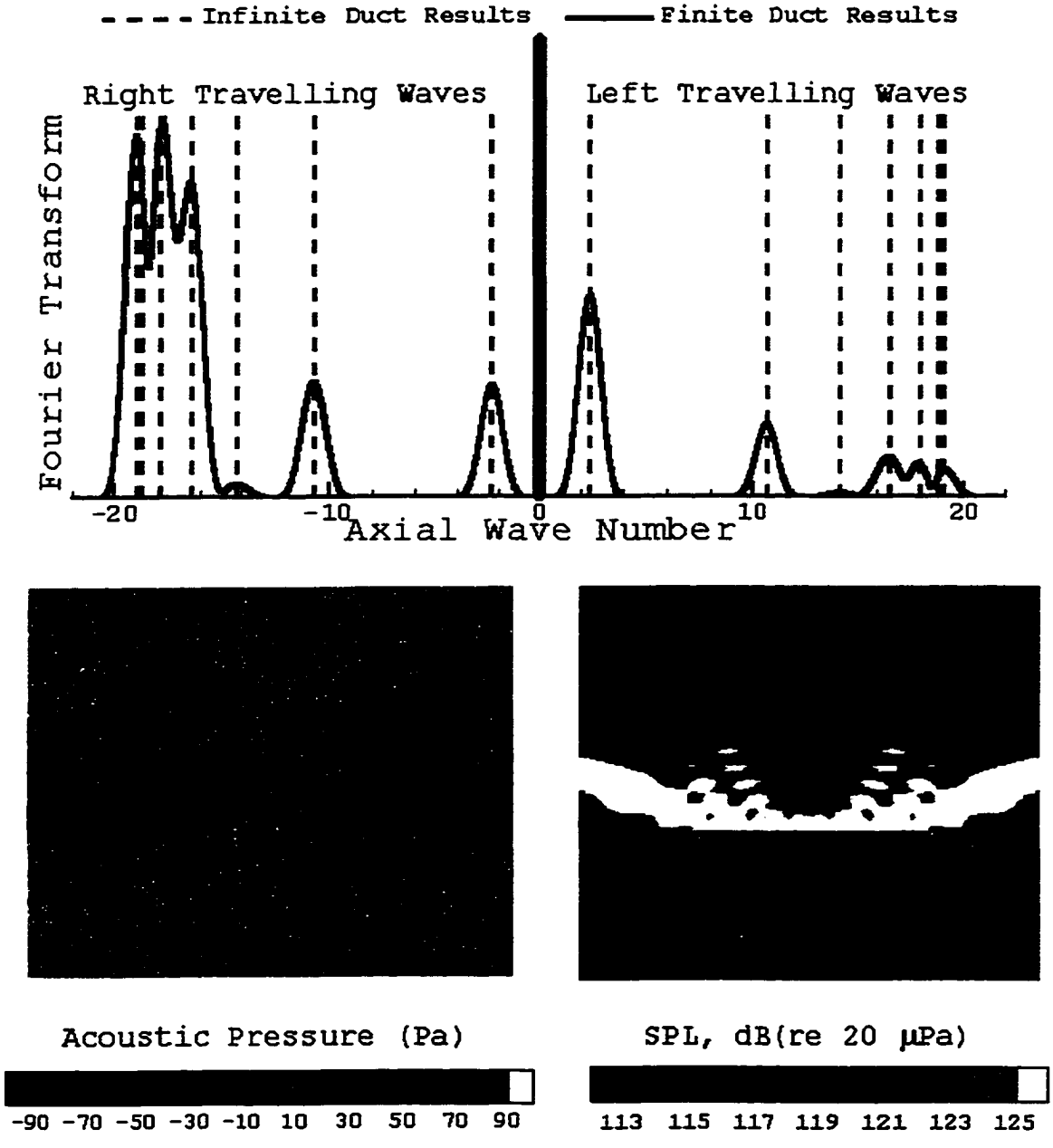

Figure 8.7 Conventional, stationary duct with one non-symmetrically placed axial dipole line source

The SPL pattern in Figure 8.7 is quite interesting. The sound is reflected up as it exits the duct. Much more noise is being reflected in the first and second quadrants than in the third and fourth. Later, a technique, which is based on reflecting sound away from sensitive areas, is examined.

The last stationary case will look at the effect of a frequency that is below the cut-on frequency. For this particular geometry and an odd source, the cut-on frequency is $k = \pi$. Hence, we will use the two-dipole case and let $\tilde{\omega} = 1$ kHz.

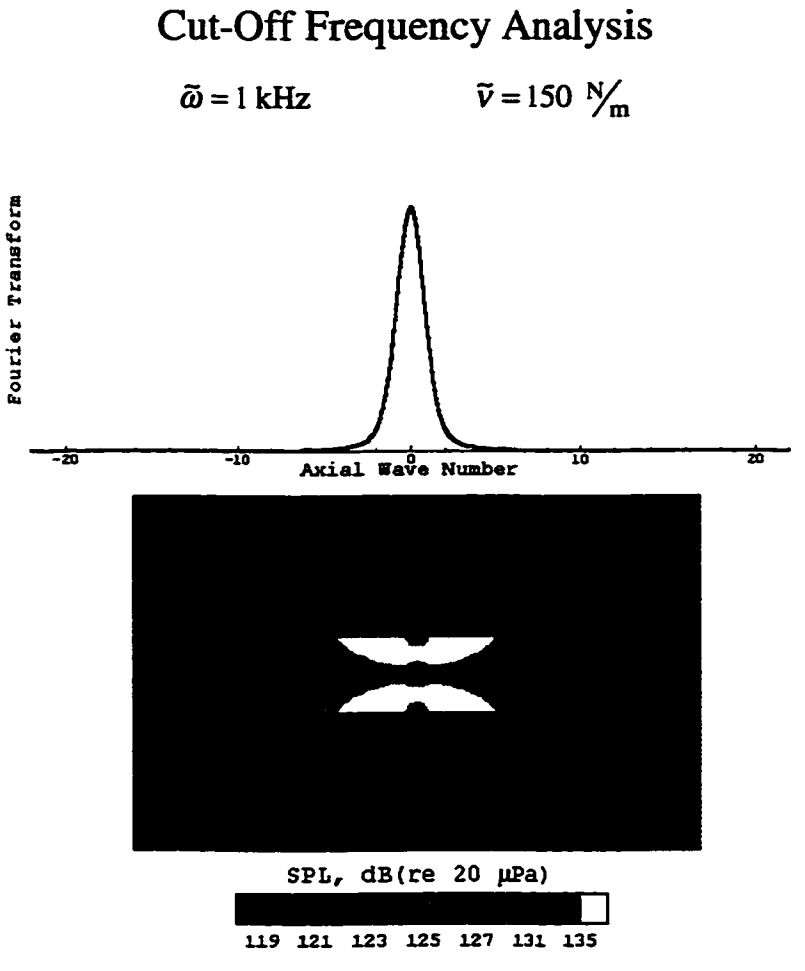

Figure 8.8 Sound pressure levels for a source below cut-on frequency

This is particularly interesting because only the decaying modes are present. It is clear from Figure 8.8 that the modes decay very rapidly and very little sound is propagated out of the duct. This concludes the stationary spectral analysis. Now the focus will shift to results from a moving, symmetric duct.

The following results for the moving conventional duct are based on two symmetrically placed axial dipoles of opposite strength. The following parameters will be used:

$$\begin{aligned} &\tilde{\rho}_0 = 1.21 \ {}^{kg}/_{m^3} \\ &\tilde{c} = 342 \ {}^{m}/_{sec} \\ &\tilde{\omega} = 6.84 \text{ kHz} \\ &\tilde{\nu}_1 = -\tilde{\nu}_2 = 150 \ {}^{N}/_{m} \\ &\tilde{W} = 1 \text{ m} \\ &\text{Duct length} = 1 \text{ m} \end{aligned} \tag{8.68}$$

The velocity of the duct for the first case will be $70 \ {}^{m}/_{sec}$. In the two cases that follow, the velocity is $140 \ {}^{m}/_{sec}$ and $210 \ {}^{m}/_{sec}$, respectively. Due to the fact that the right travelling waves are being compressed and the left travelling waves are being stretched, there is more noise in front of the source than behind the source.

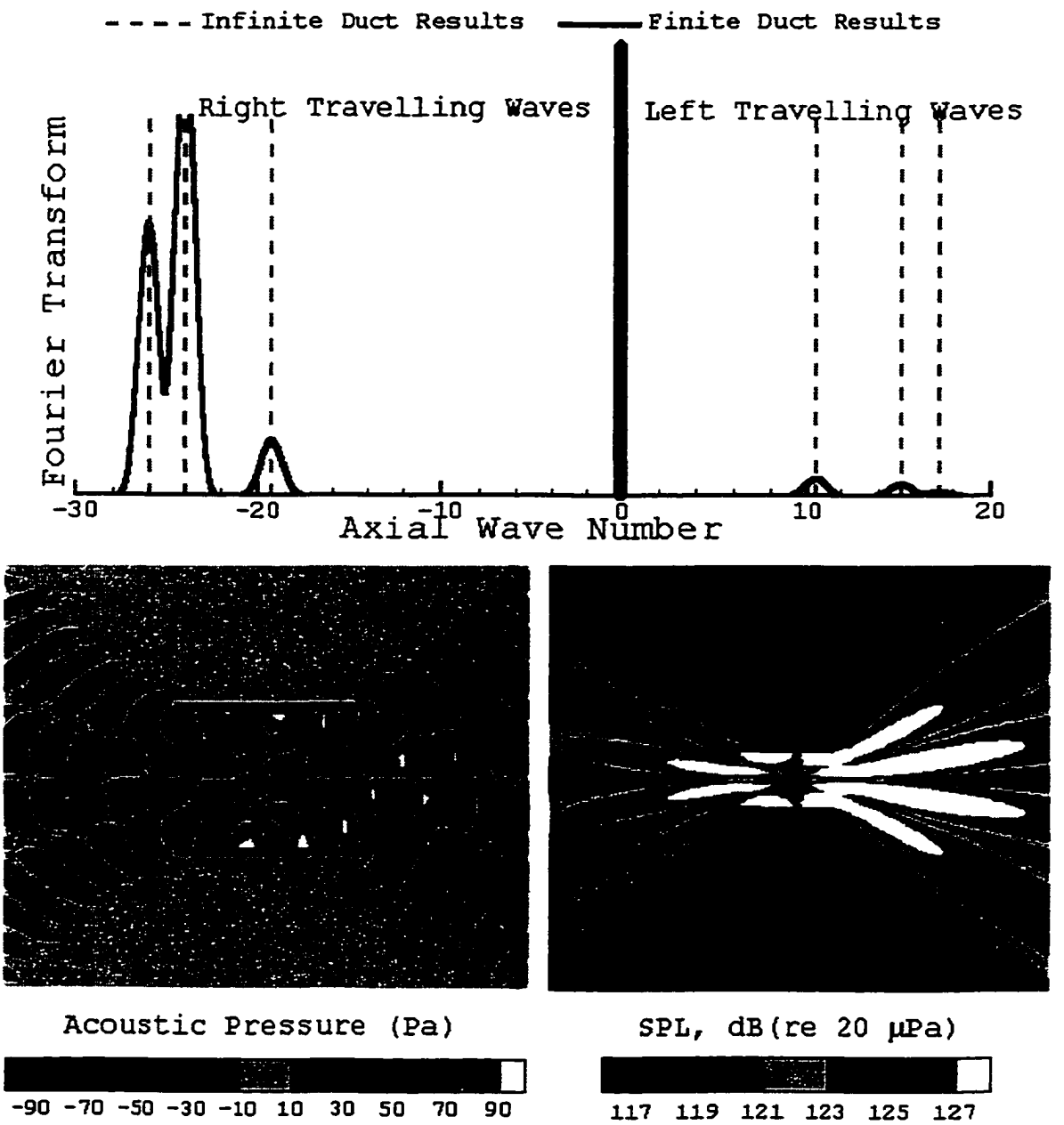

Figure 8.9 Spectral analysis $M = 0.2$

Spectral Analysis

$k = 20$ $M = 0.4$

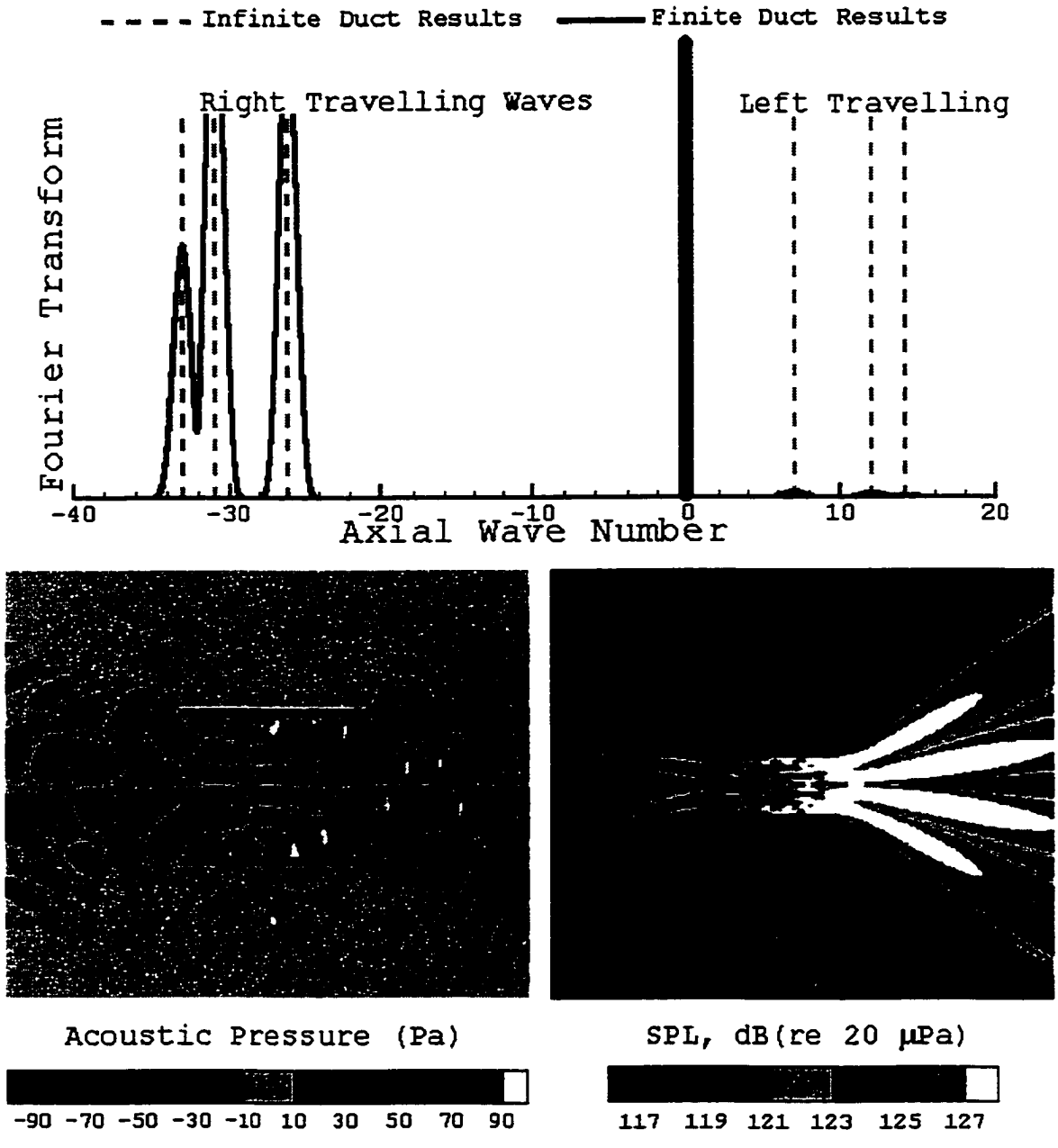

Figure 8.10 Spectral analysis $M = 0.4$

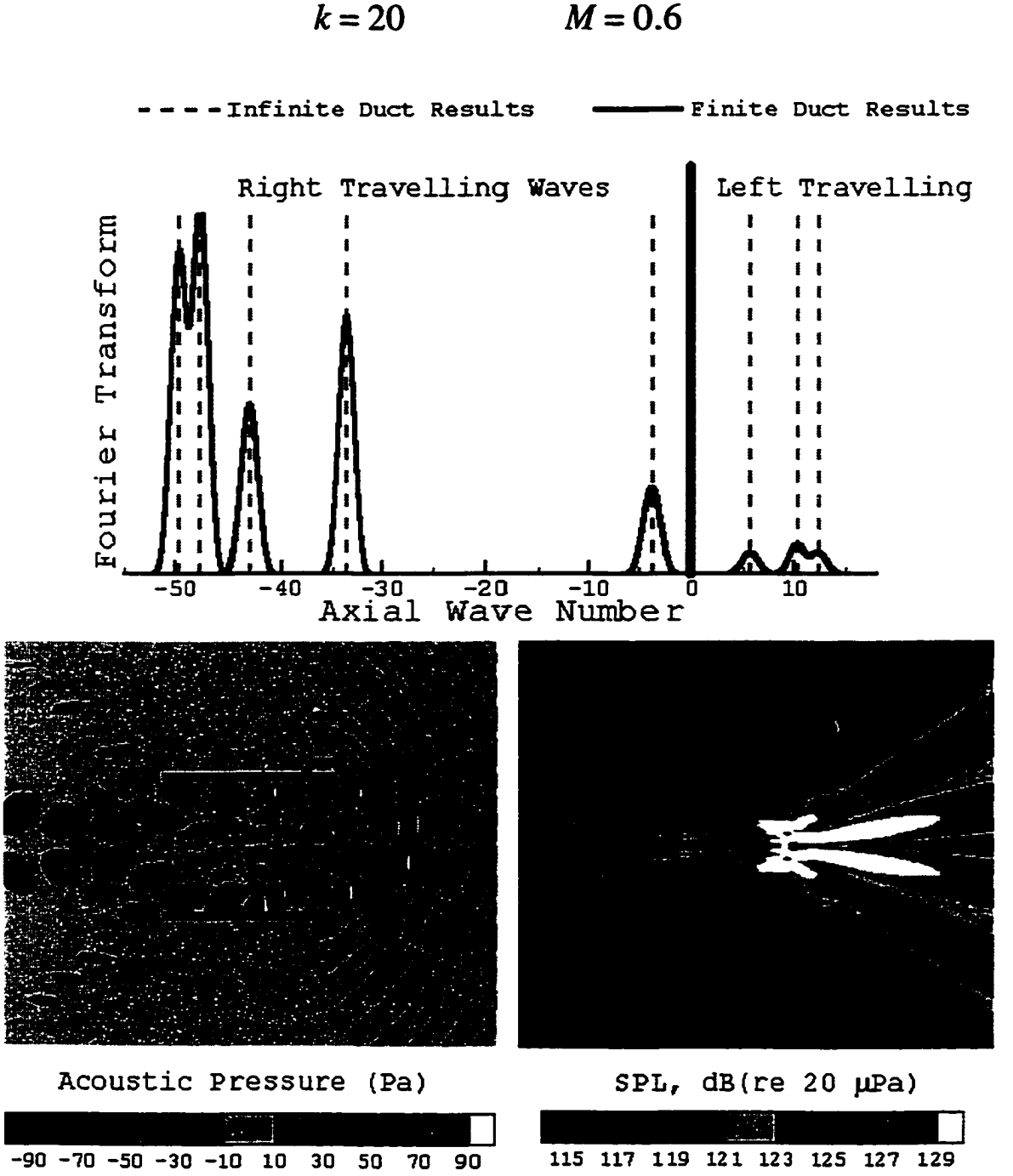

Figure 8.11 Spectral analysis $M = 0.6$

Something very interesting happens when the speed is increased to $M = 0.6$. The spectrum shows that there are additional cut-on frequencies. In particular, the $\pm 7^{th}$ modes are present. In addition, both are right travelling waves. This is evident in the strength of the sound exiting the inlet of the duct.

The previous spectrum examples are a very clear demonstration to the effectiveness of the numerical technique developed for solving these acoustic duct problems. In the next section a passive noise control technique, called scarf inlet, is considered.

8.9 Passive Noise Control (Scarf Inlet Model)

A duct is said to have a scarf inlet if the line joining the leading edges of its walls makes nonzero angle α with the normal to the walls. The case $\alpha = 0$ represents the conventional inlet, see Figure 8.12.

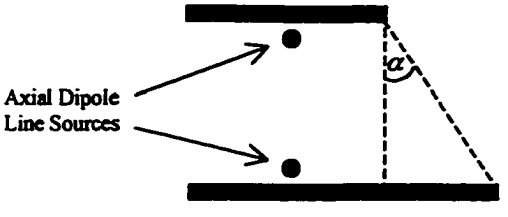

Figure 8.12 Geometry for scarf inlet

As is clearly shown in the sound pressure level plots, distinct lobes of prominent sound are present. The direction of these lobes can be approximated by a ray acoustics method. Rays are the solution to the homogeneous wave equation as the wave number approaches infinity. It can be shown that in a homogenous medium the wave fronts are plane waves and the rays are straight lines normal to the wave fronts [5]. That is, in a

limiting sense, the far field sound pressure level directivity is approximated by plane waves propagating in straight lines.

For large k, the group velocity of the n^{th} mode makes the angle θ_n with the duct axis [28] where

$$\cos(\theta_n) = \frac{\beta\sqrt{\kappa^2 - (n\pi/2h)^2}}{\sqrt{\beta^2\kappa^2 + M^2(n\pi/2h)^2}}$$

Furthermore, when sound waves impinge on the boundary the angle of incidence is equal to the angle of reflection. Hence, if the waves inside the duct are travelling at the angle corresponding to the group velocity vector, they must exit in a channel with the same angle, see Figure 8.13

.

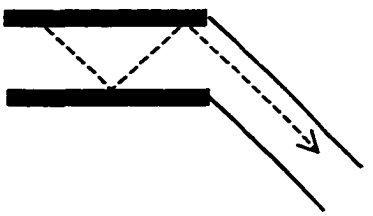

Figure 8.13 Group velocity vector

This simple geometric argument shows that if the lower portion of the duct is extended far enough; i.e. α is large enough, all sound is reflected upward.

Using ray acoustic approximations and the Wiener-Hopf technique for solving the 2-D scattering by a semi-infinite duct, Peake [27] has shown that at high frequencies and for $\frac{\pi}{2} \geq |\theta_n| > \frac{\pi}{2} - \alpha$ significant noise reduction in the lower farfield quadrant is possible

due to the scarf inlet. In particular, nearly 20 dB reductions can occur for near cut-off modes.

Dunn [8] has noted some limitations of the previous method. He suggests the following: large frequencies are required for asymptotic analyses, radiation angle analysis provides qualitative results in the far-field only and, the effect on the scarf inlet on the amplitudes of the reflected and transmitted modes inside the duct are not included.

The above restrictions do not apply to the integral equation method. It does not use modal decompositions. The only limitations of the boundary integral equation method are limitations due to the following: computational resources, thin duct approximations, linearity, and uniform inflow. Another advantage of the integral equation method is that propagation and radiation are coupled both forward and aft. No special numerical procedure is required to ensure continuity of the pressure at the duct inlet or exhaust. Furthermore, the solution is valid in both the far field and near field at all feasible frequencies and inflow Mach numbers.

8.10 Scarf Inlet Results

Experimental evidence exists which demonstrates that a scarf inlet affects the directivity of the noise radiation patterns [4]. The geometry for the scarf inlet is given in Figure 8.12. The results are divided into three case studies identified by the inflow Mach number ($M = 0$, 0.2, and 0.6). A contour plot of the near field radiation patterns is given for $k = 20$ and the following scarf inlets: $\alpha = 0^{\circ}$, 10°, 20°, and 30°. Next, the far field radiation patterns of the scarf inlet are compared to those from the conventional inlet. In this case, the SPL is computed for an arc of observers with radius 10 meters from the

sound source polar plots are given for

$k = 15, 20, 30$, and 40.

The following kinematics and geometry is used for the results to follow.

$$\tilde{\rho}_0 = 1.21 \ {}^{kg}/_{m^3}$$
$$\tilde{c} = 342 \ {}^{m}/_{sec}$$
$$\tilde{W} = 1 \text{ m}$$
$$\tilde{a}_1 = -\frac{1}{2}\tilde{W} \quad \tilde{b}_1 = \frac{1}{2}\tilde{W}$$
$$\tilde{a}_2 = -\frac{1}{2}\tilde{W} \quad \tilde{b}_2 = \left(\frac{1}{2} + \tan\alpha\right)\tilde{W}$$

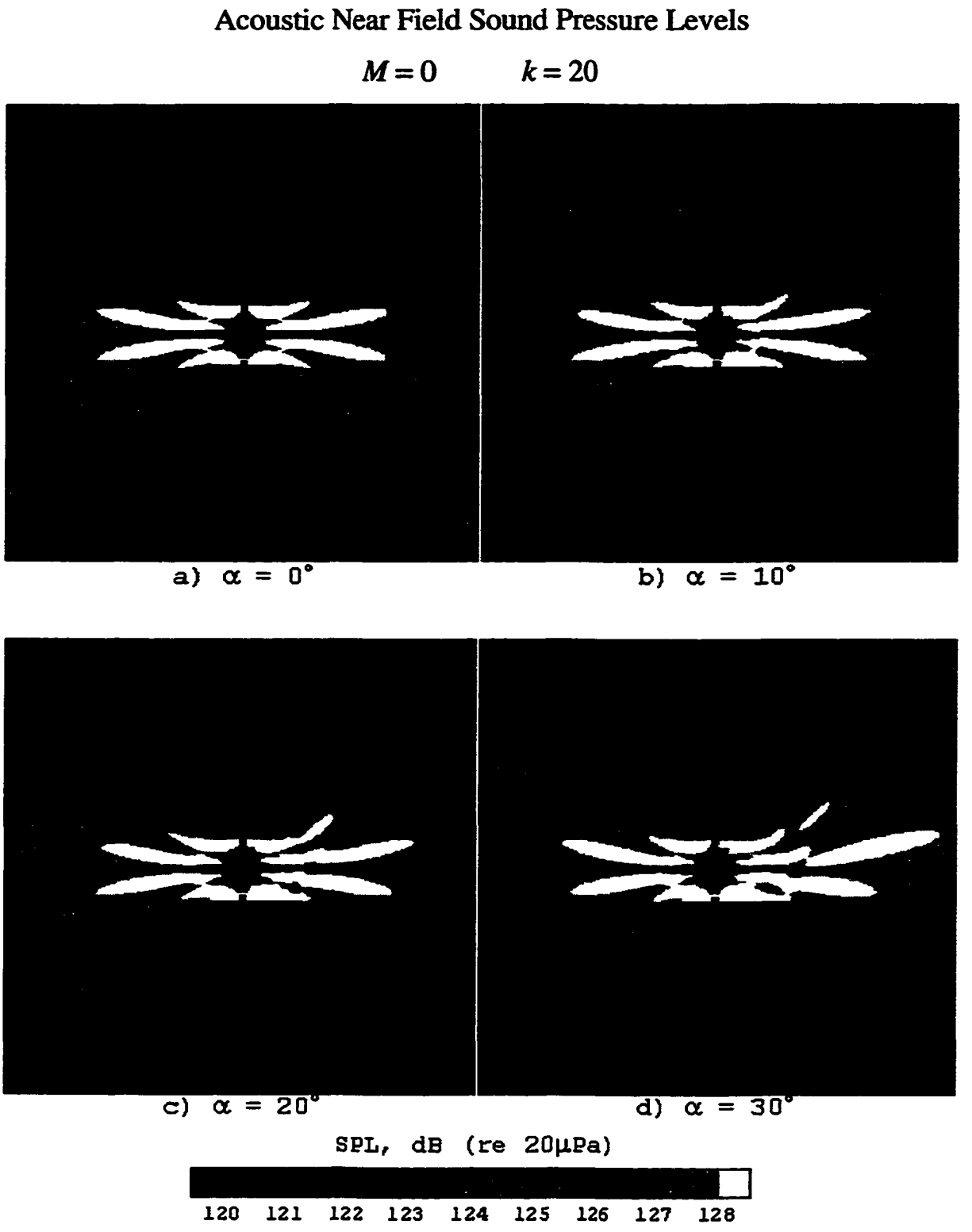

Figure 8.14 Acoustic near field for various inlet configurations ($M = 0.0$)

Several interesting results are demonstrated here. Firstly, it is intuitively clear that the $n = 1$ modes $\left(\theta_1^{\pm} \approx \pm 9.0^{\circ}\right)$ show very little attenuation. For these modes to be attenuated by the scarf inlet, the angle θ would need to be very large.

Now consider the $n = 3$ mode in the upper right quadrant, corresponding to $\theta_3^{+} \approx 28.11^{\circ}$. This mode is effected very little in Figure 8.14b corresponding to $\alpha = 10^{\circ}$, whereas when $\alpha = 20^{\circ}$ and $\alpha = 30^{\circ}$, we see considerable attenuation of the $n = 3$ mode. In particular, for $\alpha = 30^{\circ}$ the corresponding mode in the lower right quadrant, $\theta_3^{-} \approx -28.11^{\circ}$, is nearly completely attenuated.

Lastly, the $n = 5$ modes, in the upper right quadrant, are negligible in Figure 8.14a-b, but become quite prominent when $\alpha = 20^{\circ}$ or $\alpha = 30^{\circ}$.

The next case was chosen to simulate flight conditions at take-off. The same parameters will be used, with the exception of the Mach number, which will be increased to $M = 0.2$.

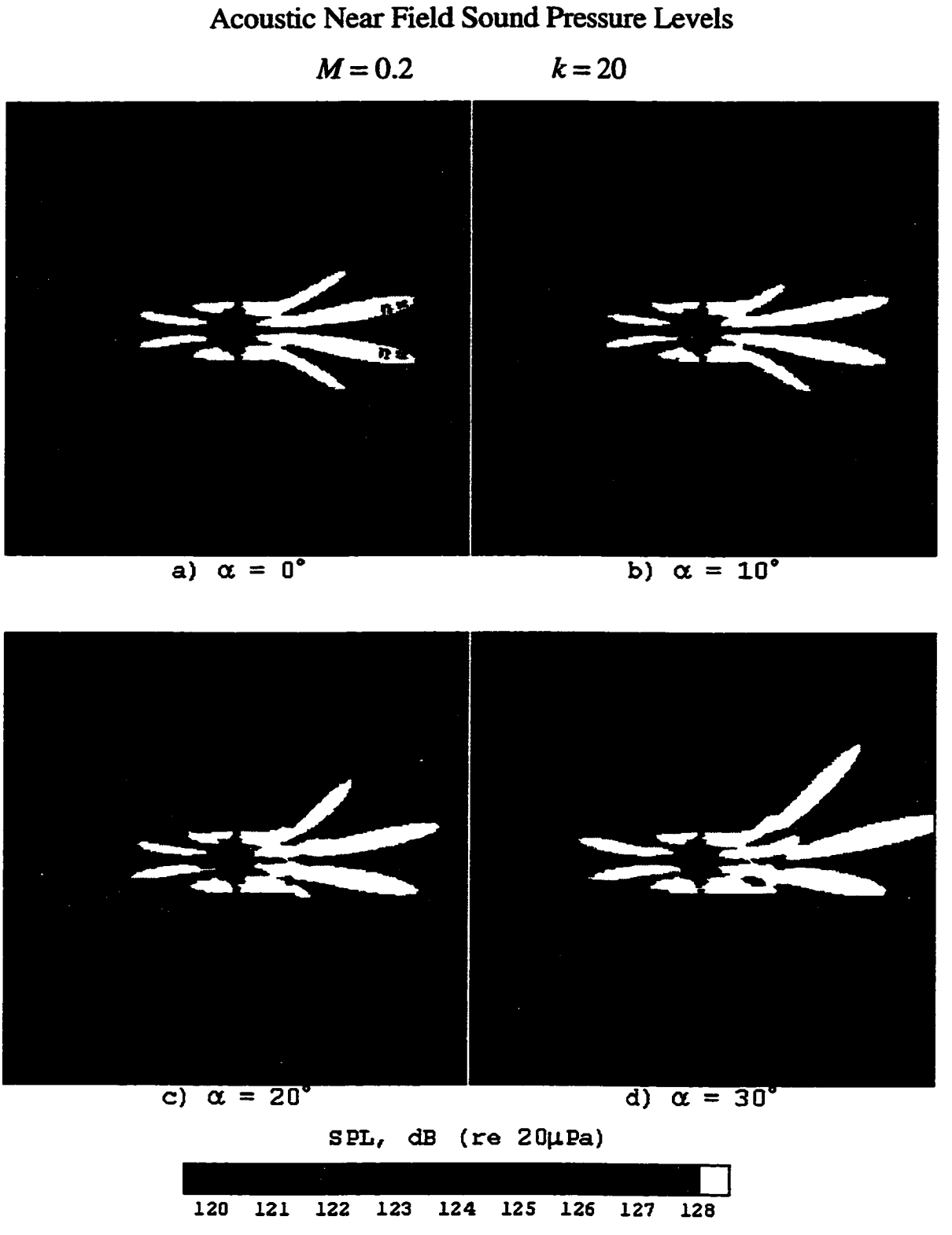

Figure 8.15 Acoustic near field for various inlet configurations ($M = 0.2$)

The noise radiation results in the upper right quadrant are similar to the case with no inflow. The exhaust pattern is far more skewed than the stationary case. The uniform inflow seems to effect the sound exiting the duct. This observation implies that the scarf inlet has an effect on the modal structure inside the duct.

To conclude the near field study, let $M = 0.6$.

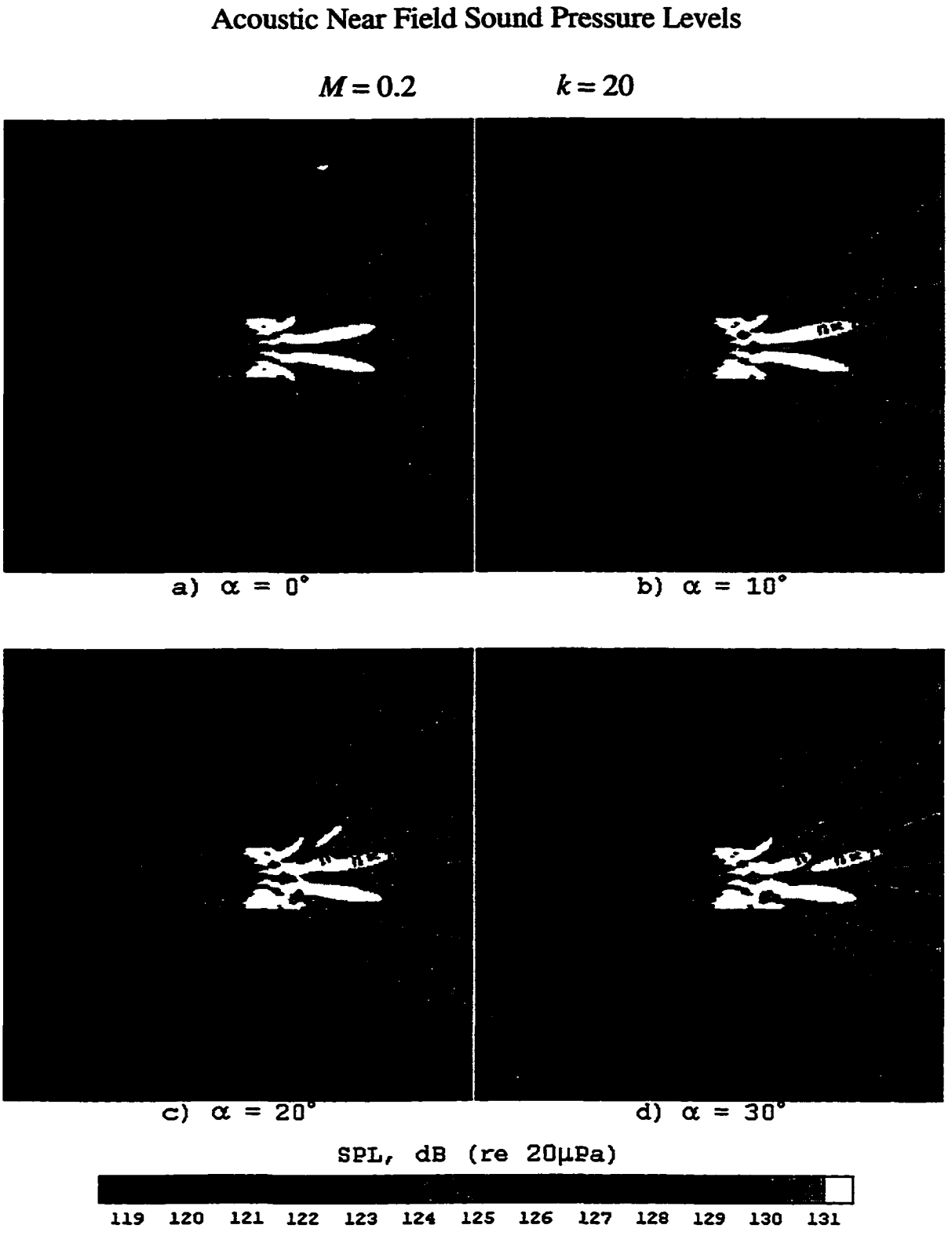

Figure 8.16 Acoustic near field for various inlet configurations ($M = 0.6$)

This case is particularly interesting. The magnitudes of the modes are effected considerably with the various inlet configurations. In particular, we validate the claim made by Peake. For the $n = 7$ mode (near cut-off), the noise is considerably lower with the scarf inlet.

In order to study the far field effects due to scarf inlets an arc of observers, radius 10 meters from the center of the duct, is used. A two-dimensional polar plot of the sound pressure levels is given for $k = 15, 20, 30$, and 40, and with $M = 0$, and 0.6. In Figure 8.17 - Figure 8.20 the sound pressure levels of a $\alpha = 20^{\circ}$ scarf inlet are compared with the conventional inlet sound pressure levels. The results here agree very well with the findings by Peake. However, with the studies conducted here, the ray acoustics conclusions can be expanded to include the following:

1. The scarf inlet is effective at directing the sound away from the lower inlet quadrant for a wide range of frequencies and inflow Mach numbers.
2. Significant noise reduction in the lower quadrant is possible for low order modes.
3. Noticeable noise reduction is observed in directions for which $\theta_n < \frac{\pi}{2} - \alpha$.
4. The scarf inlet affects the aft radiation pattern. The effects appear to be more pronounced for increasing Mach numbers.
5. Reflection patterns inside the duct can be severely affected by the scarf inlet thereby affecting the radiated field. This phenomenon requires further study and is the subject of future research.

Far Field Directivity – Sound Pressure Levels, dB (20 μPa)

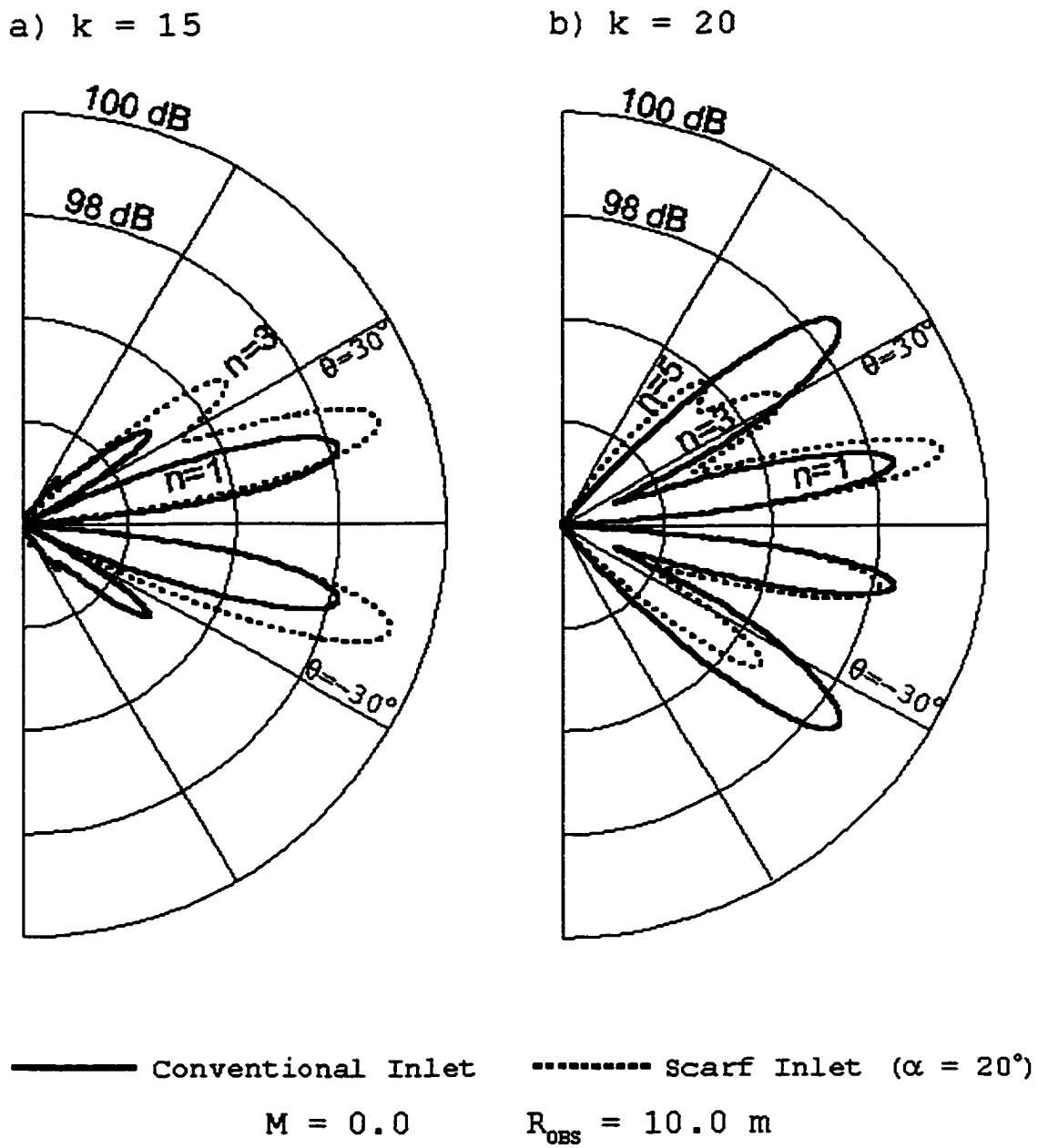

Figure 8.17 Far field directivity ($k = 15, 20$; $M = 0.0$)

Far Field Directivity – Sound Pressure Levels, dB (20 μPa)

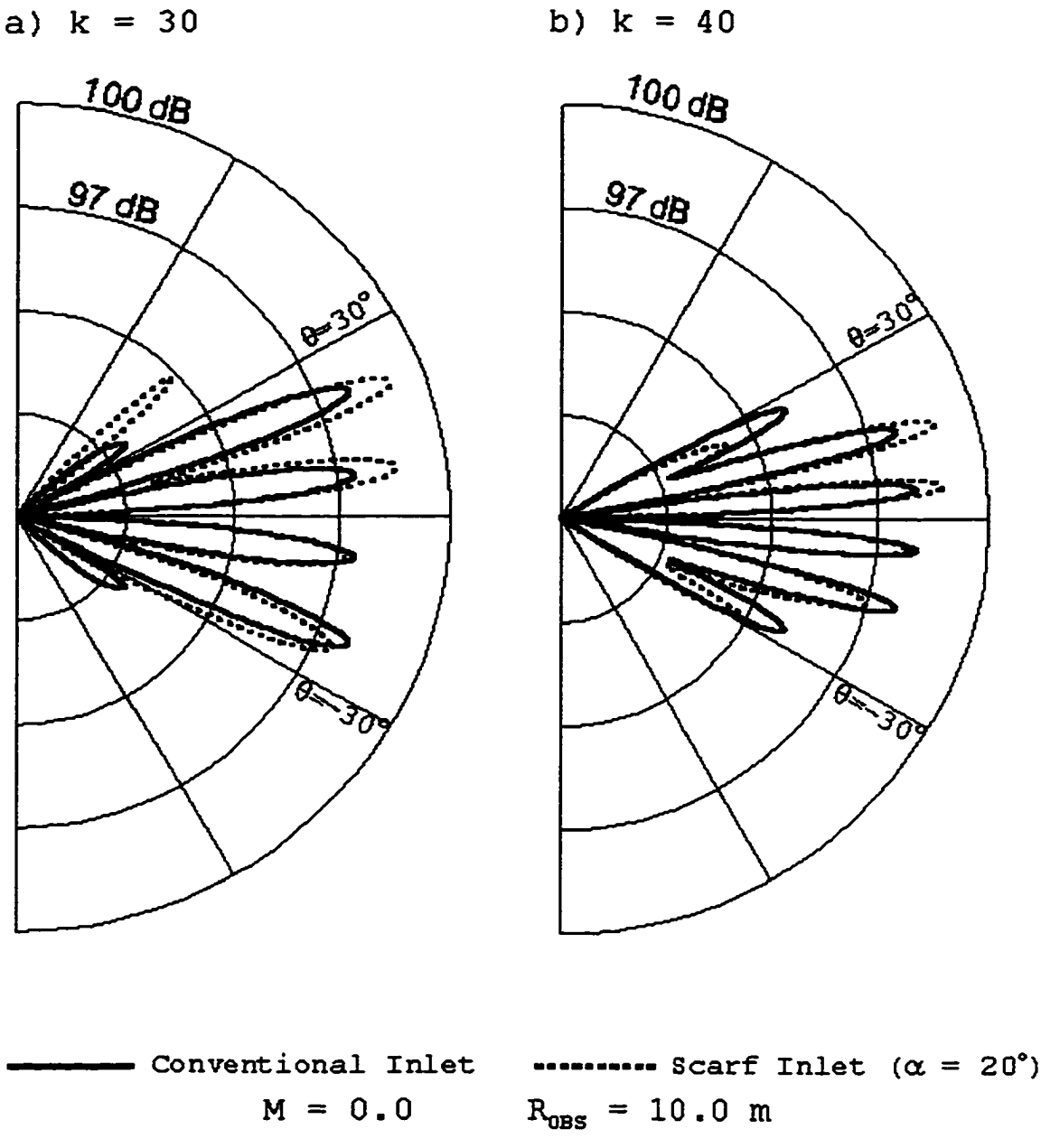

Figure 8.18 Far field directivity ($k = 30, 40$; $M = 0.0$)

Far Field Directivity – Sound Pressure Levels, dB (20 μPa)

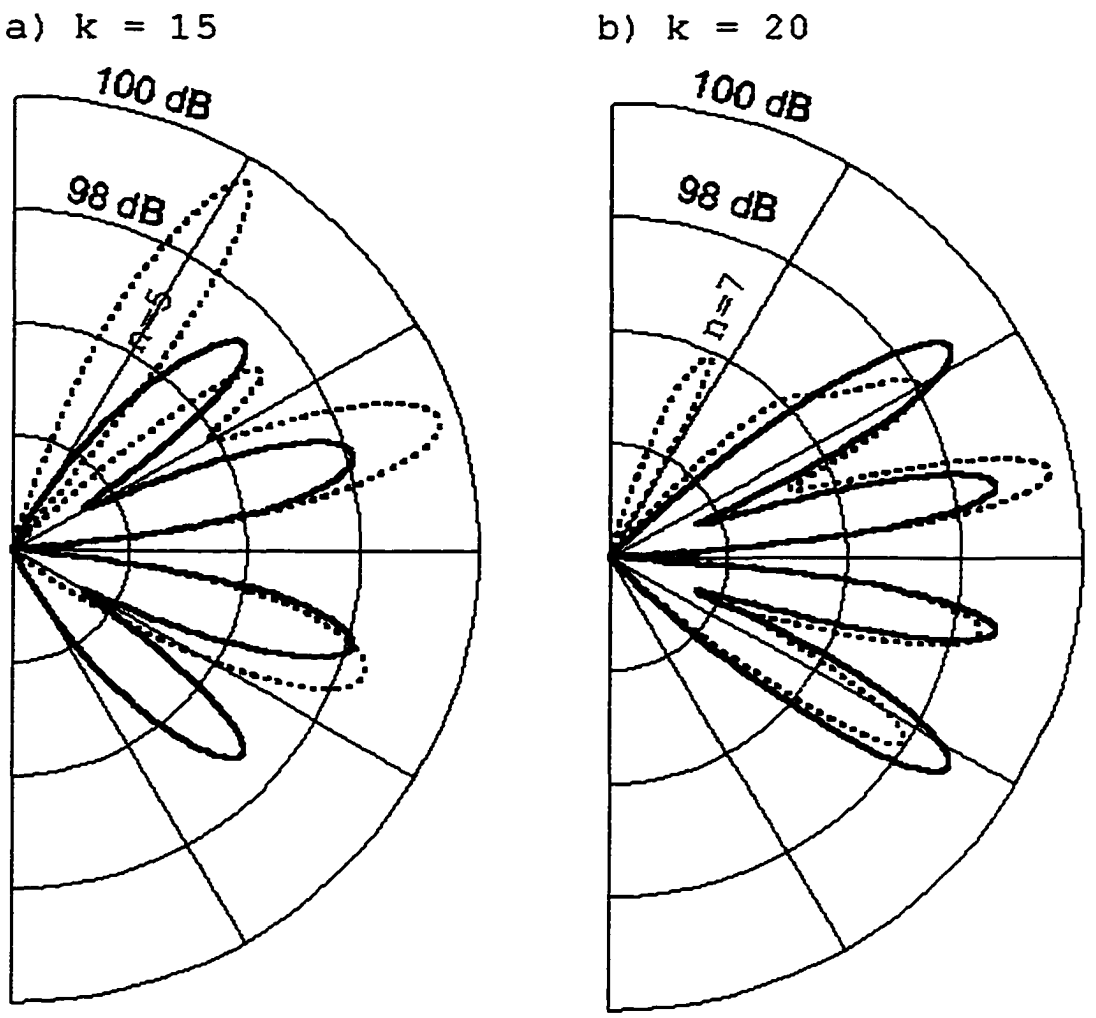

Figure 8.19 Far field directivity ($k = 15, 20$; $M = 0.6$)

Far Field Directivity – Sound Pressure Levels, dB (20 μPa)

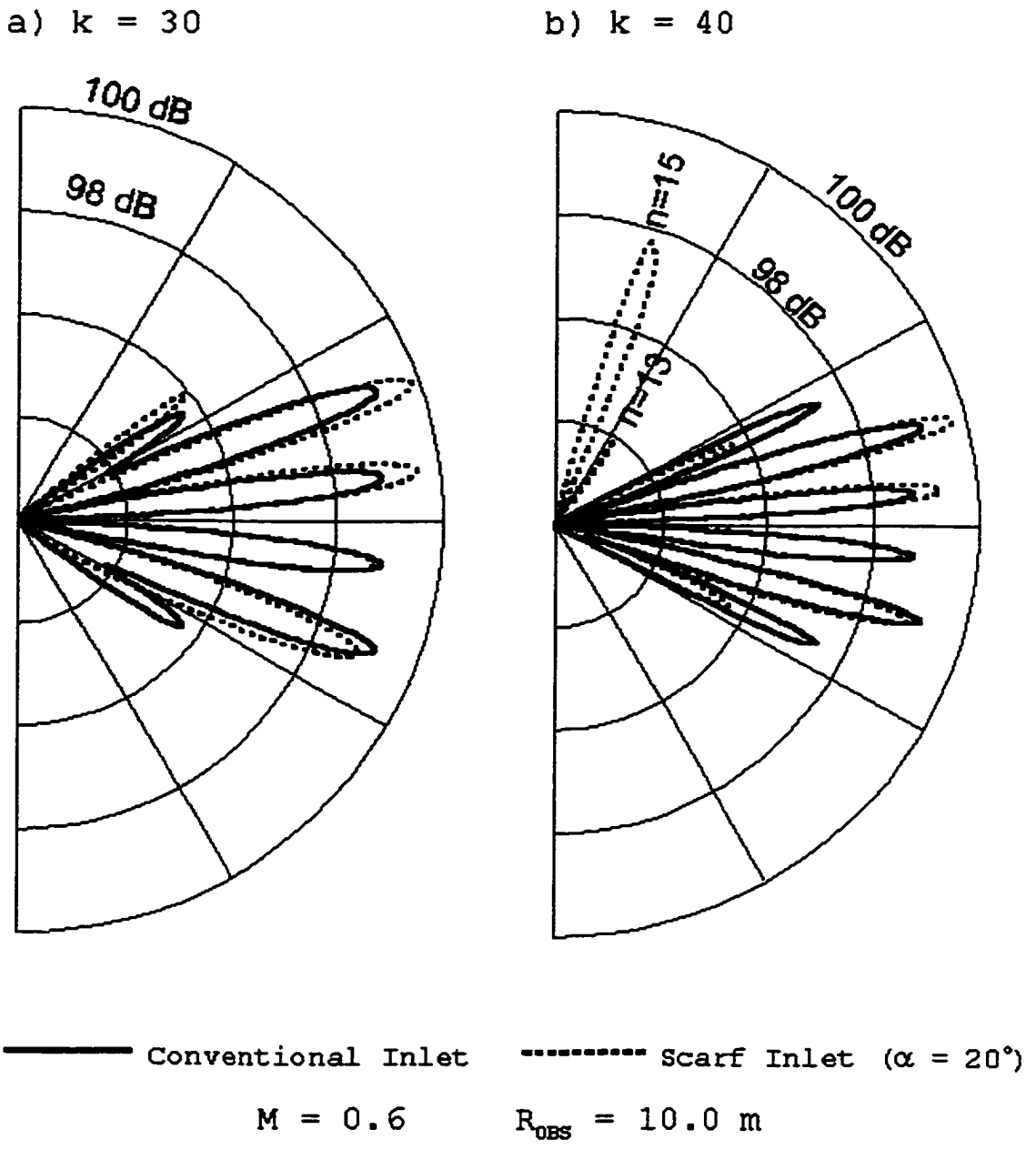

Figure 8.20 Far field directivity ($k = 30, 40$; $M = 0.6$)

8.11 Resonance

It is well known that the infinite duct problem is not solvable at certain frequencies, called eigenfrequencies. The finite duct is, in theory, solvable for all frequencies. Numerical studies have suggested that near the eigenfrequencies of the infinite duct the finite duct experiences resonance. Although a theoretical proof is outside the scope of the dissertation, this section will give numerical evidence to the veracity of this claim.

Consider a duct with length 2 meters and width 1 meter. The eigenfrequencies for the corresponding infinite duct have been previously determined to be $\lambda_n = n\pi$. It is further suggested that the numerical technique used for the finite duct becomes ill conditioned at these eigenfrequencies. Hence, in order to look for ill-conditioning Figure 8.21 is a plot of the condition number of the discretized system for the finite duct over a large range of frequencies.

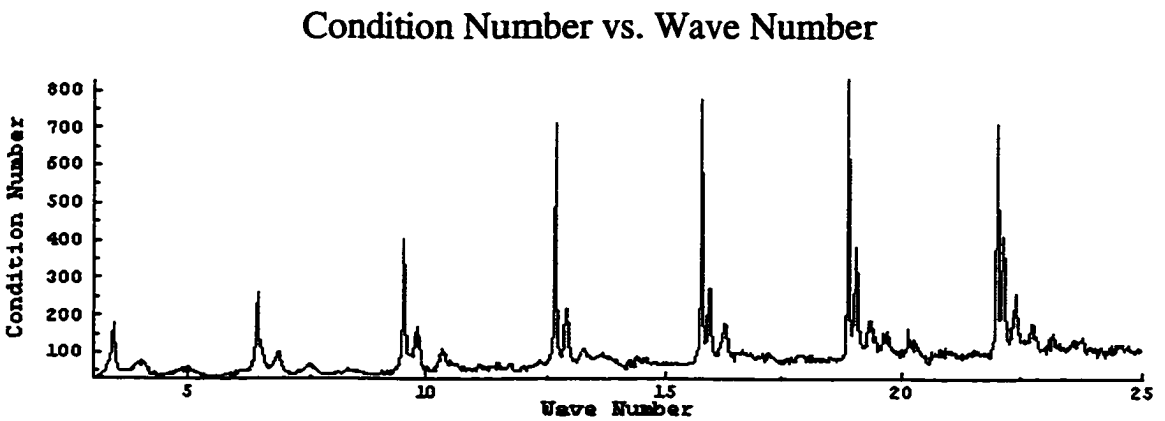

Figure 8.21 Condition number vs. Wave number

It is clear that at certain frequencies the matrix becomes more ill conditioned. The spikes in this plot represent the frequencies of possible ill conditioning. Clearly, these resonance frequencies are near the eigenfrequencies of the infinite duct. In fact, for a sufficiently long duct, the finite duct resonance frequencies are very close to the infinite duct eigenfrequencies.

Through numerical testing, a phenomenon has been observed. It appears that the axial dipole is not affected by these resonance frequencies. The geometry for this study is given by Figure 8.4, with the exception of the line sources. The first of two cases will use two symmetrically placed axial dipole line sources whereas the other will use two symmetrically placed monopole line sources. It will be shown that the monopole line sources experience resonance, although the accuracy of the solution is as yet undetermined. A monopole line source centered at (X_0, y_0) gives the incident field

$$\tilde{Q}_i(X,y) = \tilde{\nu} H_0^{(2)}\left[\kappa\sqrt{(X-X_0)^2+(y-y_0)^2}\right]. \tag{8.69}$$

Consider the resonance frequency $k = 15.774$, which corresponds to the eigenfrequency $\lambda_5 = 5\pi \approx 15.708$. Figure 8.22 clearly shows a standing wave in the monopole line case but no such wave exists in the case of a dipole line source. However, if the axial dipole line sources are sufficiently close to the inlet or exhaust resonance does occur for the axial dipole. Nevertheless, every case the author has considered, where the line sources are located near the center of the duct, demonstrates the type of behavior seen in Figure 8.22. A more detailed study of this phenomenon is left for further research.

Resonance Flood Plot

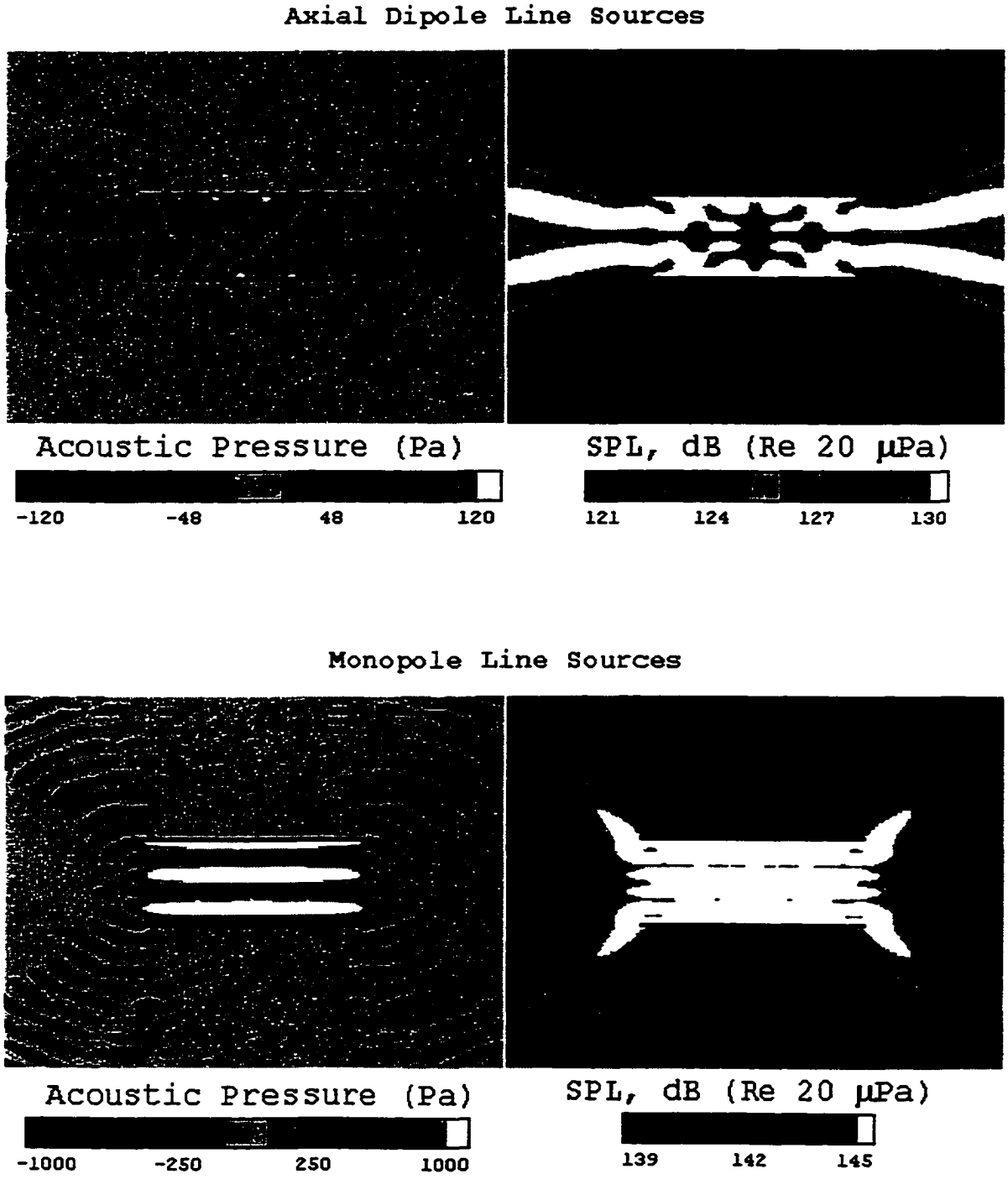

Figure 8.22 Resonance for axial dipole and monopole line sources

8.12 Conclusions

We have shown that the scarf inlet has the potential of redirecting sound away from sensitive areas. It was also shown that noise reduction occurs in the far field as well as the near field.

We have demonstrated the usefulness and versatility of the boundary integral equation method for solving the finite duct problem with scarf inlets. The mathematical formulation for two and three-dimensional scattering of sound by finite length ducts are very similar. We therefore expect the observations for the two-dimensional case to apply to the sound scattered by a cylindrical duct with a scarf inlet in a uniform flow field.

The computer code TBIEM2D [31] was used for calculation for the two-dimensional duct. For the three-dimensional cylindrical duct, studies can be performed via TBIEM3D [6]. In this case, the sound from a finite cylindrical duct is computed via a boundary integral equation method. Both codes can easily be used to study acoustic scattering for any computationally feasible frequency, subsonic inflow Mach number, duct length, and inlet configuration.

SECTION 9

CONCLUSIONS

In this dissertation computationally efficient algorithms were given for the solution of two classes of hypersingular integral equations. It was shown that the collocation method was the preferred method for solving each class of integral equation. The reason for this is two-fold. The Galerkin method requires a computationally expensive double numerical integration whereas the collocation method only requires one numerical integration. However, the question of convergence is just as important as computer resources. Although convergence results were proven for both the Galerkin and collocation methods, it was unclear as to which method converged faster. We were able to give qualitative meaning to the rates of convergence. Surprisingly, we saw that collocation method was superior in that realm as well.

Once we established numerical techniques for solving each class of hypersingular integral equation, we were able to use the techniques to solve problems in fracture mechanics and acoustics. The first problem was the dynamic crack problem. We were able to relax the rather strong restrictions imposed by the techniques used by Itou and Mal. In addition, the method we derived for the dynamic crack problem was versatile enough to apply to parallel and perpendicular line crack problems. We were able to solve these dynamic crack problems for different configurations of disjoint parallel and perpendicular Griffith cracks, yielding new insight into these problems.

The last area of research was conducted in acoustics. The moving wing problem was solved first and served as a precursor to the moving finite duct problem. In particular, we focused on the effects of a scarf inlet design on the sound field. We saw that we could redirect sound away from sensitive areas with the appropriate inlet design.

Passive noise control studies are the topic for future research. In particular, the effects of acoustic liners in a moving duct will be examined. Some modifications will be required to the techniques presented here in order to solve the lined duct problem. Nonetheless, the work in this dissertation will help to develop such models.

REFERENCES

[1] I. D. Abrahams and G. R. Wickman, On the Scattering of Sound by Two Semi-infinite Parallel Staggered Plates, II. Evaluation of the Velocity Potential for an Incident Plane Wave and an Incident Duct Mode, *Proc. Roy. Soc.* **427** (1990) 139 – 171.

[2] I. D. Abrahams and G. R. Wickman, On the Scattering of Sound by Two Semi-infinite Parallel Staggered Plates, I. Explicit Matrix Wiener-Hopf Factorization, *Proc. Roy. Soc.* **420** (1988) 131 – 245.

[3] C. T. Baker, *The Numerical Treatment of Integral Equations*, (Clarendon Press, Oxford, New York, 1977)

[4] L. R. Clark, R. H. Thomas, R. P. Dougherty, F. Farassat, and C.H. Gerhold, Inlet Shape Effects on the Far-field Sound of a Model Fan, *AIAA-97-1589* (1997).

[5] D. G. Crighton, A. P. Dowling, J. E. Ffowcs Williams, M. Heckl, and F. G. Leppington, *Modern Methods in Analytical Acoustics, Lecture Notes*, (Springer-Verlag, New York, 1992).

[6] M. H. Dunn, TBIEM3D – A Computer Program for Predicting Ducted Fan Engine Noise, Version 1.1, *NASA/CR-97-206232* (1997).

[7] M. H. Dunn, J. Tweed, and F. Farassat, The Prediction of Ducted Fan Engine Noise Via a Boundary Integral Equation Method, *AIAA-96-1770* (1996).

[8] M. H. Dunn, J. Tweed, and R. St.John, Sound Radiation from a Two-Dimensional Scarf Inlet Using Noise Prediction Code TBIEM2D, *AIAA-98-2202* (1998).

[9] P. J. T. Filippi, Layer Potentials and Acoustic Diffraction, *Journal of Sound and Vibration* **54(4)** (1977) 473 – 500.

[10] A. Frenkel, A Chebyshev Expansion of Singular Integrodifferential Equations with a $\partial^2 \ln|s-t| / \partial s \partial t$ Kernel, *Journal of Computational Physics* **51** (1983) 335 – 342.

[11] J. Fromme and M. A. Golberg, Numerical Solution of a Class of Integral Equations Arising in Two-Dimensional Aerodynamics, *Solution Methods for Integral Equations with Applications*, (Plenum, New York, 1979).

[12] F. D. Gakhov, *Boundary Value Problems*, (Dover Publications, Inc., New York, 1996).

[13] M. A. Golberg, The Convergence of Several Algorithms for Solving Integral Equations with Finite-Part Integrals, *Journal of Integral Equations* **5** (1983) 329 – 340.

[14] M. A. Golberg, The convergence of several algorithms for solving integral equations with a finite-part integral II, *Applied Math & Comp.* **21** (1987) 283 – 293.

[15] A. A. Griffith, The phenomena of rupture and flow in solids, *Phil. Trans. A.* **221** (1921) 163.

[16] J. Hadamard, *Lectures on Cauchy's Problems in Partial Differential Equations*, (Yale University Press, New Haven CT, 1923).

[17] G. R. Irwin, Analysis of stresses and strains near the end of a crack traversing a plate, *J. Appl. Mech.* **24**, 3.

[18] S. Itou, Diffraction of an antiplane shear wave by two coplanar Griffith cracks in an infinite elastic medium, *Int. J. Solids Structures* **16** (1980) 1147 – 1153.

[19] D. L. Jain, and R. P. Kanwal, Diffraction of elastic waves by two coplanar Griffith cracks in an infinite elastic medium, *Int, J. Solid Structures* **8** (1972) 961 – 975.

[20] J. F. Kalthoff, S. Winkler and J. Beinert, The influence of dynamic effects in impact testing. *Int. J. Fracture* **13** (1977) 528 – 531.

[21] A. C. Kaya and F. Erdogan, On the solution of integral equations with strongly singular kernels, *Quart. Appl. Math* **45** (1987) 105 – 122.

[22] A. C. Kaya and F. Erdogan, On the solution of integral equations with a generalized Cauchy kernel, *Quart. Appl. Math*, **45** (1987) 455 – 469.

[23] Rainer Kress, *Linear Integral Equations, Applied Mathematical Sciences, Vol. 82*, (Springer-Verlag, New York, 1980).

[24] J. F. Loeber and G. C. Sih, Diffraction of anti-plane shear waves by a finite crack. *J. Acoustic Soc. Am.* **44** (1968) 90 – 98.

[25] W. Magnus, F. Oberhettinger and R. P. Soni, *Formulas and theorems for the special functions of mathematical physics*, (Springer-Verlag, New York, 1966).

[26] A. K. Mal, Interaction of elastic waves with a Griffith crack, *Int. J. Engng Sci.* **8** (1970) 763 – 776.

[27] N. Peake, A theoretical investigation of the noise radiation from a scarfed intake, *CEAS / AIAA*-95-101 (1995).

[28] E. J. Rice, M. F. Heidmann, and T. G. Sofrin, Modal propagation angles in a cylindrical duct with flow and their relation to sound radiation, *AIAA*-79-0183 (1979).

[29] G. C. Sih and J. F. Loeber, Wave propagation in an elastic solid with a line of discontinuity or finite crack. *Quart. Appl. Math.* **27** (1969) 193 – 213.

[30] V. I. Smirnov, *A Course of Higher Mathematics Vol. IV.* (Pergamon Press, Oxford, 1964).

[31] R. St.John, and M. H. Dunn, TBIEM2D – A Computer Program for Predicting the Noise Radiated from Two-Dimensional Ducts, Version 1., *To Appear as a NASA Contractor Report.*

Richard St. John

Education

1998 – Ph.D. Computational and Applied Mathematics, Old Dominion University
1995 – M.S. Computational and Applied Mathematics, Old Dominion University
1993 – B.S. Applied Mathematics, Old Dominion University

Presentations and Publications

"TBIEM2D – A Computer Program for Predicting the Noise Radiated from Two-dimensional Ducts"
R. St.John and M.H. Dunn, NASA/CR-98-XXXX

"Sound Radiation from a Two-dimensional Scarf Inlet Using the Noise Prediction Code TBIEM2D"
M. H. Dunn, J. Tweed, and R. St.John; AIAA-98-2202

"Algorithms for the Numerical Solution of a Finite-Part Integral Equation"
J. Tweed, R. St.John, and M. H. Dunn;

"The Solution to Hypersingular Integral Equations with Applications in Acoustics and Fracture Mechanics"
Presented at the MD-DC-VA Section meeting of the MAA, Nov. 21-22, 1997

"2-D Acoustic Scattering and Noise Control"
Presented at VCES Spring Conference, Hampton, VA; June 11 – 12, 1997

"Solving Hadamard Integral Equations, a Numerical Approach"
Presented at Graduate Student Seminar Series, Old Dominion University, Norfolk, VA; Sept. 1996

Research Interests

- Singular Integral Equations
- Numerical Analysis
- Algorithm Development
- Programming
- Fracture Mechanics
- Acoustics

Honors

- Dept. of Mathematics and Statistics Teacher of the Year Nominee, 1998
- Phi Kappa Phi Honor Society, April 1997
- Outstanding Senior in Mathematics/Statistics Award, April 1993

IMAGE EVALUATION
TEST TARGET (QA-3)

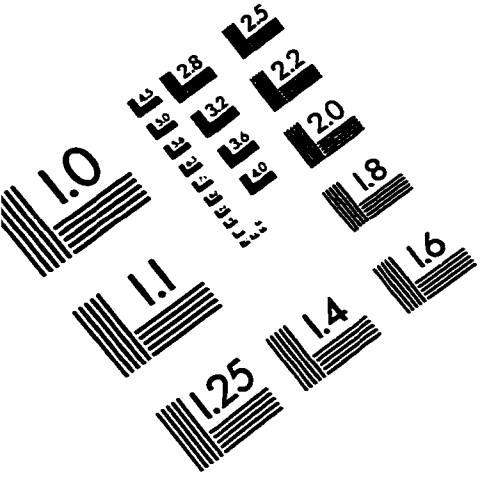

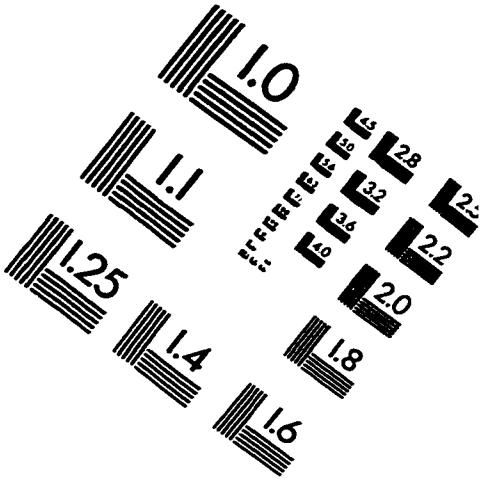

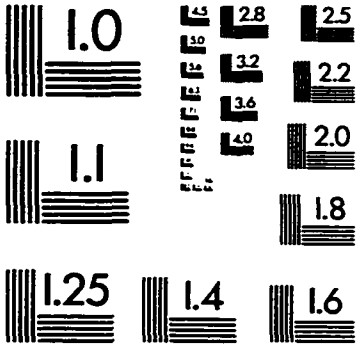

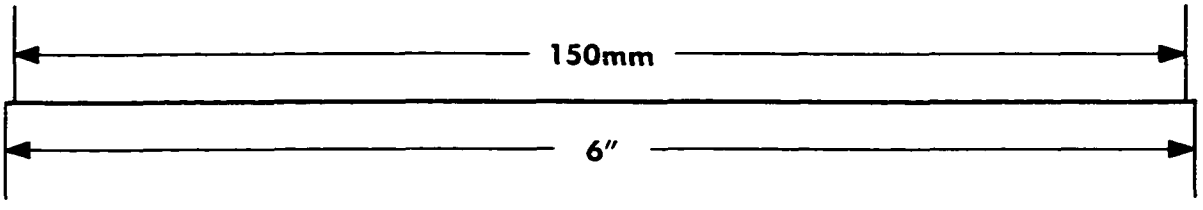

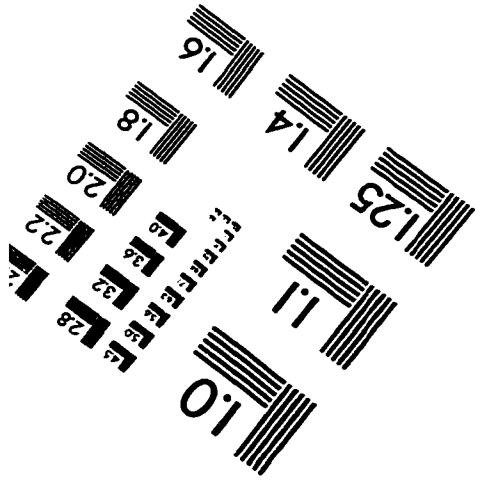

APPLIED IMAGE, Inc
1653 East Main Street
Rochester, NY 14609 USA
Phone: 716/482-0300
Fax: 716/288-5989